Protection of AC Wind Collection Grid with HVDC Transmission

Elforsk rapport 11:69

G. Velotto, R. Irnawan, M. Moccia, K. Srivastava, M. Reza

May 2012

ELFORSK

Protection of AC Wind Collection Grid with HVDC Transmission

Elforsk rapport 11:69

G. Velotto, R. Irnawan, M. Moccia, K. Srivastava, M. Reza May 2012

Foreword

For wind farm connection, HVDC transmission based on voltage source converter (VSC) give some advantages, such as its ability to independently control active and reactive power, to control frequency and its black start capability.

One of main challenges in connecting HVDC connected wind farm is the protection system. There are several factors that make the protection of HVDC connected wind farm is more challenging than it of HVAC wind farm. In order to further investigate these challenges and find solutions a project V-321 was formed within the research program Vindforsk III.

Vindforsk-III is funded by ABB, Arise windpower, AQ System, E.ON Elnät, E.ON Vind Sverige, EnergiNorge, Falkenberg Energi, Fortum, Fred. Olsen Renewables, Gothia Vind, Göteborg Energi, HS Kraft, Jämtkraft, Karlstads Energi, Luleå Energi, Mälarenergi, O2 Vindkompaniet, Rabbalshede Kraft, Skellefteå Kraft, Statkraft, Sena Renewable, Svenska kraftnät, Tekniska Verken i Linköping, Triventus, Wallenstam, Varberg Energi, Vattenfall Vindkraft, Vestas Northern Europe, Öresundskraft and the Swedish Energy Agency.

Comments on the work and the final report have been given by a reference group with the following members: Kristian Høy-Thomsen, E.ON, Sigbjørn Sørbotten, Statnett, Norway, Jianping Wang, ABB, Muhamad Reza, ABB, Peter Sandeberg, ABB and Anders Holm, Vattenfall.

Stockholm November 2012

Anders Björck
Program manager Vindforsk-III
Electricity and heat production, Elforsk AB

Summary

This report firstly presents a short-circuit study of two AC wind collection grids: one is equipped with Doubly Fed Induction Generator (DFIG) and the other one with Full-scale Converter Generator (FCG) wind turbines. Afterwards, it analyzes the results and proposes fault detection methods for faults in the AC collection grids. In both cases, the AC collection grids are connected to the main grid by a VSC-HVDC (Voltage Source Converter – High Voltage DC) transmission system.

Simplified models of HVDC, DFIG, and FCG suitable for simulation with PSCAD/EMTDC software were developed. A study system consisting of 9 wind turbines placed on 3 feeders, with each feeder having 3 wind turbines, was also developed. Three-phase short-circuits at a number of locations in the collection grid were studied. The short-circuit contribution of the HVDC link and the FCG was limited to 10% above the rated current. The voltage and currents were simulated and post-processed using sliding data window method having 20 milliseconds width (one cycle of 50 Hz). The information such as the peak value of the voltage and current, the fundamental component of voltage and current, the harmonic contents, and the derivative of the voltage and current were obtained. In addition, the instantaneous active power and impedance were also computed. The protection logic was built based on the above information.

The studies revealed that in the AC collection grid with DFIG wind turbines, a faulty feeder can be detected by observing the peak current at the collection point. An over-current relay can be utilized to accomplish this objective.

A faulty section within a feeder can be detected by comparing the current magnitude from the two ends of the section. This can be accomplished by utilizing a current differential relay. This would require a communication link between the two ends of the section.

In the AC collection grid with FCG wind turbines, a faulty feeder can be detected by combining the information such as the active power direction and the peak current observed at the collection point. Directional power relay and over-current relay can be utilized to accomplish this objective.

Three different methods for identifying the faulty section within a feeder were investigated. These methods are based on the comparison of current magnitudes from the two ends of the section, comparison of the active power direction at the two ends of the section, and comparison of the positive sequence impedance at the two ends of the section. All these three methods require a communication link between the two ends of the section. This can be accomplished by utilizing the current differential, directional power, and positive sequence impedance relays.

Sammanfattning

Denna rapport beskriver kostslutningsberäkningar för två typer av uppsamlingsnät för vindkraftparker. Båda näten är växelströmsnät. I den ena utgörs vindgeneratorerna av dubbelmatade asynkronmaskiner (Doubly Fed Induction Generator-DFIG) medan det i den andra utgörs av generatorer av fullomriktartyp (Full-scale Converter Generator-FCG). Resultaten har analyserats och rekommendationer för feldetekteringsmetoder för fel i uppsamlingsnät av växelströmstyp har tagits fram. I båda fallen har uppsamlingsnäten varit anslutna till stamnätet via etn spänningsstyv HVDC-länk (VSC-HVDC:Voltage Source Converter – High Voltage DC) transmissionssystem.

Förenklade modeller för VSC-HVDC, DFIG och FCG har utvecklats för simuleringsprogramvaran PSCAD/EMTDC. Ett typsystem bestående av 9 vindkraftverk anslutna till tre olika matningar (tre verk per matning) implementerades för studien. Trefasig kortslutning har studerats vid ett antal positioner i uppsamlingsnätet. Kortslutningsbidraget från HVDC-länken och FCG begränsades till 10% över märkström. Spänningar och strömmar har simulerats och analyserats med ”sliding data window” med 20 millisekunders bredd (en 50Hz-cykel). Maxvärden, grundfrekvens och derivator för ström och spänning, övertonsinnehåll samt momentan aktiv effekt och impedans har också beräknats. Skyddslogiken har designats utifrån denna information.

Studien visar att i AC-uppsamlingsnät med DFIG-vindkraftverk kan den felbehäftade ledningen detekteras genom att mäta strömmen vid uppsamlingspunkten. Ett överströmsrelä kan användas för detta ändamål.

Den felaktiga sektionen i felbehäftad ledning kan detekteras genom att jämföra strömmens amplitud vid sektionens båda ändar. Detta görs lämpligen med ett strömdifferential-relä. Detta kräver dock kommunikation mellan sektionens ändar.

För AC-uppsamlingsnät med FCG-vindkraftverk så kan den felbehäftade ledningen detekteras genom att kombinera information om (aktiv) effektriktning och maxström vid uppsamlingspunkten. För detta kan effektriktningsreläer och överströmsskydd användas.

Tre olika metoder för detektering av felaktiga sektioner undersöktes. Den första metoden bygger på att man jämför strömamplitud vid sektionens ändar, den andra på att man jämför (aktiva) effektriktningen vid sektionens ändar och den tredje på att man jämför uppmätta plusföljdsimpedanser vid sektionens ändar. De tre metoderna kräver alla kommunikation mellan sektionernas ändar. Feldetekteringen kan åstadkommas med strömdifferens-reläer, effektriktningsreläer och plusföljdsimpedansreläer.

Innehåll

1 Introduction

1.1 Background

During the last decade, world non-hydro renewable electricity generation has gradually increased from 1.7% of total electricity generation in year 2000 to 4.6% in year 2009 [0]. This number is expected to increase since many countries try to get 20% of their electricity generation from renewable resources by 2020 [0]. In Europe, 41% of new electricity generation installations during 2010 came from renewable energy [0]. This statistic shows a huge leap of EU countries to move away from fossil fuels and nuclear power.

Among renewable energy sources, wind energy is the fastest growing energy technology, due to its cost-competitiveness, reliability, and efficiency[0]. At the end of year 2000, there are 18 GW installed capacity of wind energy around the globe. By the end of year 2010 this number has increased tremendously to 195 GW [0]. With 44% of the global installed wind energy capacity in 2010, Europe is the global leader in wind energy technology[0].

In order to maximize wind turbine efficiency and power generation capacity without increasing the environmental impacts such as aesthetic issues, noise pollution and ecological life, wind farms are preferably located in remote sites, both offshore and onshore. If the wind farm connection exceeds 80 km offshore [0] or 500 km onshore [0], HVDC transmission system gives more economical benefits than HVAC transmission system. Voltage source converter high voltage DC (VSC-HVDC) system is a better option than the classical (Line Commutated Converter) HVDC system because of independent active and reactive power controllability and small filter requirements [0]. Further in this study, the term HVDC will refer to VSC-HVDC.

1.2 Elforsk research scope V-321 and V-323

Wind farm collection grid can be either AC or DC. AC collection grid has been most popularly used in the offshore and onshore wind farm. With increasing size of wind farms, the losses in the collection grid will increase. Therefore the interest for DC collection grid is increasing.

The use of HVDC-connected wind farm should be guaranteed by a good protection system. By having a good protection system, faulty parts within the wind farm can be removed as quickly as possible while leaving the healthy parts to operate.

Elforsk has sanctioned two projects V-321 and V-323 concerning the protection in HVDC-connected wind farm. Project V-321 deals with protection of HVDC connected wind farm with AC collection grid. Project V-323 focuses on protection of HVDC wind farm with DC collection grid.

ABB Corporate Research Sweden has been responsible for project V-321 i.e. the studies relating to protection of HVDC connected wind farm with AC collection grid.

Vattenfall AB has been assigned the task of executing project V-323 i.e. the studies relating to protection of HVDC connected with farm with DC collection grid.

This report presents the findings of project V-321 only and does not cover the findings of V-323. The findings of V-323 will be separately reported by Vattenfall AB.

1.3 Problem description

Project V-321 focused on the fault detection in the AC collection grid that is connected to the main network by a HVDC transmission link. This study focused on the method to detect the fault in the AC collection grid by examining different signals behavior from the post-processed current and voltage measurement signals.

In this study, a system of HVDC connected wind farm was modeled and simulated. The short-circuit analysis for several fault scenarios within the AC collection grid were performed. Potential protection schemes for this HVDC connected wind farm were proposed.

The study has considered two wind turbine generator (WTG) technologies – doubly fed induction generator (DFIG) and full scale converter generator (FCG). Reference [0] describes DFIG technology as Type-3 and FCG as Type-4.

WTG Type 3 is also known as Doubly Fed Asynchronous Generator (DFAG). It is possible to operate DFIG over a wide range of speed, typically ±33% of synchronous speed.

WTG Type 4 employs a full scale power electronic converter between the generator and the grid. Usually, a back-to-back voltage source converter (VSC) is used in order to achieve full control of the active and reactive power.

The advantages of using DFIG and FCG are the improvement in efficiency, flexibility, and stability. Today most of the wind farms predominantly employ either of two WTG technologies [0] and [0].

Some of the challenges of the protection of HVDC-connected wind farm with AC collection grid, especially one with FCG wind turbines are as follows:

- Converter at HVDC station limits short circuit current contribution from grid-side
- Converters at wind turbine limit short circuit contribution from every turbine generator
- Consequently, short circuit currents may be close to rated current values
- Classical protection for AC distribution system may not be directly applicable and require new protection algorithms/methods

1.4 Structure of the report

The present report is structured in six chapters.

The second chapter discusses the research method and some limitations for the study.

The third chapter discusses the wind farm configuration and modeling of the main components used in the study.

The fourth chapter presents the short-circuit simulation results for HVDC-connected wind farm with DFIG wind turbines and the proposed protection methods.

The short-circuit simulation results for HVDC-connected wind farm with FCG wind turbines and the proposed protection methods are presented in chapter 5.

Finally, the conclusions of the study along with the ideas for the future work are presented in Chapter 6.

2 Research method

The studies were performed by adopting a research methodology depicted in Figure 1. The first step was to build the study system model in PSCAD/EMTDC. After having built the model, short-circuit fault for different scenarios was simulated. Digital signal processing (DSP) of the voltage and current data from the simulation was done in Matlab. By analyzing the DSP output signals, the fault detection methods were developed.

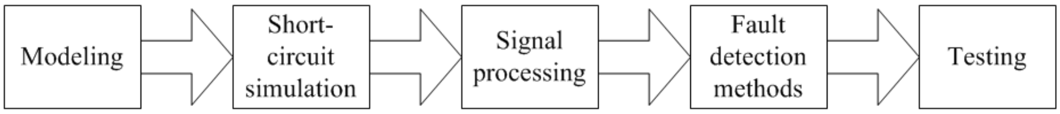

Figure 1: Research methodology

2.1 Wind farm study system

The studied system consists of 9 WTGs only placed on 3 feeders, each feeder having 3 WTGs. The number of WTGs was limited to 9 only because of long simulation time taken by PSCAD/EMTDC. This study system having 9 WTGs offers reasonable complexities that a real system would.

This study considered wind farm with two different types of WTGs technologies, DFIG (Type 3) or FCG (Type 4). A wind farm with mixed configuration, i.e. having both DFIG and FCG was not considered.

2.2 Short-circuit simulation

This study considered balanced three-phase to ground fault only. Although the three-phase faults do not occur frequently, these faults give most severe fault conditions. The most frequent faults are single-phase to ground faults. If the single-phase to ground fault is not cleared due to some reason, this may eventually develop into a three-phase fault.

The faults in AC collection grid only were considered. The fault inside WTG or HVDC-link was not considered in this study because these faults are the responsibility of the respective vendors and is also outside the scope of this project.

2.3 Digital signal processing

The voltage and current signals obtained from the short-circuit simulation studies were processed using DSP techniques and the peak value of the voltage and current, the fundamental component of voltage and current, the harmonic contents, the derivative of the voltage and current. In addition the instantaneous active power and impedance were also computed.

2.4 Fault detection methods

The fault detection methods were proposed based on the information obtained from the DSP analysis for the AC collection grids with DFIG and FCG turbines. The trip logics were built by selecting the useful signal from the DSP output information.

2.5 Testing of fault detection methods

The fault detection logics were tested on the studied system implemented in PSCAD/EMTDC environment. These logics were able to detect the fault in the AC collection grid.

3 Simulation setup

3.1 Case study

The case study is depicted in Figure 2. Radial wind farm collection grid is considered, since it is the most popular configuration for wind farm collection grid. The distance between wind turbines is equal to 1 km, while between each rows is equal to 1.5 km. The rating of each wind turbines are 3 MW and the rating of the HVDC is equal to 27 MVA.

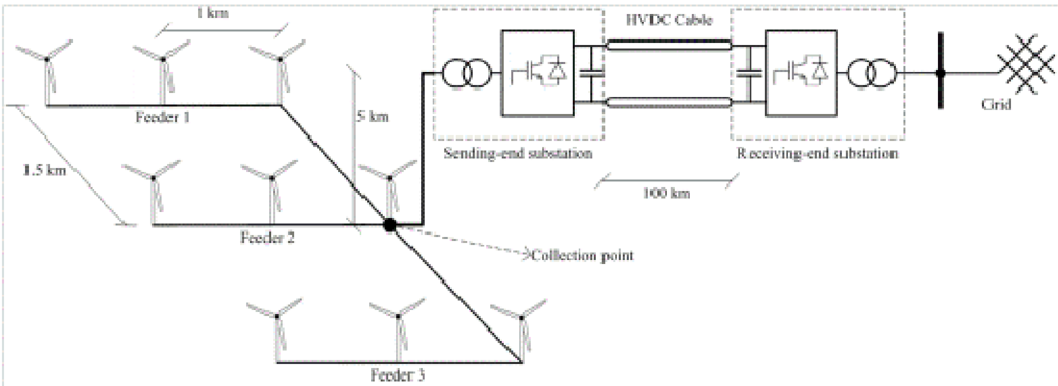

Figure 2: The case study system layout

All wind turbines in Figure 2 are equipped with FCGs or DFIGs and connected to the 50Hz 35 kV wind farm collection grid. The DC voltage level used in the HVDC transmission system is 115 kV. The infinite grid is a 50 Hz 130 kV source.

The cable size connecting each part of the system is chosen based on its current rating and voltage rating. A 3 x 95 mm^2 XLPE cable is used to connect each FCG, while 5 km of 3 x 400 mm^2 XLPE cable is used to connect the collection point to the HVDC station. The specification of the XLPE cable is given in Table 1.

Table 1: The ABB XLPE cable specification (Cu conductor) [0]

Cross-section area	Current rating	R	L	C
(mm^2)	(A)	Ω/km	mH/km	μF/km
95	275	0.193	0.69	0.17
400	515	0.047	0.57	0.28

3.2 Components Modeling

3.2.1 DFIG wind turbine model

The typical configuration of DFIG wind turbine is depicted in Figure 3. The stator of the DFIG is connected directly to the point of common coupling (PCC) via transformer, while the rotor is decoupled from the grid by means of back to back converter. By having the converter in the rotor of DFIG, the rotor current can be controlled allowing variation in electromagnetic torque and machine excitation. The rating of the power electronic converter is between 15 – 30% of the generator capacity [0].

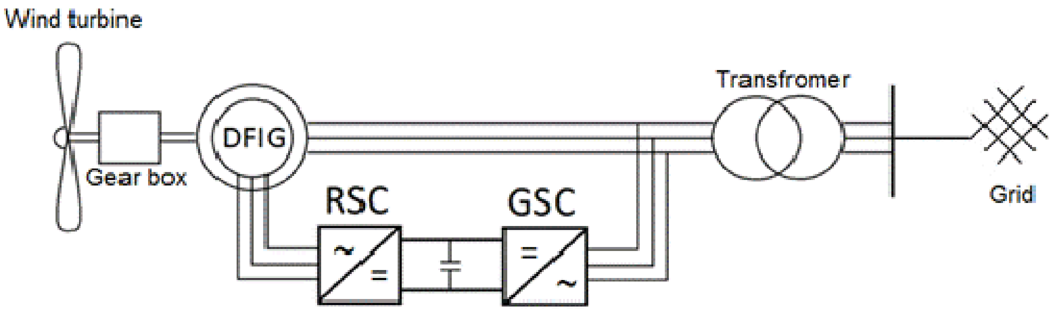

Figure 3: DFIG wind turbine model

As in fixed speed wind turbine, the generator in DFIG wind turbine system is driven by the wind turbine through gear box. The gear box is used to convert low rotational speed of the wind turbine into high speed rotational speed of the generator. As stated in [0], the common gear box ration for a 2-3 MW wind turbine is around 80 – 100.

3.2.1.1 Aerodynamic model

Power extraction from wind by wind turbine can be calculated using Betz equation given as:

$$P_m = \frac{1}{2}\rho A v_w^3 Cp(\lambda, \beta) \quad (0)$$

where P_m is the turbine mechanical power, ρ is the air density, A is the blade swept area, v_w is the wind speed, Cp is the power coefficient of the blade, and β is the blade pitch angle (BPA). The value of tip speed ratio (TSR) or λ can be calculated using (0)

$$TSR = \frac{\omega R}{v_w} \quad (0)$$

where ω is the turbine rotor angular speed, and R is the turbine blades radius.

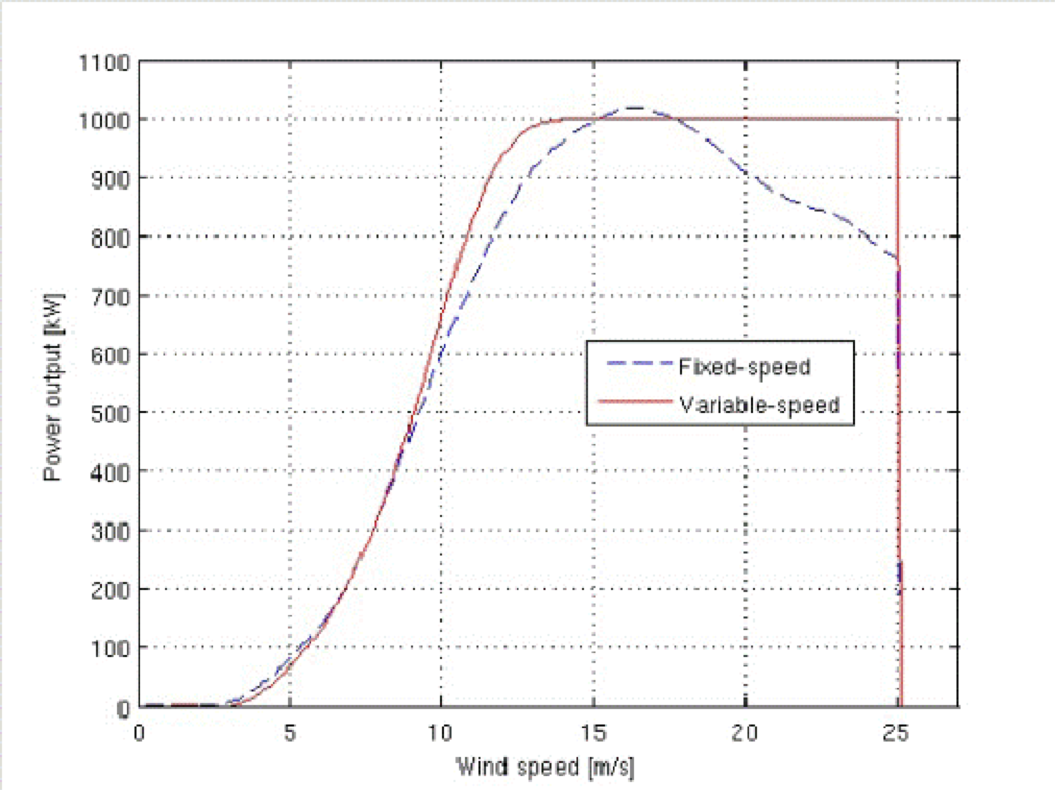

Figure 4: A typical wind turbine power curve

From (0), Cp is a nonlinear function of λ and β, and depends on the turbines structure. The λ value of fixed-speed wind turbine cannot be controlled and it gives the optimum Cp only for particular wind speed. With variable-speed wind turbine, Cp can be optimized to maximize power extraction for wide range of wind speed [0]. A typical power curve of fixed and variable-speed wind turbine is shown in Figure 4. An example of numerical approximation of Cp is given by [0] in the following form:

$$Cp(\lambda,\beta) = 0.73\left(\frac{151}{\lambda_i} - 0.58\beta - 0.002\beta^{2.14} - 13.2\right)e^{-\frac{18.4}{\lambda_i}} \qquad (0)$$

where

$$\lambda_i = \left(\frac{1}{\lambda - 0.02\beta} - \frac{0.003}{\beta^3 + 1}\right)^{-1} \qquad (0)$$

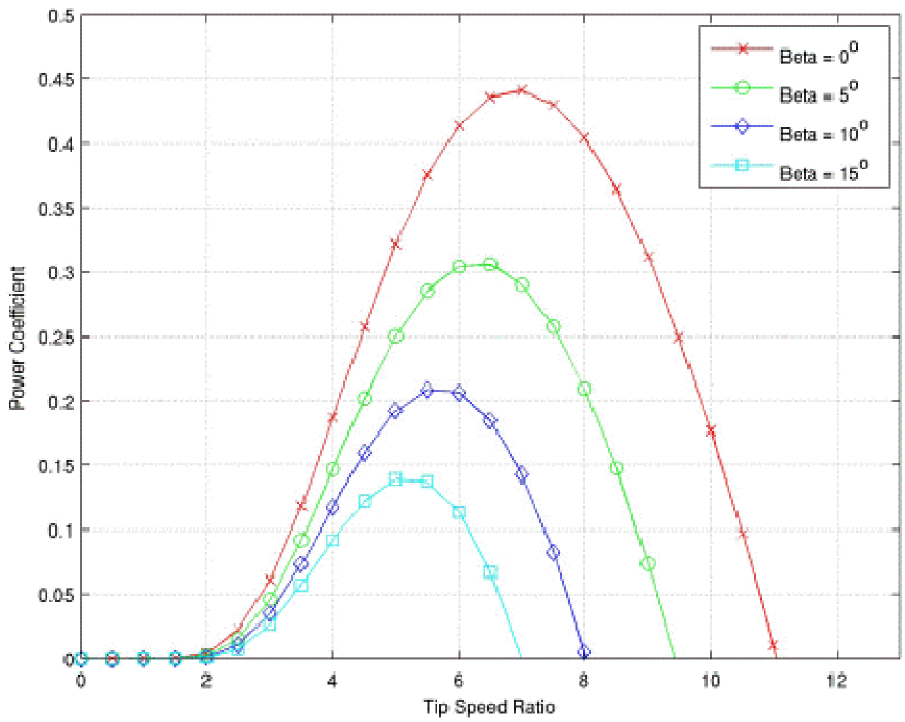

Figure 5: $\boldsymbol{Cp}$-$\boldsymbol{\lambda}$ curve for different $\boldsymbol{\beta}$

From (0), if v_w is invariable then P_m is directly proportional to Cp. It can be seen from Figure 5 that in order to maximize power extraction from the wind, β must be at the minimum and λ must be at the optimum (within 6-8). Since the wind speed in this study is assumed to be constant during simulation time, the pitch angle control of the wind turbine blade is not implemented (β is assumed to be zero).

3.2.1.2 Doubly-fed induction generator

As can be seen in Figure 3, the rotor of the DFIG can be accessed via slip ring and connected to the back to back converter; therefore the rotor is not short-circuited as in squirrel-cage induction machine ($u_r \neq 0$). The equivalent circuit of a DFIG is depicted in Figure 6 and the stator and rotor voltage equations can be written as follow.

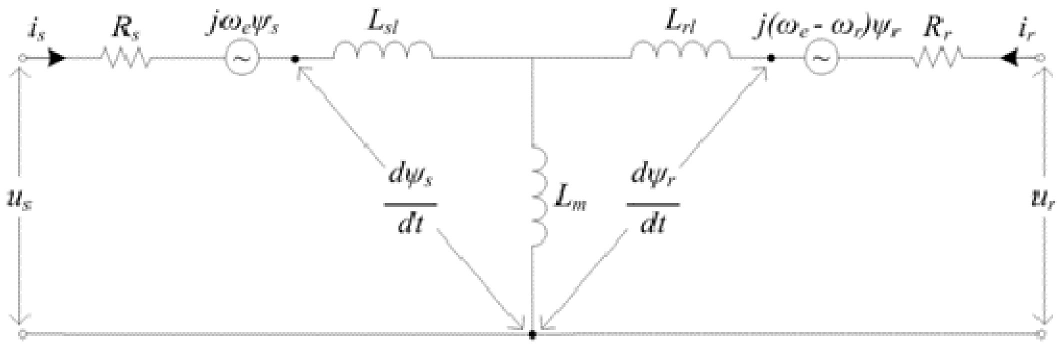

Figure 6: Equivalent circuit of DFIG

$$u_s = i_s R_s + j\omega_e \psi_s + \frac{d\psi_s}{dt} \qquad (0)$$

$$u_r = i_r R_r + j(\omega_e - \omega_r)\psi_r + \frac{d\psi_r}{dt} \qquad (0)$$

where u, i, R and ψ denote the voltage, current, resistance and flux quantity, respectively, while ω_e is the synchronous speed and ω_r is the rotor rotational speed. The subscripts s and r refer to quantities of the stator and rotor, respectively.

The relationship between the current and the flux are given in the following equations.

$$\psi_s = i_s L_s + i_r L_m \qquad (0)$$

$$\psi_r = i_r L_r + i_s L_m \qquad (0)$$

where L_m is the magnetizing inductance and L_s and L_r are the stator and rotor inductance, respectively. The rotor and stator inductance can be determined using the following equations.

$$L_s = L_{sl} + L_m \qquad (0)$$

$$L_r = L_{rl} + L_m \qquad (0)$$

where L_{sl} and L_{rl} are the leakage inductance of the stator and rotor, respectively.

The mechanical equation of the DFIG can expressed as follows:

$$J\frac{d\omega_r}{dt} = T_m - T_e \qquad (0)$$

where J is the moment inertia of the rotor, and T_m is the mechanical torque. The electrical torque (T_e) is given by equation (0).

$$T_e = Im\{\psi_s^* i_s\} \qquad (0)$$

The complex power is given as

$$S = u_s^* i_s + u_r^* i_r \qquad (0)$$

The parameters of the DFIG can be found in Appendix 1.

3.2.1.3 Back to back converter

The converters in a DFIG are placed between the rotor circuit and the step-up transformer connected to the grid. Two 6-pulse IGBT back to back converters control up to two values in the DFIG. In this study the rotor-side converter (RSC) controls the reactive power flow at the DFIG and the rotational speed of DFIG, while the grid-side converter (GSC) controls the DC-link voltage and the reactive power injection to the grid. The configuration of the converter is depicted in Figure 7.

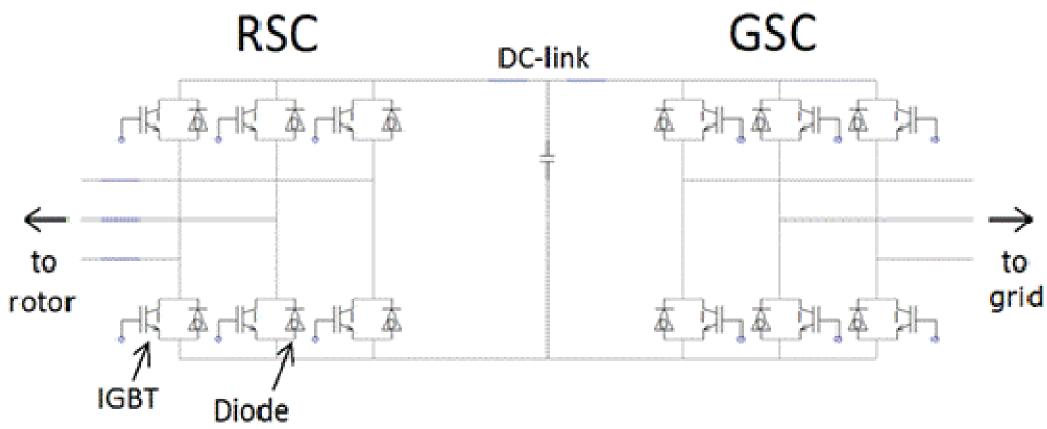

Figure 7: Electrical scheme for the back to back converters in the DFIG

The voltage transfer characteristics of the back to back converter are calculated as

$$V_s = m_1 \frac{\sqrt{3}E_{dc}}{2\sqrt{2}} \qquad (0)$$

$$V_r = m_2 \frac{E_{dc}}{2\sqrt{2}} \qquad (0)$$

where V_s and V_r are the output voltage of the GSC and RSC respectively, m_1 and m_2 are the modulation indexes of the GSC and the RSC respectively, and E_{dc} is the DC-link voltage [0].

RSC control scheme

The RSC controller is based on the *dq* rotating frame with *d*-axis rotating synchronously with the stator flux. The rotor voltage equation can be written in the following equations [0].

$$v_{dr} = R_r i_{dr} + \sigma L_r \frac{d}{dt}(i_{dr}) - (\omega_e - \omega_r)\sigma L_r i_{qr} \qquad (0)$$

$$v_{qr} = R_r i_{qr} + \sigma L_r \frac{d}{dt}\left(i_{qr}\right) + (\omega_e - \omega_r)(L_m i_{ms} + \sigma L_r i_{dr}) \qquad (0)$$

where σ is the leakage factor, and i_{ms} is the magnetizing current. Both parameter can be calculated as

$$\sigma = 1 - \frac{{L_m}^2}{L_s L_r} \qquad (0)$$

$$i_{ms} = \frac{L_s}{L_m} i_s + i_r \tag{0}$$

The stator flux angle (λ) is calculated from

$$\lambda_{\alpha s} = \int (v_{\alpha s} - R_s i_{\alpha s)} dt \tag{0}$$

$$\lambda_{\beta s} = \int (v_{\beta s} - R_s i_{\beta s)} dt \tag{0}$$

$$\theta_s = \arctan\left(\frac{\lambda_{\beta s}}{\lambda_{\alpha s}}\right) \tag{0}$$

where θ_s is the stator-flux vector position. From the following equation

$$T_e = -3\frac{P}{2} L_m i_{ms} i_{qr} \tag{0}$$

the torque is proportional to i_{qr} and can be regulated using v_{qr}. The rotor excitation current i_{dr} controls the reactive power flowing to or from the stator circuit and is controlled using v_{dr}. The RSC control scheme is depicted in details in Figure 8.

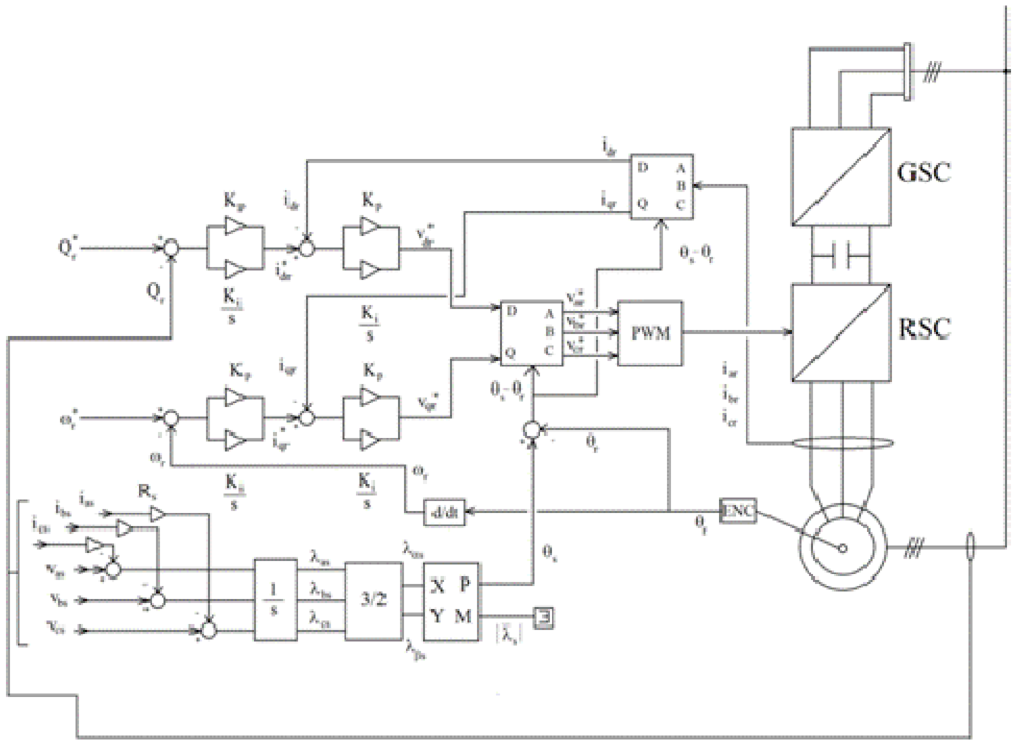

Figure 8: Control scheme for RSC

The reference three-phase voltages coming from the control unit (named $v_{ar}^*, v_{br}^*, v_{cr}^*$) are then used for generating RSC firing pulse. This means that the firing pulses for the IGBTs are created out of the comparison with a triangular carrier wave at a high frequency (2 kHz) and the desired output voltage of the converter.

The RSC current output can be limited to some value ($i_{r,lim}$) by limiting one of $i_{dr,lim}$ or $i_{qr,lim}$ and adjusting the other. In this study, d-axis rotor current is adjusted in order to allow an increase of the reactive power transferred to the DFIG, as formulated in (0) and (0).

$$i_{qr,lim} = i_{r,lim} \qquad (0)$$

$$i_{dr,lim} = \sqrt{{i_{qr,lim}}^2 - {i_{qr}}^2} \qquad (0)$$

DC-link Capacitor

The rating of the capacitance has been obtained considering that

$$C = \frac{S \cdot \Delta t}{\frac{1}{2} \cdot {E_{dc}}^2} \qquad (0)$$

where Δt is the time needed to charge the capacitor from zero to rated voltage E_{dc} if the converter is supplied with a constant power equal to S [0]. The choice of Δt depends on many factors, such as the ripples of current and the transient over-voltages. It is common to choose a value of 1 ms / 2 ms, therefore the value of the capacitance from (0) is $C = 1500\ \mu F$

GSC control scheme

The objective of the GSC is to keep constant the DC-link voltage, regardless of the magnitude and direction of the rotor power. The rotating *dq*-frame is also implemented in the GSC control with the *d*-frame is aligned with the grid voltage. The PWM converter is regulated with the *d*-axis current used to regulate the DC-link voltage and the *q*-axis current component used to regulate the reactive power injection to the grid.

In the *d*-*q* reference frame rotating at ω_e the following is obtained:

$$v_{ds} = R_s i_{ds} + L_s \frac{d}{dt}(i_{ds}) - \omega_e L_s i_{qs} + v_{ds1} \qquad (0)$$

$$v_{qs} = R_s i_{qs} + L_s \frac{d}{dt}(i_{qs}) + \omega_e L_s i_{ds} + v_{qs1} \qquad (0)$$

where L_s is the stator inductance and v_{ds1} and v_{qs1} are the *d*- and *q*-components of v_{as1}, v_{bs1}, v_{cs1}.

The active and reactive power flow is given by

$$P = 3(v_{ds} i_{ds} + v_{qs} i_{qs}) \qquad (0)$$

$$Q = 3(v_{qs} i_{ds} + v_{ds} i_{qs}) \qquad (0)$$

The angular position of the supply voltage is calculated as

$$\theta_e = \int \omega_e dt = \arctan\left(\frac{v_\beta}{v_\alpha}\right) \qquad (0)$$

where v_α and v_β are the α-β (stationary two axis) stator voltage components.

Since the d-frame is rotating synchronously with the stator voltage, then v_{qs} is equal to zero and, since the amplitude of the supply voltage is constant, v_{ds} is constant. Therefore the active and reactive power will be proportional to i_{ds} and i_{qs} respectively [0].

Power flow dynamic in the DC-link is shown by Figure 9, where P_{Gen} is the power coming in to DC-link, P_{Grid} is the power coming out from the DC-link, and P_{Cap} is the power flowing to the capacitor (C).

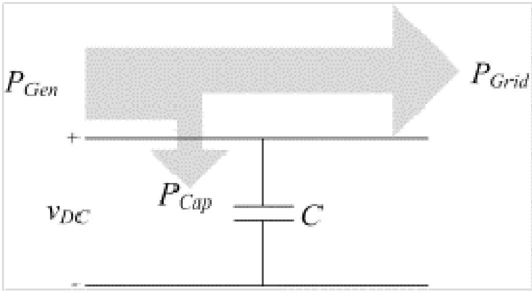

Figure 9: Power flow dynamic in the DC-link

The power flow into capacitor can be written as follows:

$$v_{DC} \times C \frac{dv_{DC}}{dt} = P_{Gen} - P_{Grid} \quad (0)$$

By assuming that P_{Gen} is constant and P_{Grid} depends on i_{ds} (from (0)), equation (0) shows that the DC-link voltage can be controlled via i_{ds}. The control scheme thus utilizes current control loops for i_{ds} and i_{qs} with the i_{ds} demand being derived from the DC-link voltage error through a standard PI controller, while the i_{qs} demand determines the reactive power flowing to or from the GSC to the grid and, together with the reactive power from the stator windings controlled by the RSC, represents the total amount of reactive power injected to or absorbed from the grid. In this way there is a complete control of the reactive power.

The detailed control scheme for the GSC is shown below.

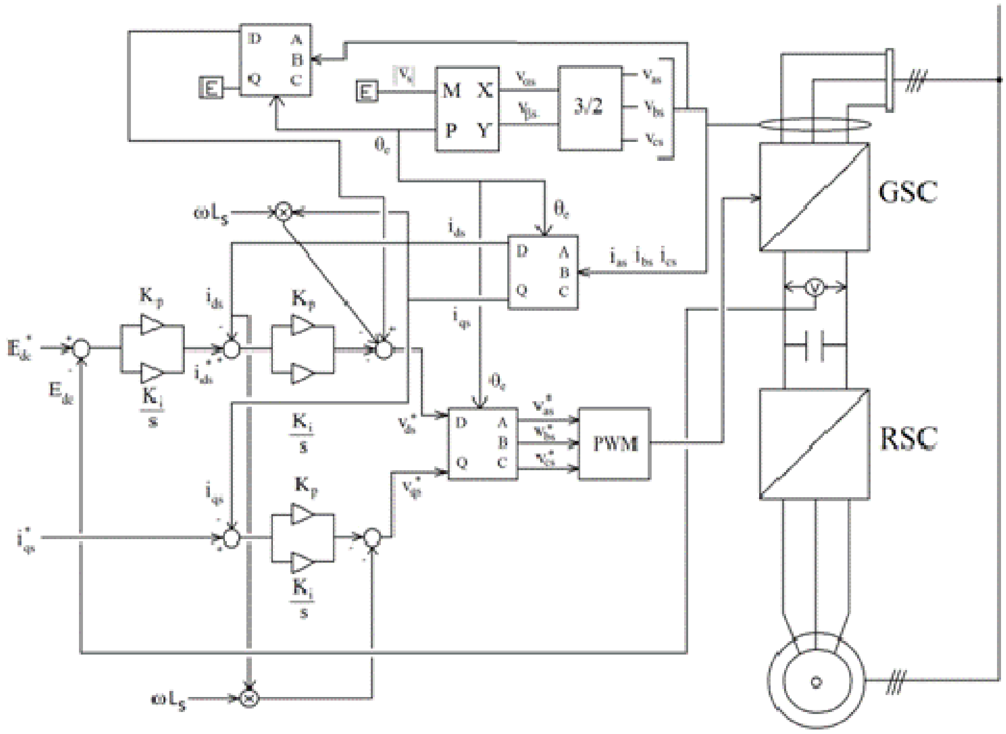

Figure 10: Control scheme for GSC

3.2.1.4 Crowbar

When a fault occurs outside the DFIG terminals, high currents flow from the stator to the fault location, with its value depending on the electrical impedance between these two points. Because of the electro-magnetic coupling between the stator and the rotor, high currents appear also in the rotor windings, which may damage the converters. That is why a crowbar is used to disconnect the rotor converter from the generator during faults.

Whenever a fault occurs, a signal triggers the switch (named “CBs” in Figure 11) on the DC resistance, so that the current flows on it. At this condition, the DFIG operated as wound rotor induction generator and only the RSC is disconnected, while the GSC is still injecting the reactive power to the grid.

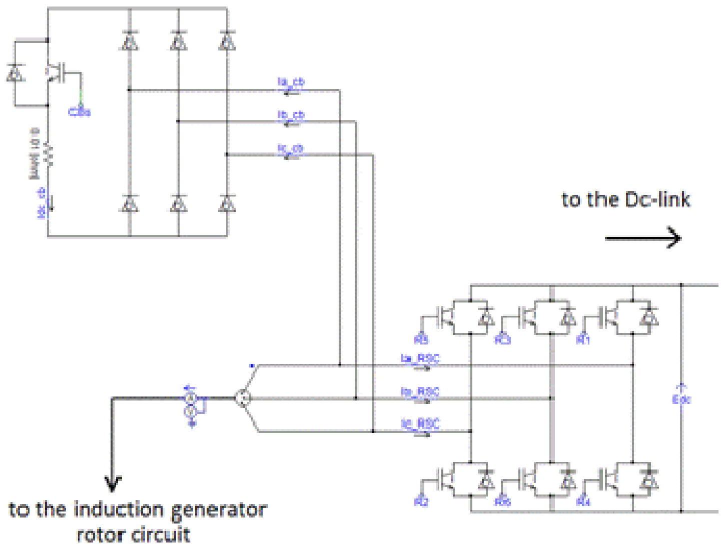

Figure 11: Electrical scheme for the crowbar used in the DFIG model

In this study, the current threshold for the crowbar is 25% above the nominal rotor current.

3.2.2 FCG model

Figure 12 shows the typical configuration of FCG with a permanent magnet synchronous generator (PMSG) and six-pulse IGBT back to back converter. The generator-side converter is used to control the PMSG speed in order to maximize the wind power extraction by optimizing the TSR of the wind turbine.

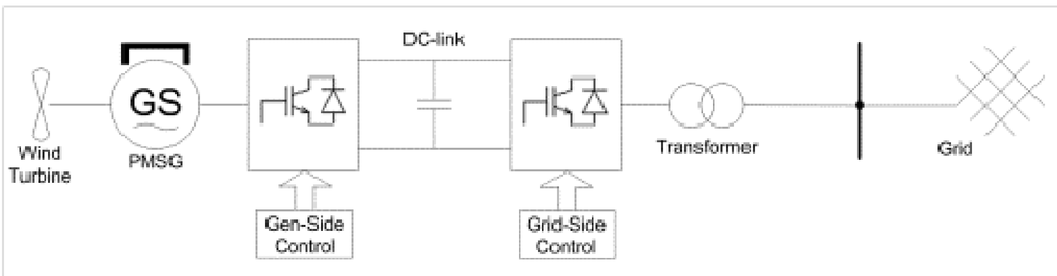

Figure 12: PMSG with back-to-back PWM converter

3.2.2.1 Permanent Magnet Synchronous Machine model

The PMSG is modeled in dq-representation assuming that it has sinusoidal flux distribution in the air gap and no zero components in the three phase quantities. The transformation from three-phase quantities to dq-axis is done by aligning the d-axis to the rotor flux as depicted in Figure 13.

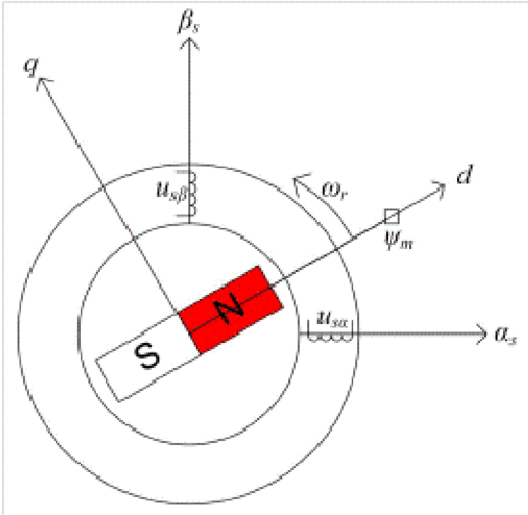

Figure 13: Simple $\boldsymbol{dq}$-axis representation in 2 poles PM machine

The stator voltage equation can be expressed as:

$$\begin{aligned} u_{sd} &= R_s i_{sd} - \omega_r \psi_{sq} + \frac{d\psi_{sd}}{dt} \\ u_{sq} &= R_s i_{sq} + \omega_r \psi_{sd} + \frac{d\psi_{sq}}{dt} \end{aligned} \quad (0)$$

where u_{sd} and u_{sq} are the stator voltage in dq-axis, R_s is the stator resistances, i_{sd} and i_{sq} are the stator current in dq-axis, ω_r is the rotor electrical speed, ψ_{sd} and ψ_{sq} are the dq-axis representation of stator flux linkage. Flux linkage equations are given in (0) as follow:

$$\begin{aligned} \psi_{sd} &= L_{sd} i_{sd} + \psi_m \\ \psi_{sq} &= L_{sq} i_{sq} \end{aligned} \quad (0)$$

where L_{sd} and L_{sq} are the stator inductance in dq-axis. By inserting (0) to (0), stator voltage equations become:

$$\begin{aligned} u_{sd} &= R_s i_{sd} - \omega_r L_{sq} i_{sq} + L_{sd} \frac{di_{sd}}{dt} \\ u_{sq} &= R_s i_{sq} + \omega_r (L_{sd} i_{sd} + \psi_m) + L_{sq} \frac{di_{sq}}{dt} \end{aligned} \quad (0)$$

The rotor electrical speed (ω_r) in the previous equations can be calculated as follows:

$$\omega_r = \omega_m n_p \quad (0)$$

where n_p is the number of rotor pole pair. The mechanical angular speed (ω_m) can be expressed as a function of electrical torque (T_e) and mechanical torque (T_m) as given in the following equation:

$$J \frac{d\omega_m}{dt} = T_m - T_e - B\omega_m \quad (0)$$

where J is the moment inertia of the rotor, and B is the viscous damping.

The space vector representation of electrical torque (T_e) is given by the following equation:

$$T_e = \frac{3n_p}{2} Im\{\psi_s^* i_s\} \quad (0)$$

by inserting (0) into (0), electrical torque equation become:

$$T_e = \frac{3n_p}{2}(\psi_m i_{sq} + (L_{sd} - L_{sq}) i_{sd} i_{sq}) \quad (0)$$

It can be observed from (0) that there are two terms of torques which are synchronous torque and reluctance torque. The preceding is produced by the permanent magnet flux and q-axis current, while the later is produced by the difference of the inductance in dq-axis [0].

3.2.2.2 Generator-side converter model

Field Oriented Control (FOC) scheme is implemented in this study to control the PMSG. This control scheme relies on the transformation of three-phase quantities into two coordinate system (dq-representation), so that it similar to DC machine control. The transformation is implemented by aligning the d-axis to the rotating stator flux.

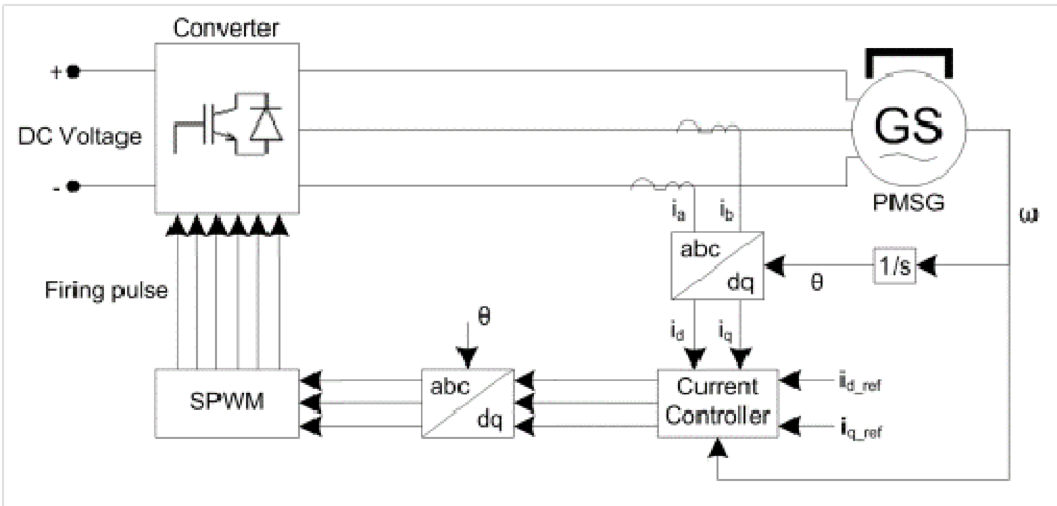

Figure 14: Basic scheme of FOC for PMSG

Figure 14 represent the scheme of FOC. The current reference of the current controller in Figure 14 can be obtained from the outer controller which regulates the speed of PMSG.

As explained in [0] and [0], different control strategies can be applied. In this study, full torque control strategy is implemented. In order to maximize the torque, current reference in d-axis is always set to zero. The phasor diagram of this control strategy can be seen in Figure 15.

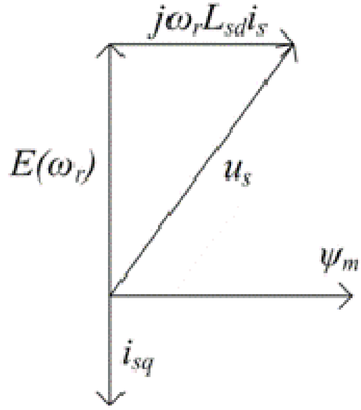

Figure 15: Phasor diagram of full torque control strategy

By inserting current value from Figure 15 into (0), the electrical torque equation can be written as:

$$T_e = \frac{3n_p}{2}(\psi_m i_{sq}) \tag{0}$$

From (0), it can be observed that the value of i_{sq} is linear to the value of T_e, which simplify the control property [0].

The structure of the current and speed controller of PMSG is represented in Figure 16.

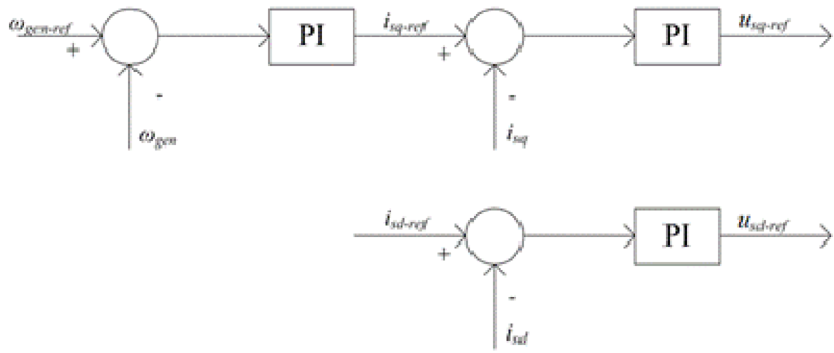

Figure 16: PMSG control structure

The q-axis control consist of outer controller (speed controller) and inner controller (current controller). The inner controller in both d and q-axis have the same properties. As a rule of thumb in control design, the inner controller bandwidth is at least 10 times faster than the outer one.

3.2.2.3 DC-link model

DC-link voltage level

The minimum value of DC voltage level in the back-to-back converter to avoid the sinusoidal pulse width modulation converter from being saturated is given as follows:

$$v_{DCmin} = \frac{2\sqrt{2} \cdot v_{l-l}}{\sqrt{3}} \quad (0)$$

where v_{DCmin} is the minimum DC voltage and v_{l-l} is the rms line to line voltage of the converter output [0]. It is common to use modulation index of the converter (m) less than 0.9 for commercial application [0], therefore (0) become:

$$v_{DCmin} = \frac{2\sqrt{2} \cdot v_{l-l}}{\sqrt{3} \cdot m} \quad (0)$$

The value of v_{l-l} is usually assumed to be equal to the maximum allowable voltage (105 percent of the nominal voltage).

DC-link capacitor

The current waveform flowing from the generator-side converter contains harmonics, which will introduce ripple in the voltage waveform. The control of the converter require a constant DC value, therefore it is needed to reduce the DC voltage ripple by using a capacitor. The amplitude of voltage ripple depends on the capacitance and switching frequency of the converter.

Selection of capacitor size is usually a trade-off between amplitude of voltage ripple and capacitor time constant [0]. A large capacitor can reduce DC-link voltage ripple, but it has slow response to the voltage change. On the other hand, a small capacitor allows fast control of DC-link voltage at the expense of higher DC-link voltage ripple. The DC time constant (τ) or Δt can be calculated using (0).

In the wind power technology applications, the capacitor size of back-to-back converter depends also on the fault ride-through (FRT) strategy of the FCG.

FRT strategy

Similar to the DFIG converter, power flow dynamic in the DC-link is shown by Figure 9. During normal condition (assuming no power losses in DC-link), P_{Gen} is equal to P_{Grid} and there is no stored energy in the capacitor (P_{Cap}=0). In the event of a grid fault, P_{Grid} is rapidly reduced ($P_{Grid} \approx 0$) but due to the fact that mechanical dynamic is slower than electrical dynamic, P_{Gen} cannot be reduced quickly to keep P_{Gen}=P_{Grid}, therefore P_{Cap} is no longer zero.

This excess power from generator accumulates in the capacitor resulting in rapid increase in DC-link voltage. Overly DC-link voltage can destroy both capacitor and converter; therefore action must be taken to avoid system failures. In [0] several types of FRT strategies are discussed. In this study, only over-dimensioned DC-link capacitor and full power braking resistor are applied since both methods are giving the best dynamic performance [0]. Typical value of DC-link capacitor is approximately 55 to 270 μF per horsepower or 70 to 400 mF for a 2 MW wind turbine [0].

The amount of energy dissipated in the braking resistor is controlled by IGBT. It is called full power braking resistor, because the energy dissipated in the resistor is equal to the energy generated by the wind. The schematic diagram of full power braking resistor is depicted in Figure 17.

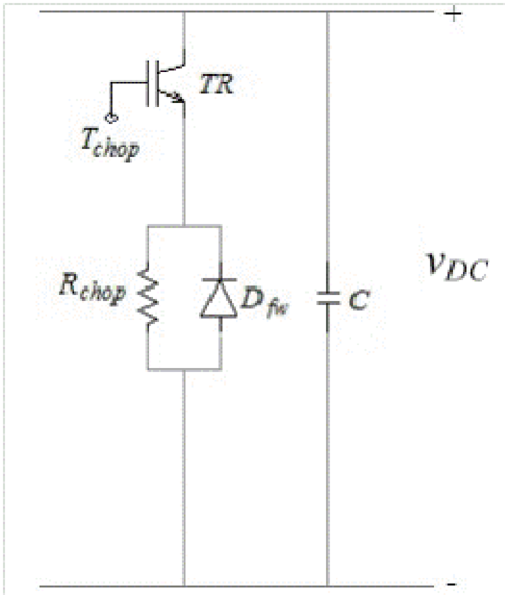

Figure 17: DC chopper schematic

In Figure 17, the switch TR will conduct only if the DC-link voltage increase beyond the allowable limit (vary between 10 to 20 percent above the nominal voltage), and the power from generator is dissipated in the resistor R_{chop}. In the steady-state operation of FRT, the value of R_{chop} should be 1 per unit. There is no maximum limit of R_{chop}, but too large resistance will give large effects during fault clearance condition [0].

3.2.2.4 Grid side converter model

The purpose of the grid-side converter is to interface active and reactive power exchange between DC-link and AC grid. As can be seen in Figure 9, the DC-link voltage should be kept constant in order to maximize active power transfer to the grid, therefore DC-link voltage control is implemented in the grid-side converter. The reactive power support from FCG can be realized by controlling reactive current output from the grid-side converter [0], [0].

The grid-side converter control is based on the dq-frame rotating synchronously with the AC grid. The most beneficial factor of using vector control is that the AC voltage and current are represented in constant vectors, therefore PI controller can be used to remove static errors of the control system hence simplify the controlling scheme. Clark and Park power invariant transformation is used to transform three-phase quantities into dq-axis representation.

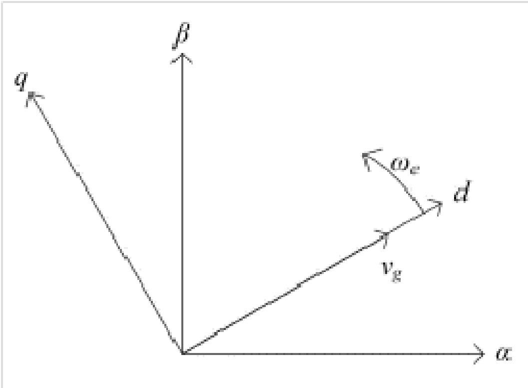

Figure 18: Transformation of axis for vector control

The transformation from stationary reference frame to rotational reference frame is shown in Figure 18, where ω_e represents the angular speed of AC grid.

The active power (p_g) and reactive power (q_g) transferred to the grid in dq-axis representation can be calculated as follows:

$$\begin{aligned} p_g &= \frac{3}{2}(v_{gd}i_{gd} + v_{gq}i_{gq}) \\ q_g &= \frac{3}{2}(v_{gq}i_{gd} - v_{gd}i_{gq}) \end{aligned} \tag{0}$$

where v_{gd} and v_{gq} represent the grid phase voltage magnitude in dq-axis, while i_{gd} and i_{gq} are the current that flow to the AC grid in dq-axis. In this study, the dq rotating frame is aligned with the grid voltage such that v_{gq} = 0 and v_{gd} = $|v_g|$, therefore (0) becomes:

$$\begin{aligned} p_g &= \frac{3}{2}(v_{gd}i_{gd}) \\ q_g &= \frac{3}{2}(-v_{gd}i_{gq}). \end{aligned} \tag{0}$$

As can be seen in (0), the active and reactive power can be controlled independently by controlling the dq current that flows to the grid.

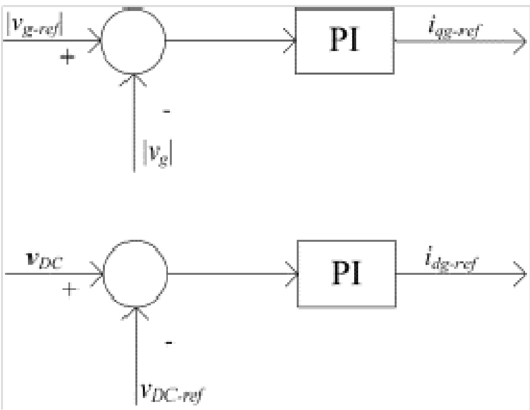

Figure 19: Grid-side converter control

The grid-side converter control structure is depicted in Figure 19. In this study, hysteresis current control is implemented to inject current into the grid. The diagram of hysteresis control can be seen in Figure 20.

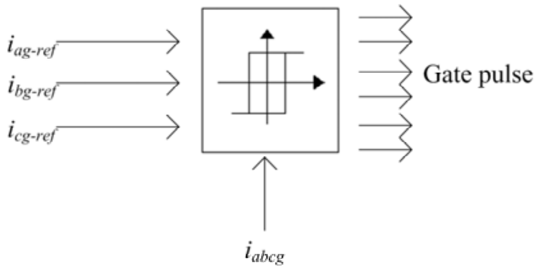

Figure 20: Hysteresis band current controller

The advantages of using hysteresis control are this control is simple to be implemented (control and PWM are combined), and it has quick response to reference change [0].

The converter current output can be limited by limiting one of i_{d-ref} or i_{q-ref} in Figure 19 and adjusting the other. In weak grid connected FCG, it is common to adjust d-axis current in order to allow an increase of the reactive power transferred to the grid, as formulated in (0).

$$\begin{aligned} i_{q-ref-max} &= i_{g-max} \\ i_{d-ref-max} &= \sqrt{i_{g-max}^2 - i_{q-ref}^2} \end{aligned} \tag{0}$$

3.2.2.5 Model simplification

As explained in the previous sub section, the speed control in the PMSG is usually realized by adjusting the output electrical torque with the mechanical torque from the wind turbine. The amount of the electrical torque depends on the permanent magnet flux, stator inductance, and stator current. Both flux and inductance are constant, while the stator current is controlled by the generator-side converter. The three phase stator current then rectified by the generator-side converter into DC quantity. If the wind speed is constant and the TSR of the wind turbine is at the optimum value, the current injected to the DC-link is also constant. Therefore, the FCG model depicted in Figure 12 can be simplified into the one depicted in Figure 21.

In the simplified FCG model, the aerodynamic, PMSG, and the generator-side converter are represented by a DC current source.

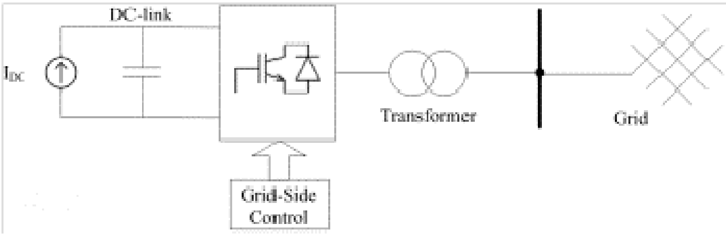

Figure 21: Simplified model of FCG

3.2.3 HVDC model

The VSC-HVDC transmission system is primarily composed of two converter stations and DC cables as depicted in Figure 22.

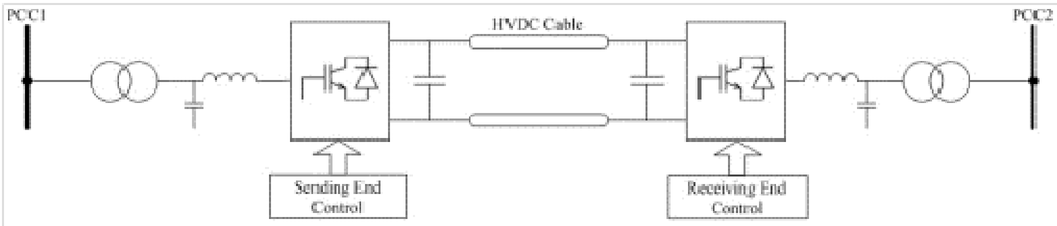

Figure 22: VSC-HVDC transmission system

Each converter station consist of an IGBT-VSC, phase reactor, filter, and transformer [0]. In this study, the sending-end HVDC (SE-HVDC) converter station is connected to the wind farm collection grid, while the receiving-end HVDC (RE-HVDC) converter station is connected to the main AC grid. The SE-HVDC converter station is used to maintain the wind farm voltage and frequency, while the RE-HVDC converter station is used to control HVDC voltage level and reactive power flow to the main AC grid. The SE-HVDC converter control is realized using sinusoidal PWM. The sinusoidal reference waveform has constant frequency and the magnitude is set so that the output voltage of SE-converter station equals to wind farm grid nominal voltage. The RE-converter is using the same control strategy as in the grid-side converter of FCG model which has been explained in section 3.2.2.4[0].

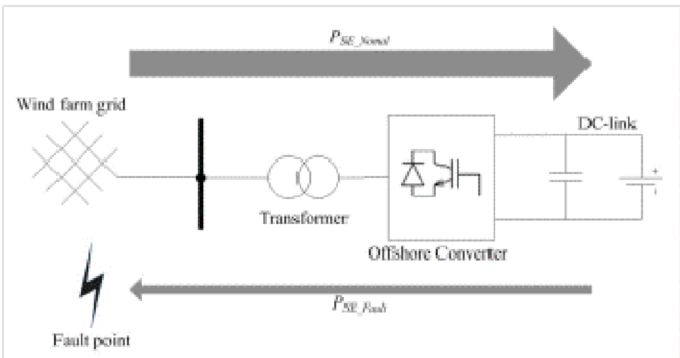

Figure 23: During normal condition, active power flows from wind farm grid to DC-link, while during fault in the wind farm grid, active power flows in reverse direction

When fault occurred in the wind farm collection grid, the magnitude and direction of the active power flow measured in the SE-HVDC converter is changed as depicted in Figure 23. Due to the safety reason of the converter, during short-circuit fault in the wind farm grid the SE-HVDC converter should limit it's short-circuit current contribution. There are two ways to achieve this limitation, the first one is to reduce the voltage reference in SE-HVDC converter [0], while the second one is to switch the SE-HVDC converter control from voltage-regulated mode in normal condition to current-regulated mode during fault [0].

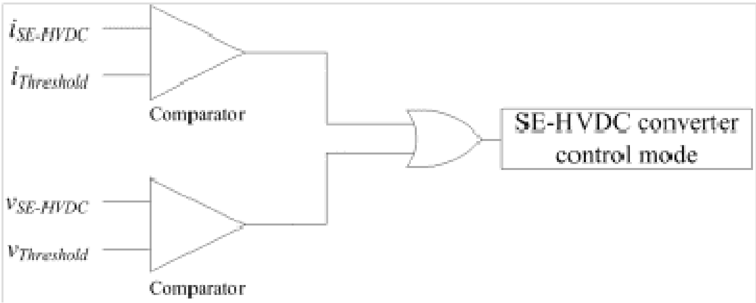

Figure 24: SE-HVDC converter control mode switch is implemented by sensing the instantaneous voltage ($\boldsymbol{v_{SE}}$) and current ($\boldsymbol{i_{SE}}$).

Figure 24 depicted the control mode alteration method in the SE-HVDC converter station. In Figure 24, instantaneous voltage (v_{SE}) and current (i_{SE}) are measured in the connection point of the SE-HVDC converter. If the measured peak current reach more than its threshold value (10% above nominal current) or the measured peak voltage goes below its threshold value (70% of nominal voltage), then the SE-HVDC converter change its voltage reference or alters from voltage source mode to current source mode. When current source mode is activated, SE-HVDC converter uses the same control strategy as explained in section 3.2.2.4.

3.2.4 Cable model

For a short AC transmission line (less than 35 km), pi line section model is used to represent the transmission line. This is because for a short transmission line, the propagation time is less than a simulation time step [0]. The pi line section model is depicted in Figure 25.

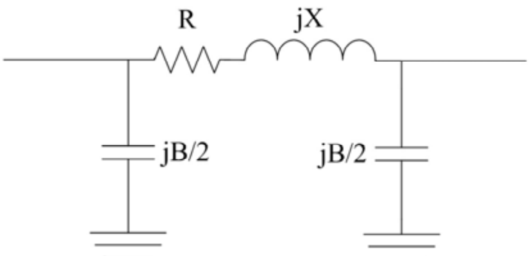

Figure 25: Pi line section model

In PSCAD/EMTDC, coupled pi line section component is used in this study, which means that the conductor voltages are always measured to true ground or earth [0]. The line data used in this study are given in Table 1.

The DC cable used in the HVDC system uses frequency dependant (phase) model to represents the DC cable. By using the frequency dependant (phase) model, the frequency response of a cable is duplicated using curve fitting method [0]. The geometry of the DC cable is given in Figure 26.

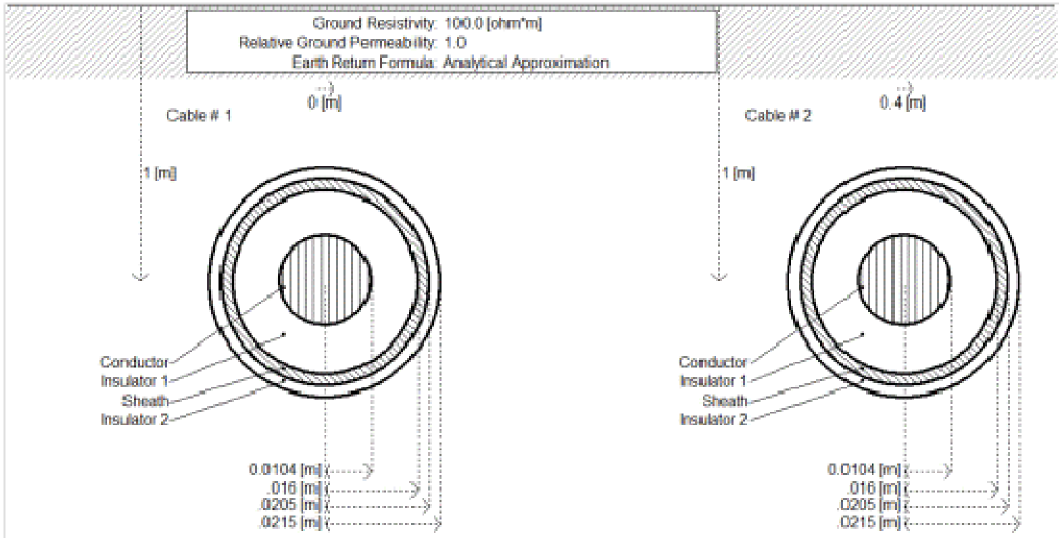

Figure 26: HVDC cable geometry implemented in PSCAD/EMTDC

3.3 Simulation scenarios

Three-phase to ground fault for different fault locations in the wind farm collection grid were simulated. The fault is located in the terminal of WTG as can be seen in Figure 27 and has a resistance (R_{fault}) of 0.001 Ω. The fault 1 is defined as the fault occurred in the terminal of WTG 1, and fault 2, 3, 4, 5, 6 respectively.

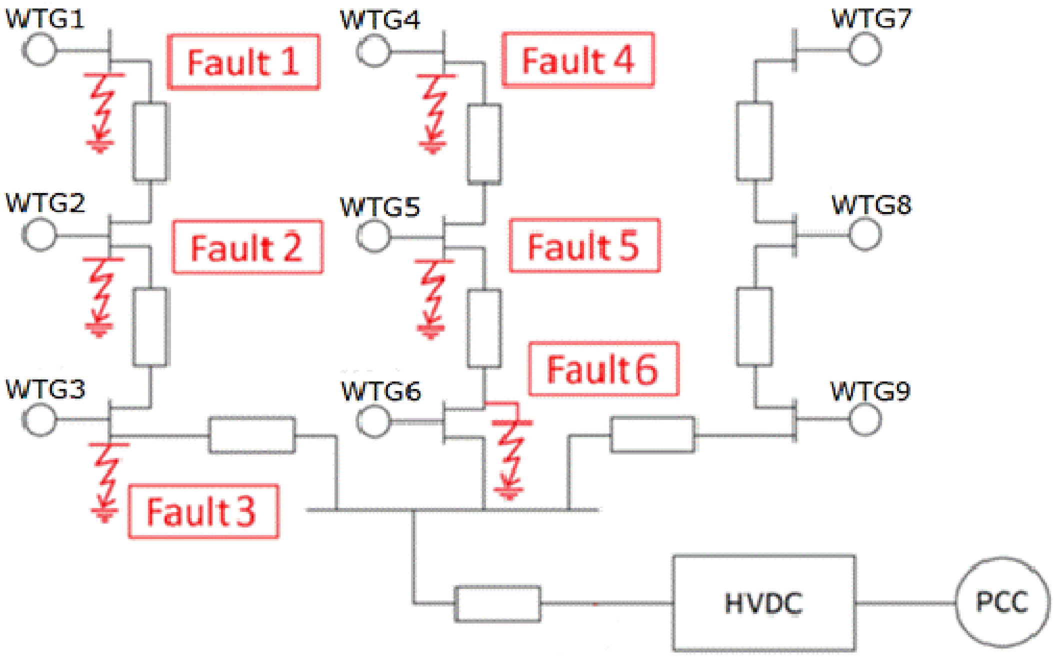

Figure 27: Different fault locations for the short-circuit simulation

As the base case, all WTGs are producing power at their rated capacity and short-circuit current contribution from WTG and HVDC are equal to 10% above their rated current.

Typical protection zones in wind farm are explained in [0]. Since the fault is assumed to occur only in the wind farm collection grid, the affected zones are the collector feeder relay zone (feeder line) and the collector bus relay zone (collection point) as can be seen in. In the collection point, the voltage and current measurement units are placed in point a, b, c, and d depicted in Figure 28. In the first feeder line, the voltage and current measurement units are placed in point e, f, g and in the second feeder line, the voltage and current measurement units are placed in point g, h, c.

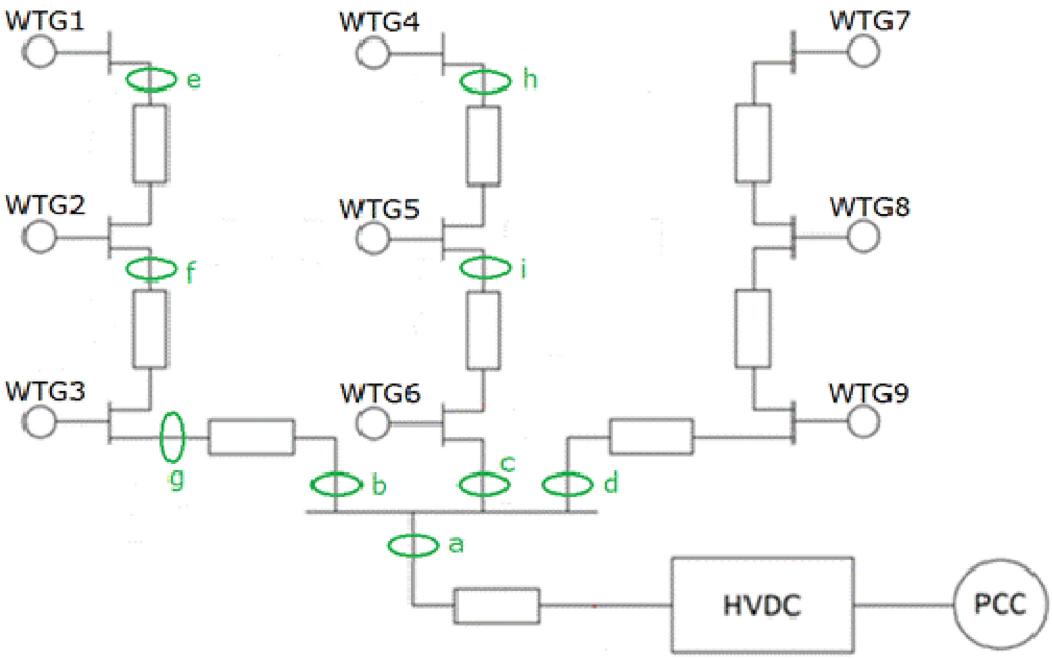

Figure 28: Voltage and current measurement units in collection point are placed in point a, b, c, d; and measurement units in feeder line are placed in point e, f, g or h, i, c

The terms "section" within a feeder line means the line section between two contiguous measurement points, for example: between measurement point e and f.

3.4 DSP analysis

In this study, the DSP is done for one data window. Figure 29 illustrates the moving rectangular data window when new sample is included and the oldest one is discarded.

The window width used in this study is equal to one cycle of the power frequency (20 ms). The DSP methods used in this study are instantaneous peak value, DFT analysis, instantaneous active power (p_{inst}), differential value, and positive sequence line-ground (L-G) impedance (Z) [0]-[0].

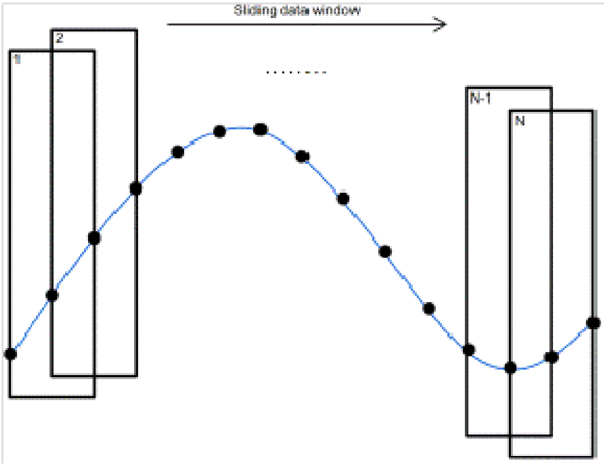

Figure 29: Sliding data window method

Instantaneous peak value (z_p), DFT analysis (Z_k), and differential value (z_{diff}) are calculated using the following equations.

$$z_p = \text{ } maximum\ of\ \ |z_k|_{k=0}^{N-1} \tag{0}$$

$$Z_k = \sum_{n=0}^{N-1} z_k e^{-j\frac{2\pi}{N}kn} \quad k = 0, \ldots, N-1 \tag{0}$$

$$z_{diff} = z_{k+1} - z_k \quad k = 0, \ldots, N-1 \tag{0}$$

where j denotes the imaginary unit, N is the number of the sample in one window, and z_k is the sampled signal. While instantaneous active power (p_{inst}), is calculated from instantaneous value of phase current (i) and voltage (v) and given as follows:

$$p_{inst} = \frac{1}{N}\sum_{n=0}^{N-1} v \cdot i \tag{0}$$

The result of the DFT analysis in (0) is the signal spectrums. By using the fundamental phase current ($I_{(1)}$) and voltage ($V_{(1)}$), positive sequence L-G impedance (Z) can be calculated as:

$$Z = \frac{V_{(1)}}{I_{(1)}} \tag{0}$$

By characterizing these DSP output the fault detection methods are proposed.

4 Simulation results with DFIG

4.1 Short-circuit simulation results and analysis

4.1.1 HVDC contribution to short-circuit currents

The first result shown here will be the current contribution of the HVDC during faults. The current at the AC side of the SE-HVDC is plotted, first with no current limiting strategy and then with the control scheme discussed on section 3.2.2.5 implemented. Results are shown in Figure 30 and Figure 31. In this case the results shown are the ones from the simulation of a fault within the wind farm ("Fault 1"). The faults are triggered at 2.025 s and this will be valid for all the subsequent simulations.

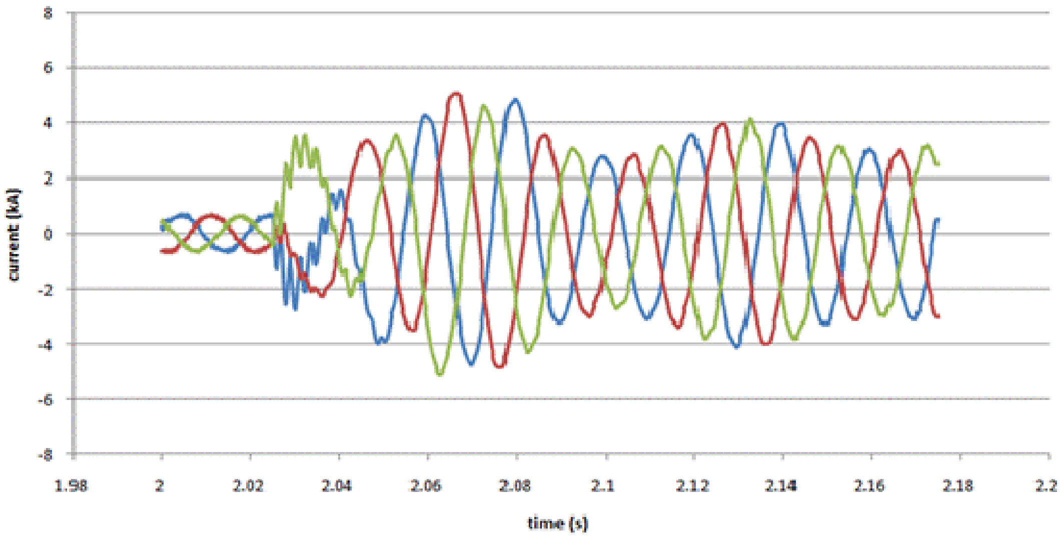

Figure 30: Current at SE-HVDC terminals during Fault 1 without current limitations at HVDC

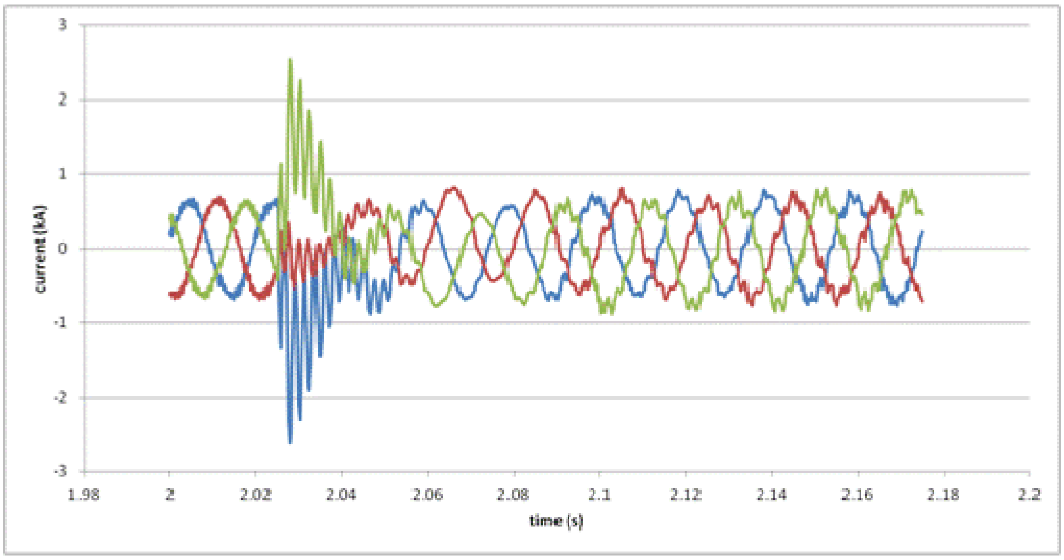

Figure 31: Current at SE-HVDC terminals during Fault 1 with current limitations at HVDC

As can be seen from the graphs, when the current limiting control is enabled, the amplitude of the current is strongly decreased. It is interesting to notice that however, in both faults, right after the fault the current is higher than the set value for the HVDC (here fixed at 1.1 pu): this is explained because the HVDC is still voltage controlled, only the reference voltage has changed, so it takes some time to decrease the voltage according to the PI regulation dynamics. During this time the current reaches a relatively high value and this maximum value appears even far from the HVDC terminals, for example at the wind turbines terminals.

4.1.2 Maximum peak currents during short-circuit

The first analysis will concern the maximum currents at the wind turbines terminals with different locations of the fault.

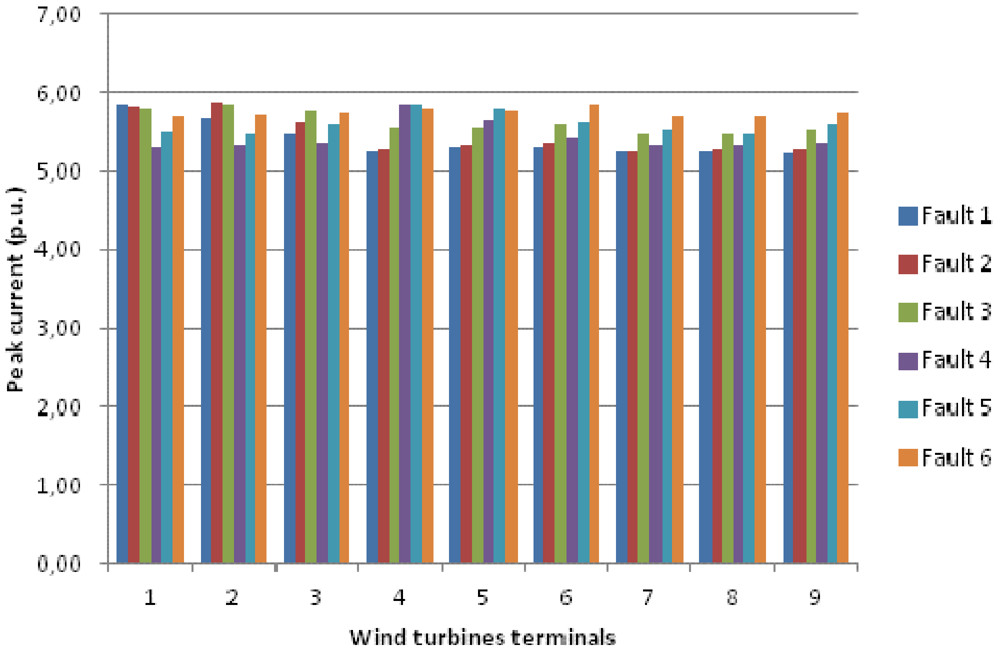

Figure 32: Peak currents (per unit values) at wind turbines terminals during faults

Figure 32 shows the maximum currents at each wind turbine terminals. Each group of bar refers to a single wind turbine and, in each group, different bars refer to different faults. It can be seen here that from wind turbine terminals it is impossible to determine where the fault is located, because the maximum currents are not differ the one from the other more than the 10% of their value (although it can be seen that the highest current always happens when the fault is located directly at the terminals of the considered wind turbine – for example in group bar number 3 the highest bar is the third).

The measuring of currents and voltages takes place also outside the wind turbines terminals, in particular it is interesting to observe the peak currents and their maximum values throughout the entire wind farm. Figure 33 shows the wind farm and represents these peak currents.

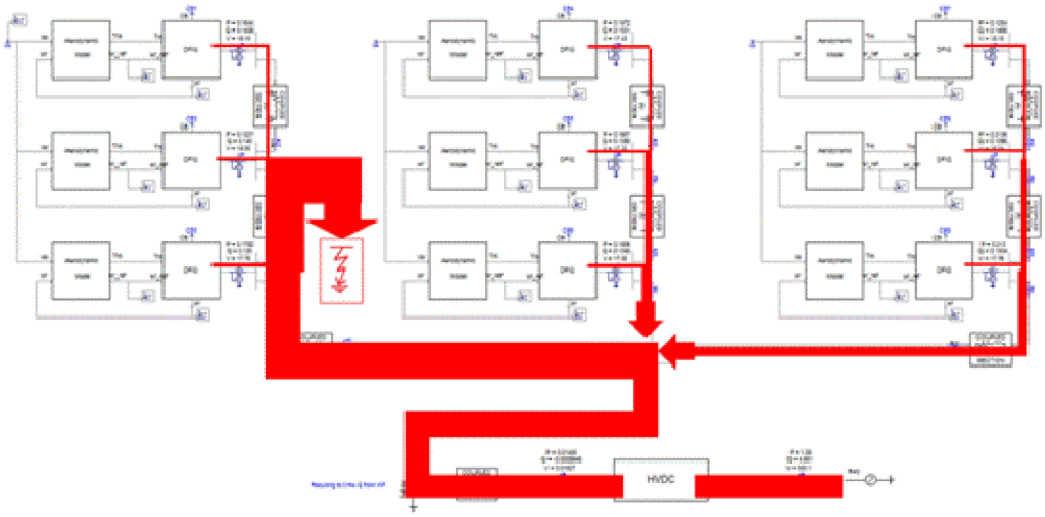

Figure 33: Maximum currents during Fault 2 represented as arrows where the width is proportional to the current amplitude

The width of the arrows represents the absolute amplitude (in kA) of the maximum peak of the currents while the direction of the arrows indicates the direction of current. In order to have the possibility to consider the arrows representatives also of the power flows, two conditions need to be fulfilled: the voltage on all the measuring points must be the same and the maximum peak currents must occur at the same time. The voltage of the wind farm during Fault 2 (the same fault of Figure 33) is shown in Figure 34.

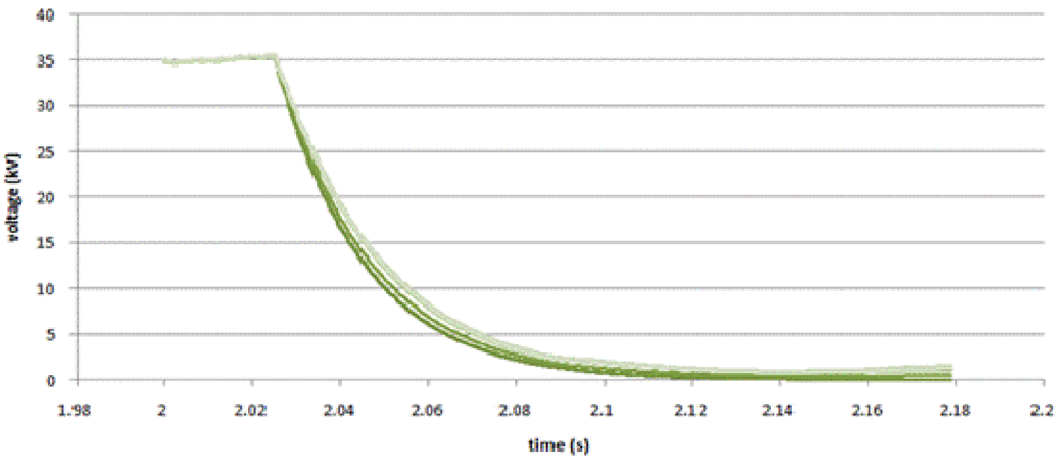

Figure 34: RMS line-to-line voltage at wind turbines terminals during fault

The voltage drop in all the wind turbines terminals is quite the same. The time instant when the maximum currents occur is always, for all the faults and all the measurements inside the wind farm, a value between 2.030 s and 2.035 s (from 0.005 s to 0.010 s after the fault). If the previous picture is zoomed at this time range the following picture is obtained.

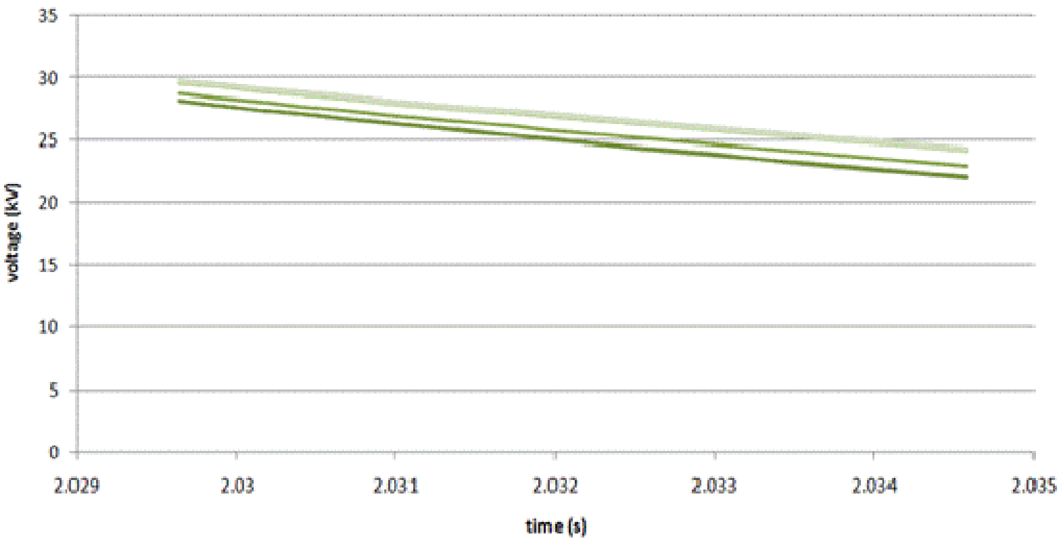

Figure 35: RMS line-to-line voltage at wind turbines terminals during fault – particular

The voltages are different as before, but the difference between the highest and the lowest voltage in the wind farm is less than 15% of the average value. Looking at these data the assumptions that the voltage is the same within the entire wind farm can be made. Arrows in Figure 33 can now be seen as power flows under the previous assumptions. It is now clear that a selectivity can be achieved observing the currents on the feeder instead of the ones from the wind turbines.

4.1.3 Peak values of current and voltage

It is now interesting to show the amplitude of the peak currents and voltages on the feeders for all the faults. The data will be arranged so that the peak value (current or voltage) will be displayed in a graph where the x-axis will represent the distance of the fault from the observation point, which for this case will be the main collector bus. The faults in the left feeder ("Feeder 1") and in the middle feeder ("Feeder 2") have been plotted in separate graphs for better understanding.

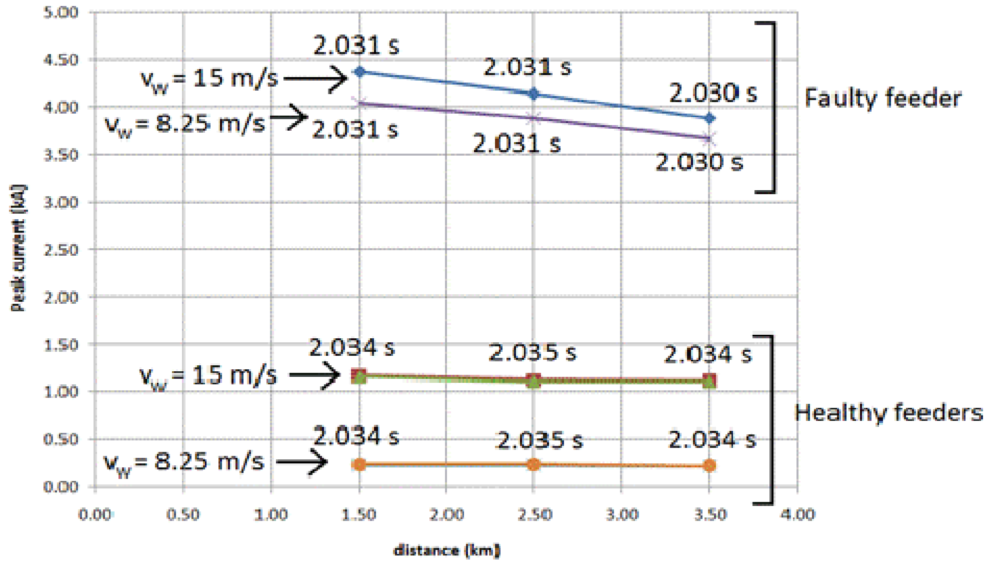

Figure 36: Peak currents for faults occurring on Feeder 1, plotted over distance between fault point and measuring point, time stamps of the peaks are also shown

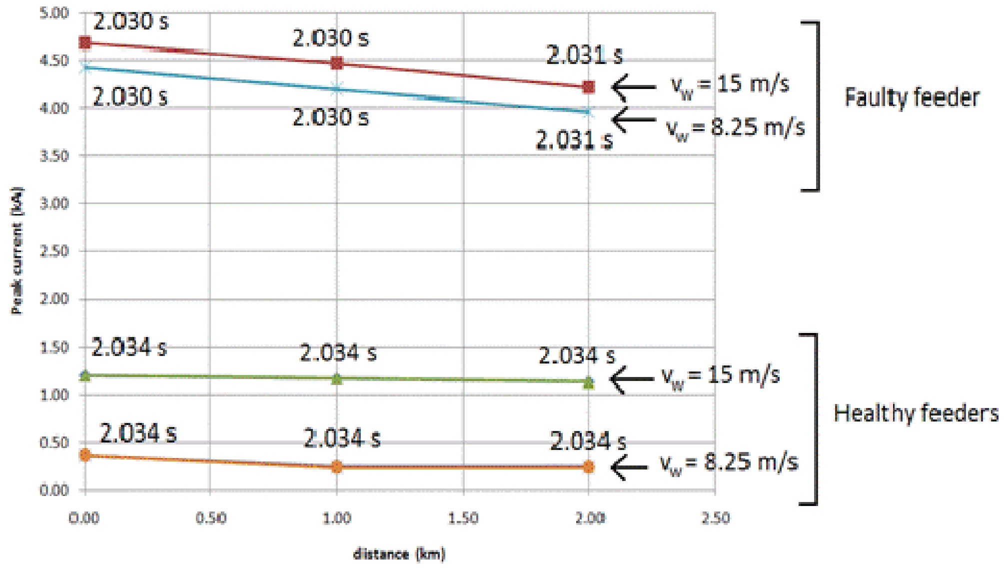

Figure 37: Peak currents for faults occurring on Feeder 2, plotted over distance between fault point and measuring point, time stamps of the peaks are also shown

The points represent the maximum peak values of the short-circuit current and each of them is labeled with the corresponding time instant. It can be seen that the faulty feeders present a peak current which is considerably higher and that happens almost a quarter of period before the healthy ones. Every short-circuit simulation has been performed at two wind conditions, at 15 m/s (nominal power) and at 8.25 m/s (20% of nominal power). With the increase of the fault distance from the observation point, it's possible to notice a decrease in the amplitude of the short-circuit current. However, such decrease is less than the 10% of the amplitude in the case of 15 m/s wind speed (and in the case of low wind speed the difference cannot even be appreciated from the graph): this behavior is not helpful for the detection of fault. The conclusions after observing these graphs are that it is possible to distinguish which feeder is healthy and which one is not, but it's impossible to determine where the fault is, within the faulty feeder, at least with these data. Finally, the difference in the wind speed affects in a relevant way only the fault currents in the healthy feeders, but in the faulty feeders the difference is only about 10%.

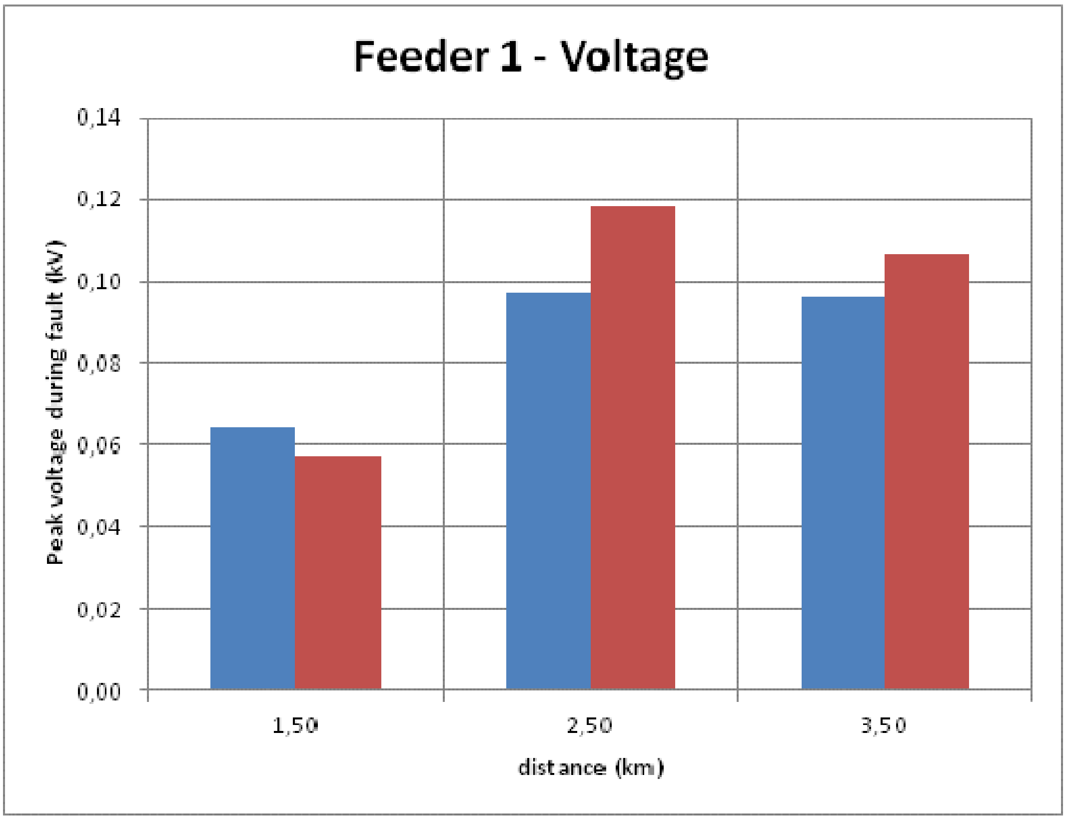

Figure 38: Voltage drops for faults occurring on Feeder 1, plotted over distance between fault point and measuring point, during high wind speed (blue) and low wind speed (red)

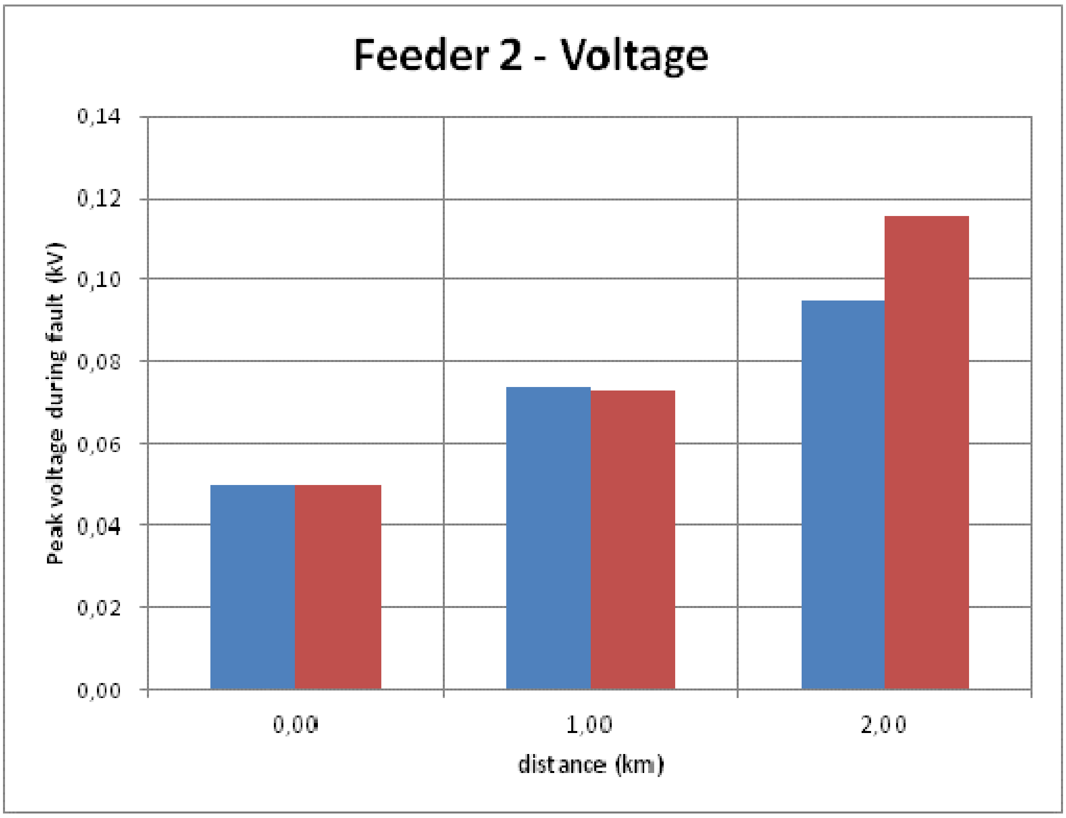

Figure 39: Voltage drops for faults occurring on Feeder 2, plotted over distance between fault point and measuring point, during high wind speed (blue) and low wind speed (red)

The voltage graphs shown in Figure 38 and Figure 39 are not giving any significant information for the fault identification. The voltage drops almost to zero in the entire wind farm, almost showing the same value at the specific time instant of Figure 38 and Figure 39. It is not possible to use the voltage to detect any more information than the presence of a fault within the system. The same considerations can be done, when analyzing the other observation point, the single feeder.

4.1.4 Maximum fault clearing time

Figure 40 shows the integral function of the current flowing through a cable. For the rating of cable connecting each WTGs, the current at the HVDC connection during fault 7 has been used. For the rating of cable connecting the collection point to the SE-HVDC terminal, the current on the cable between WTG 4 and 5 during fault 4 has been considered.

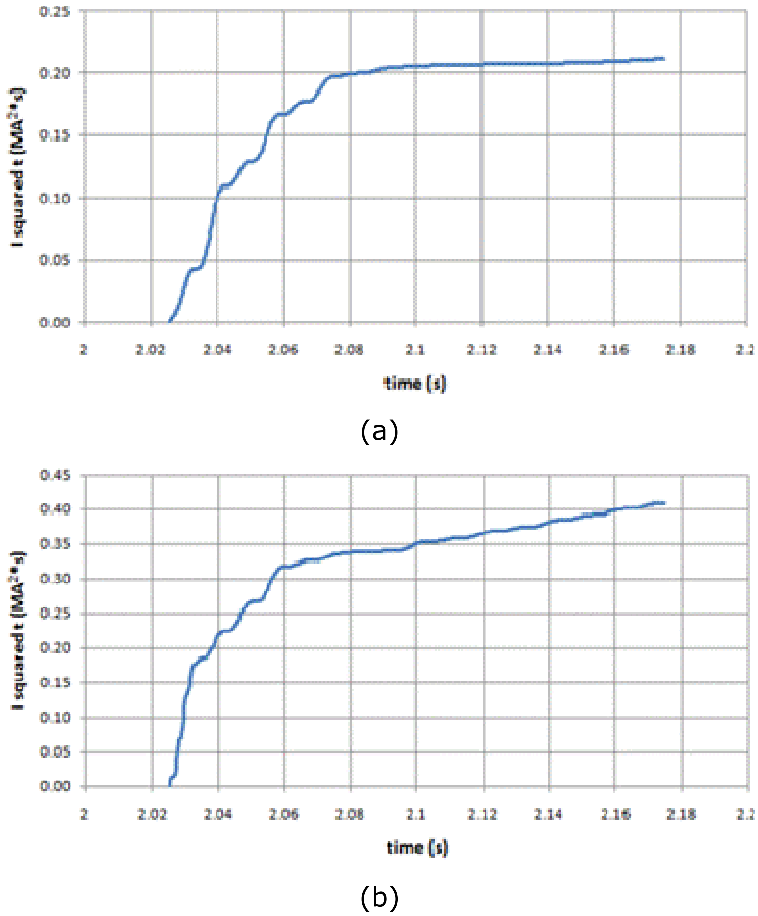

Figure 40: I squared t result for (a) cable connecting between wind turbine and (b) cable connecting collection point to the SE-HVDC terminal

Both cases represent the heaviest faults for each cable. The value of I_{lim} from [0] is:

$$I_{lim,A} = 62.7\ kA \tag{0}$$

$$I_{lim,B} = 14.9\ kA \tag{0}$$

Extrapolating the final slope from the graphs above, the time $(t_{max} - t_f)$ has been calculated as almost 5 minutes for cable used to connect each WTGs and 8 hours for cable used to connect from the collection point to the SE-HVDC terminal. Clearly the cables are not the component to worry about during faults.

There are some other dangerous phenomena that take place during a short-circuit other than the heating up of the cables. It has been observed during the simulation that the wind turbines speed up right after the appearing of a fault. This is mainly due to the energy from the wind which cannot be taken by the grid in faulty conditions, so such energy is stored in mechanical acceleration of the rotation of the blades. In the next graph it is shown the rotational speed of a wind turbine DFIG when a fault occurs.

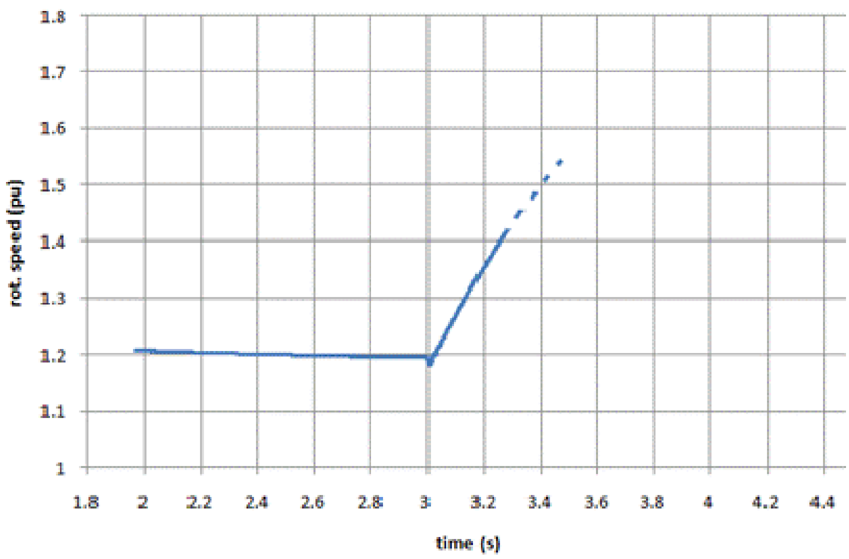

Figure 41: Rotational speed of wind turbine after fault at 3.0 s

As can be seen in Figure 41, the rotational speed of wind turbine reaches very high value (more than 1.4 p.u.) after 0.4 second from the instance of fault. This is because the overspeed protection of the DFIG is not implemented in the DFIG model.

4.2 Fault detection

4.2.1 Collection point

Many results have been processed by the sliding window for different fault positions to check which signals can be useful for the detection of the fault. The first analysis has been made on the currents flowing on the main collector bus and Figure **43**-Figure **45** show the example of processed signal with the respective color in which they appear in Figure **42**. At collection point the target is to find any signal output from the sliding window (SW) which identifies the feeder where the fault is (in this case is the left feeder – blue color lines).

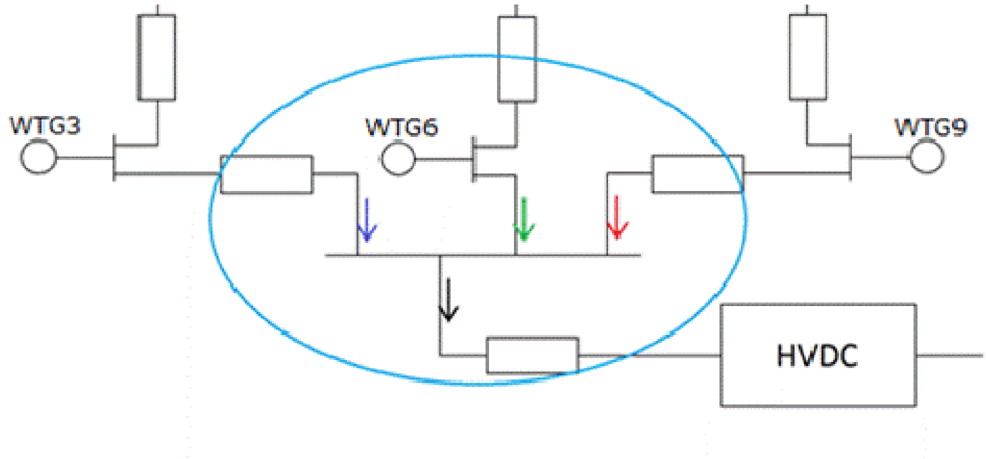

Figure 42: Collection point with measured quantities (the colors refer to the colors in the following graphs)

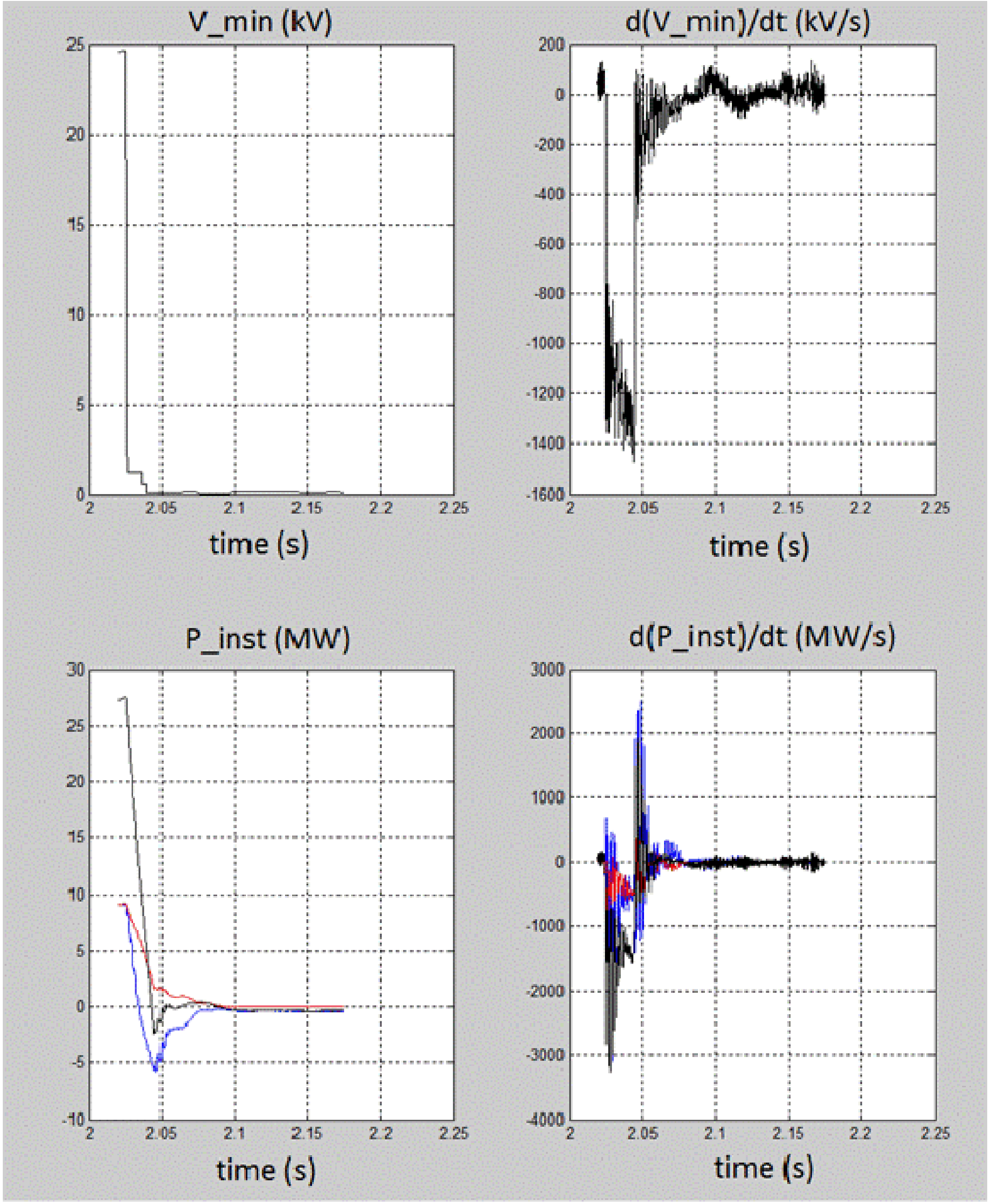

Figure 43: Minimum voltage and instantaneous active power (with respective derivatives) output by the SW during fault

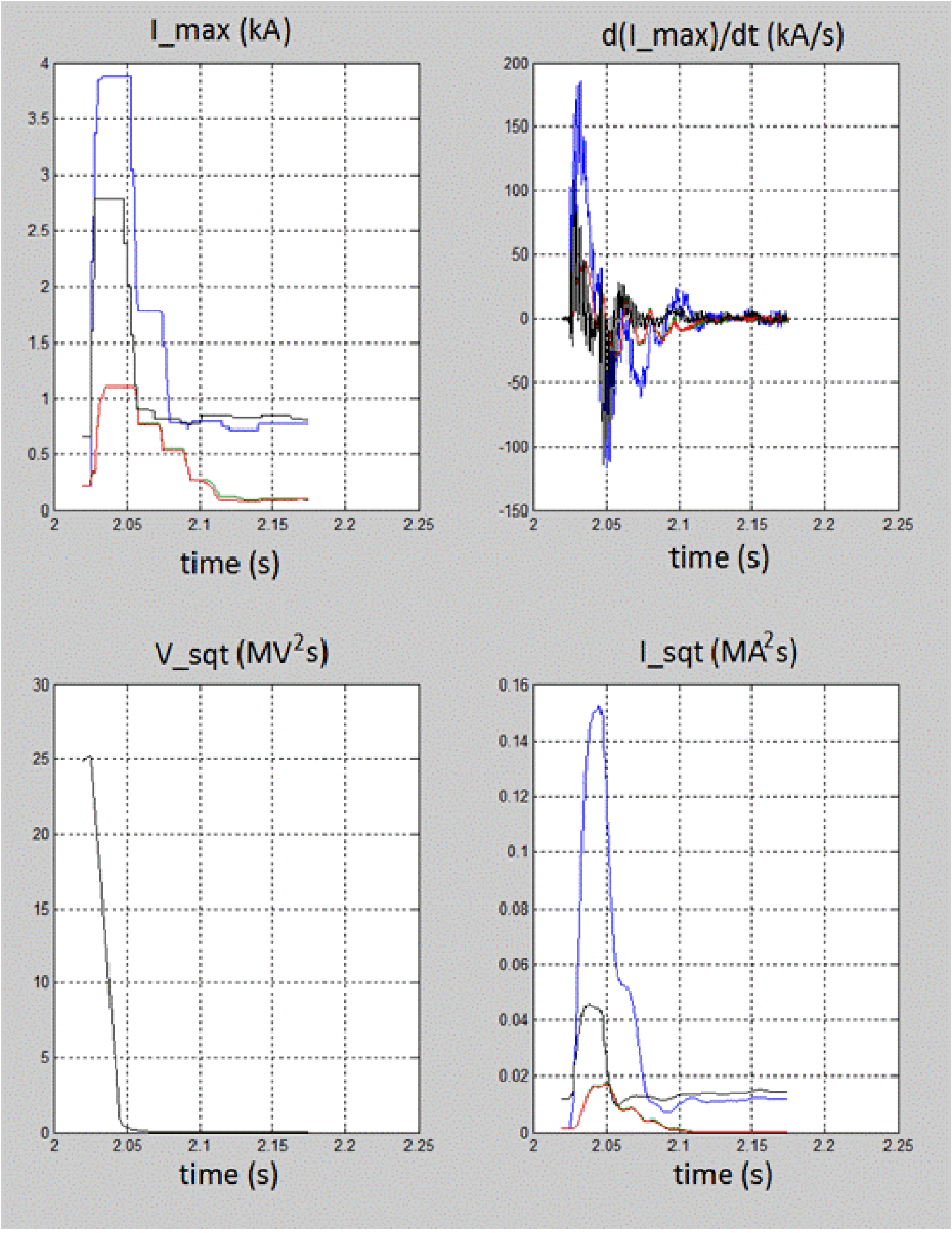

Figure 44: Maximum peak current, its derivative and integrated square voltage and current output by the SW during fault

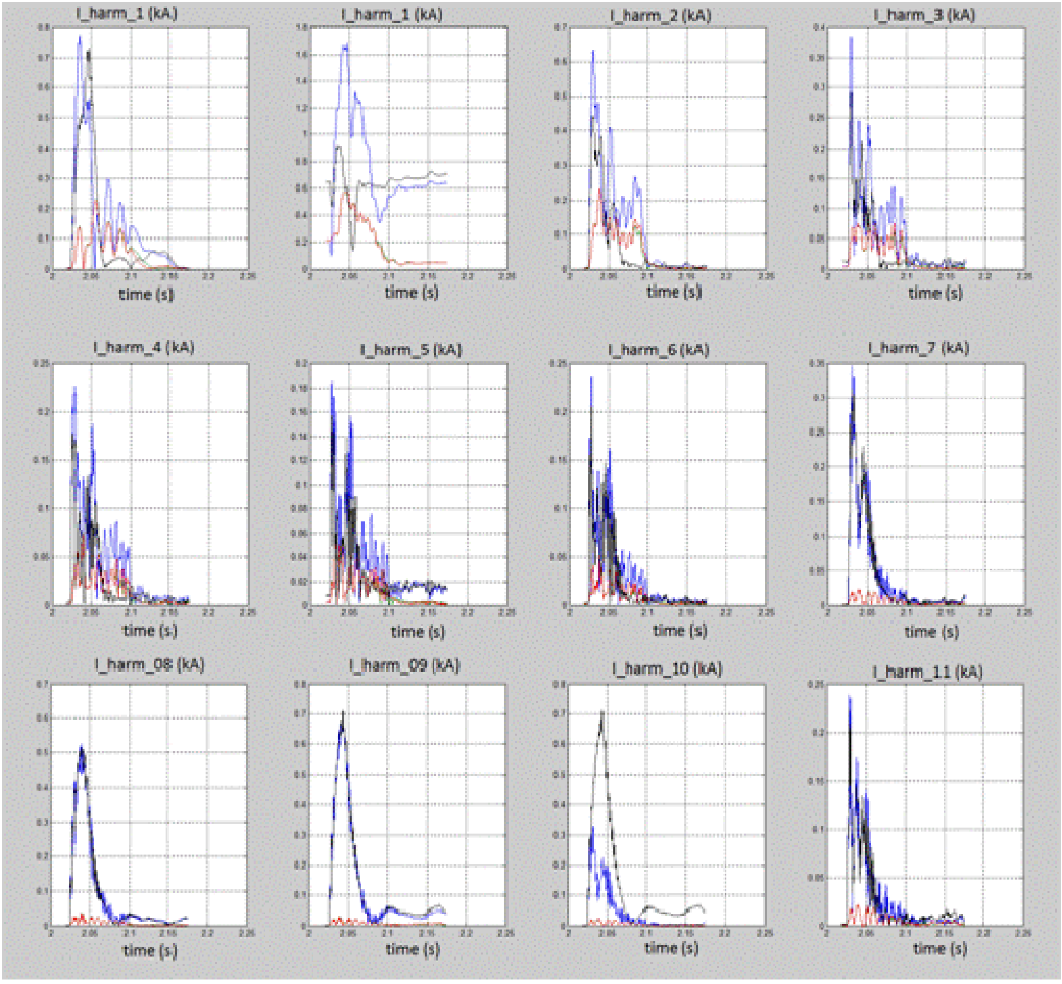

Figure 45: Current harmonic components output by the SW during fault

The derivative signals are not reliable as they show a behavior difficult to analyze due to their noise.

The voltage cannot help much because it falls down very rapidly and the signal is only one (not four, as the currents – one current each feeder plus the current flowing towards the HVDC).

The integrated square voltage and current quantities are not more useful than their peak counterparts.

Higher frequency harmonic (7^{th} to 11^{th}) content of the current is also useful for it shows very different values in the faulty feeder and in the HVDC branch in comparison to the healthy feeder.

Only instantaneous active power and peak current that can be used to differentiate between healthy and faulty feeder. Further results of both signals for different fault locations are presented in Figure 46 to Figure 57.

Instantaneous active power

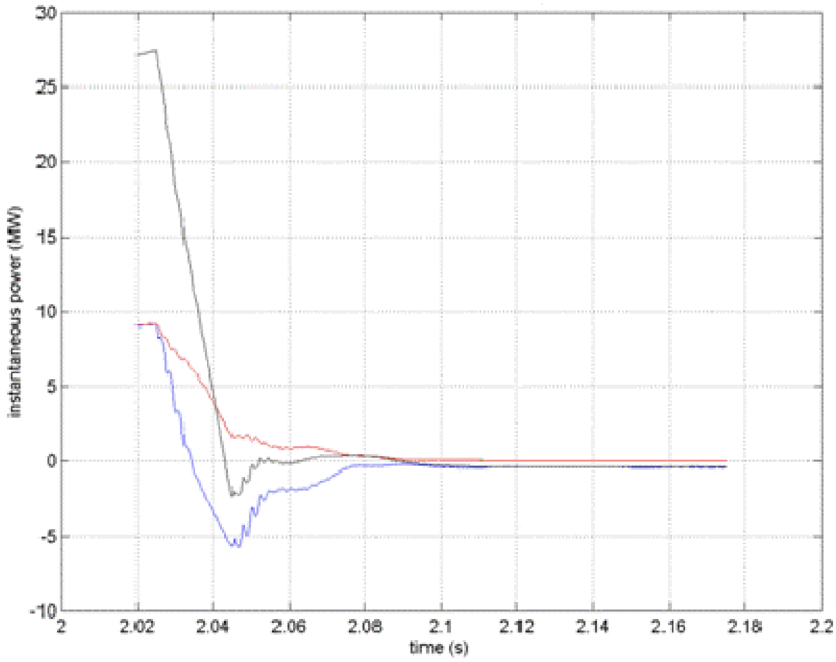

Figure 46: Instantaneous active power at collection point during Fault 1

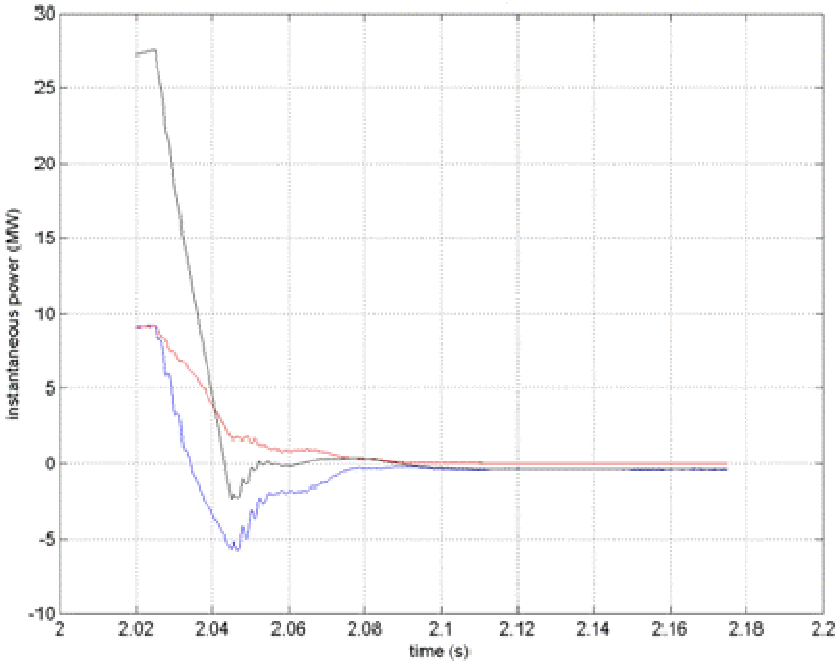

Figure 47: Instantaneous active power at collection point during Fault 2

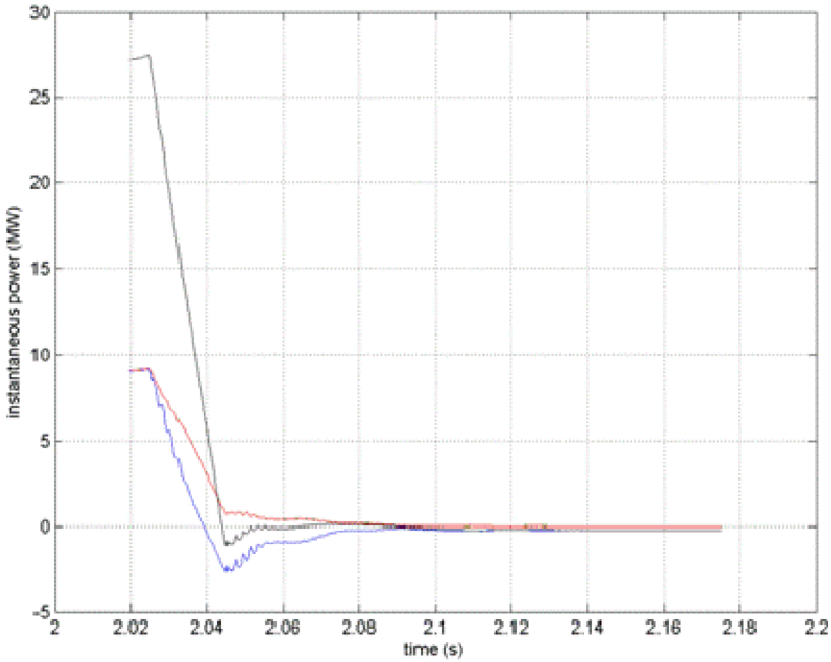

Figure 48: Instantaneous active power at collection point during Fault 3

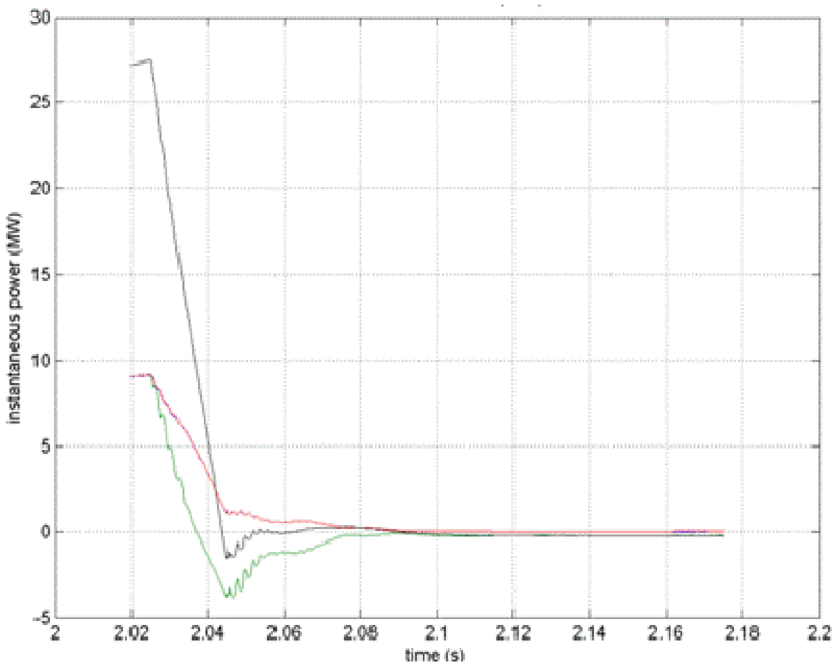

Figure 49: Instantaneous active power at collection point during Fault 4

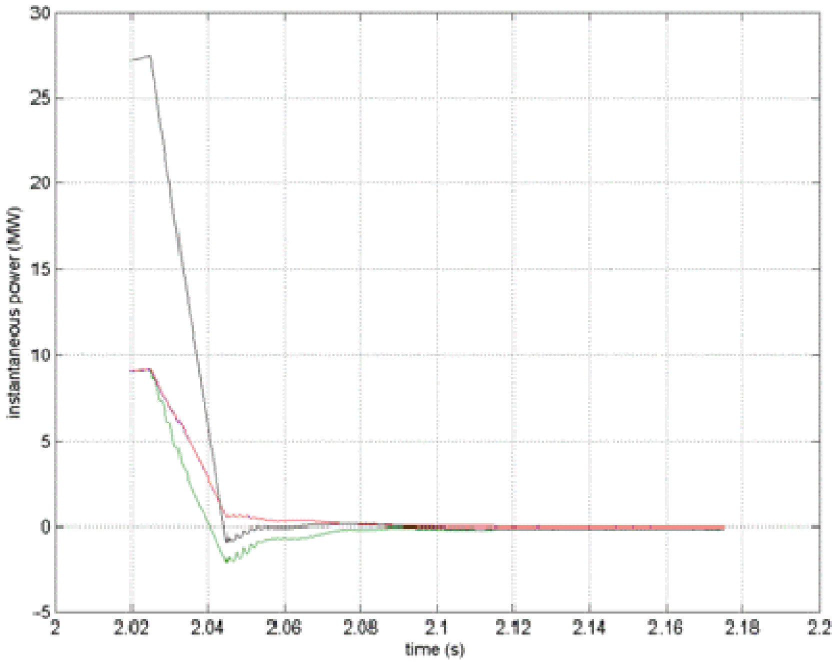

Figure 50: Instantaneous active power at collection point during Fault 5

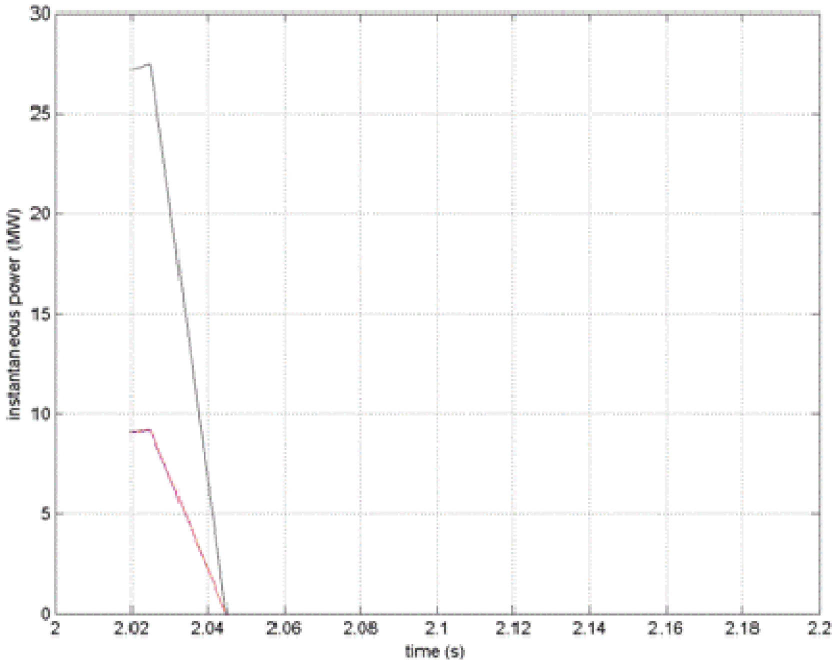

Figure 51: Instantaneous active power at collection point during Fault 6

As can be seen from Figure **46** to Figure **50**, the instantaneous active power flow in the faulty feeder (green or blue) and HVDC connection (black) are changing direction while the healthy feeder (red) is still having the same power flow direction. In Figure **51**, the instantaneous active power becomes zero since the faulty point is in the collection point

Peak currents

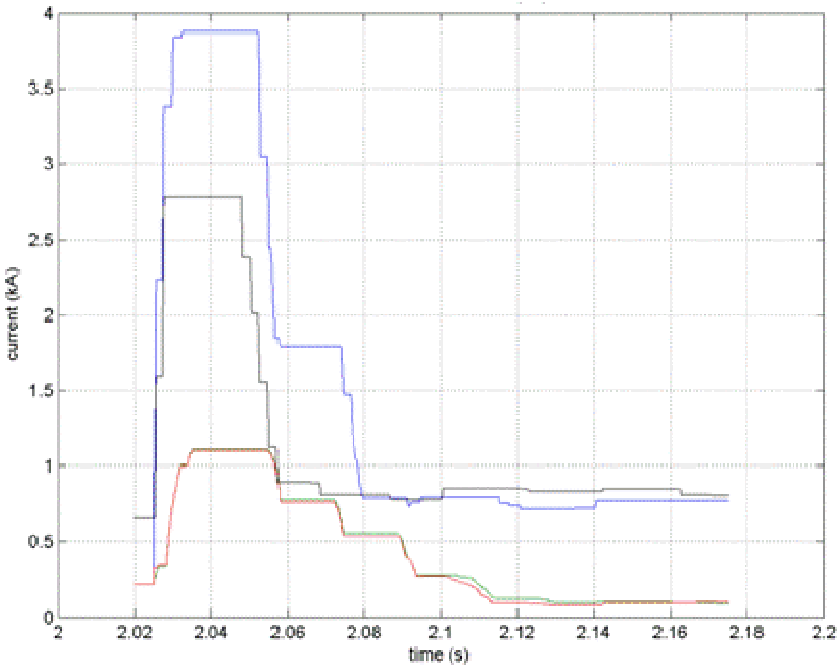

Figure 52: Peak currents at collection point during Fault 1

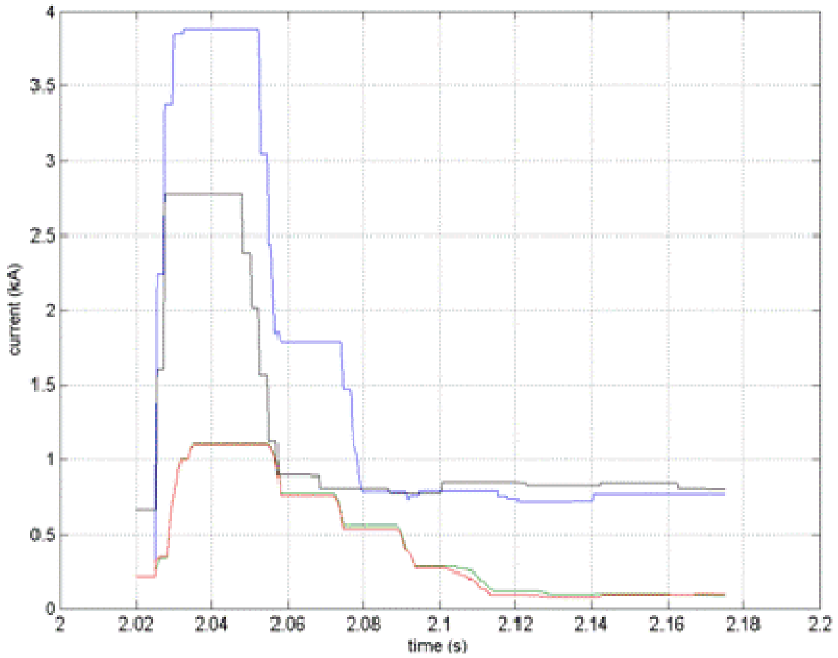

Figure 53: Peak currents at collection point during Fault 2

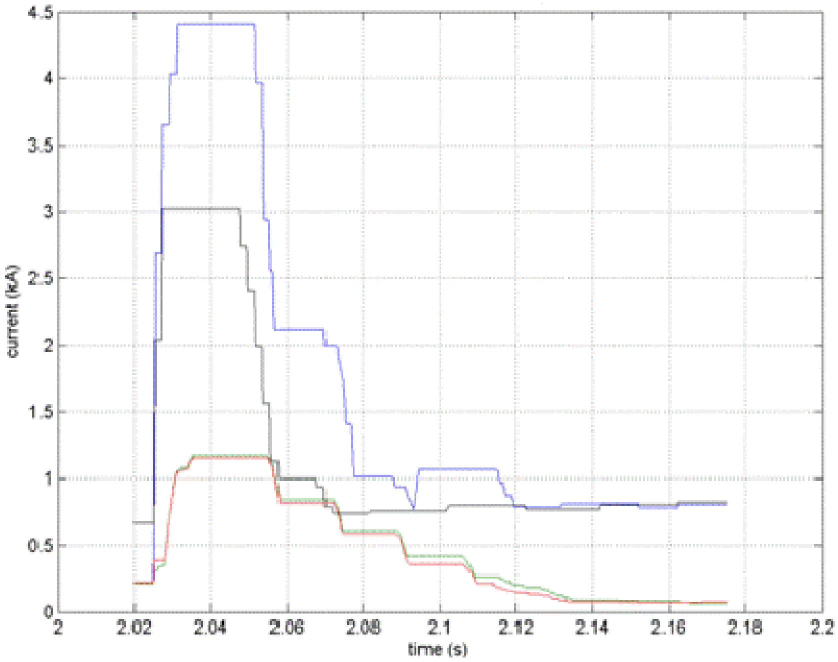

Figure 54: Peak currents at collection point during Fault 3

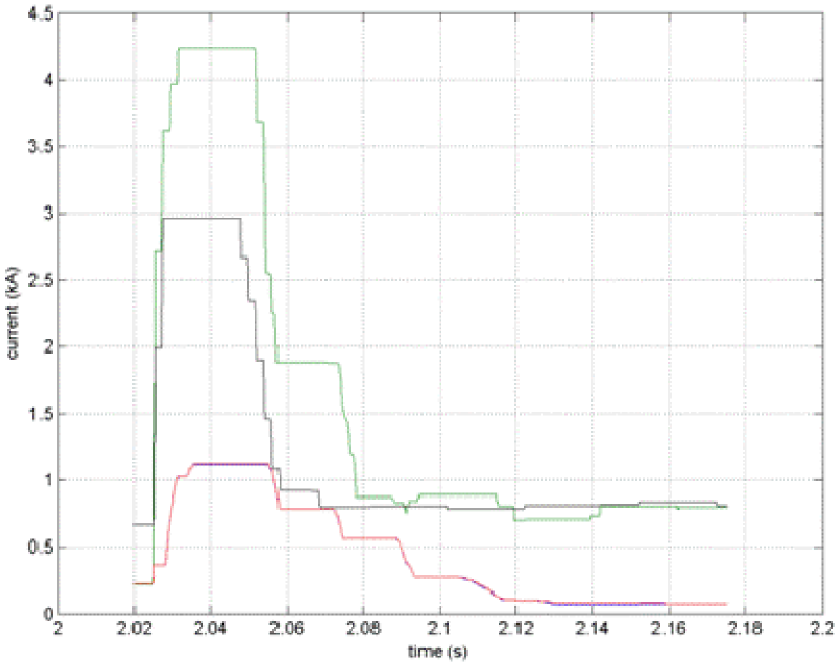

Figure 55: Peak currents at collection point during Fault 4

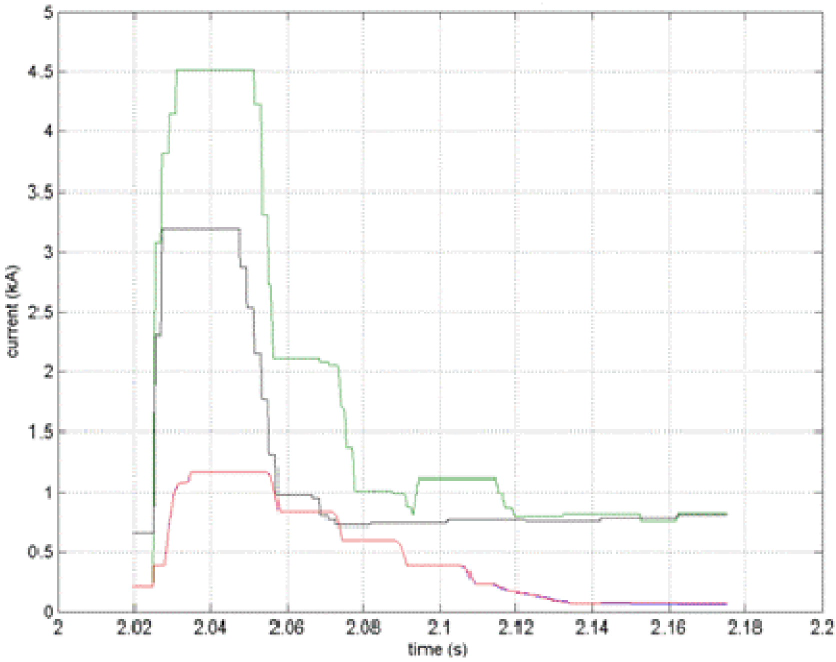

Figure 56: Peak currents at collection point during Fault 5

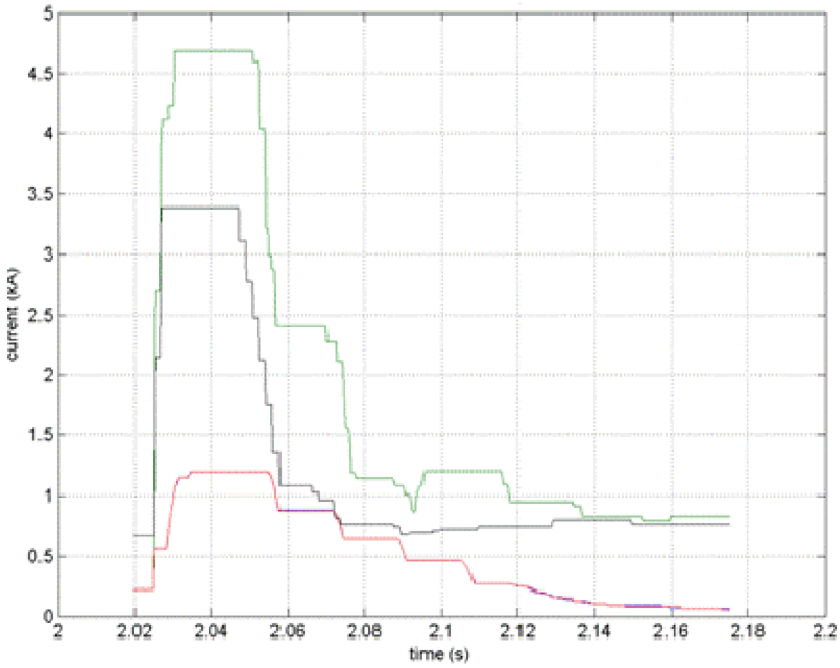

Figure 57: Peak currents at collection point during Fault 6

As can be seen in Figure **52** to Figure **57**, the peak currents are higher in the faulty feeder in comparison to the healthy feeder and HVDC connection.

Possible fault detection is explained as follows, when the directional relay detects a change in the power direction, it enables the relays on each wind farm feeder, which measure the current and detect the faulty feeder. Still, the breaker must not disconnect the line where the fault is because the fault may be distant from the main collector and some wind turbine may still be kept connected. Feeder selectivity has now to be developed.

4.2.2 Feeder line

The analysis continues focusing on the faulty feeder detected at collection point in the previous chapter. The target now is to find a signal (always as output from the sliding window) that allowed finding the exact location of the fault within the feeder.

Three possibilities have been observed: observing peak currents, the directional power or the equivalent positive sequence L-G impedance.

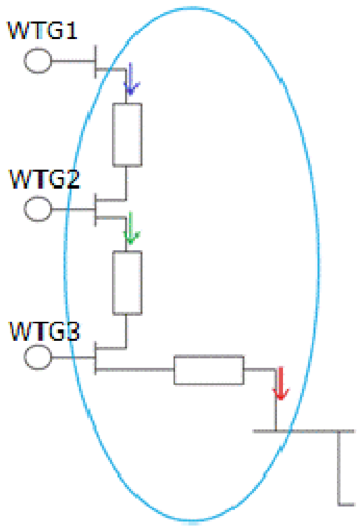

Figure 58: Feeder line with measured quantities (the colors refer to the colors in the following graphs)

Figure 59 to Figure 61, Figure 62 to Figure 64 and Figure 65 to Figure 67 plot the peak currents, the instantaneous active power and the positive sequence L-G impedance in the feeder line respectively. The feeder where the faults have been applied is the left one (Feeder 1), so the faults applied are number 1, 2 and 3. The measurements are taken as shown in Figure 58. The color coding, used also for the other following Figures, is: blue for the cable between WTG 1 and 2, green between WTG 2 and 3, red between WTG 3 and the collection point.

Peak currents

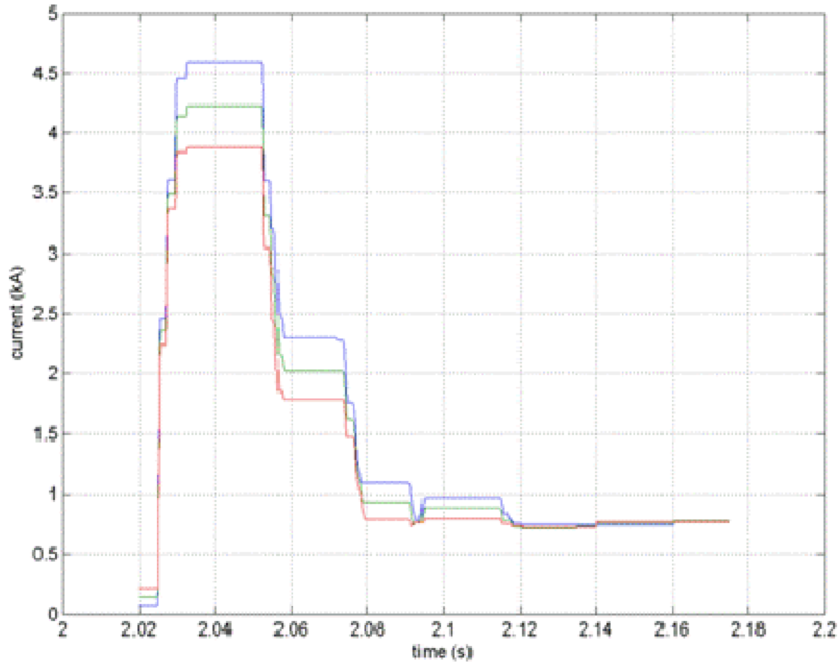

Figure 59: Peak currents at feeder line during Fault 1

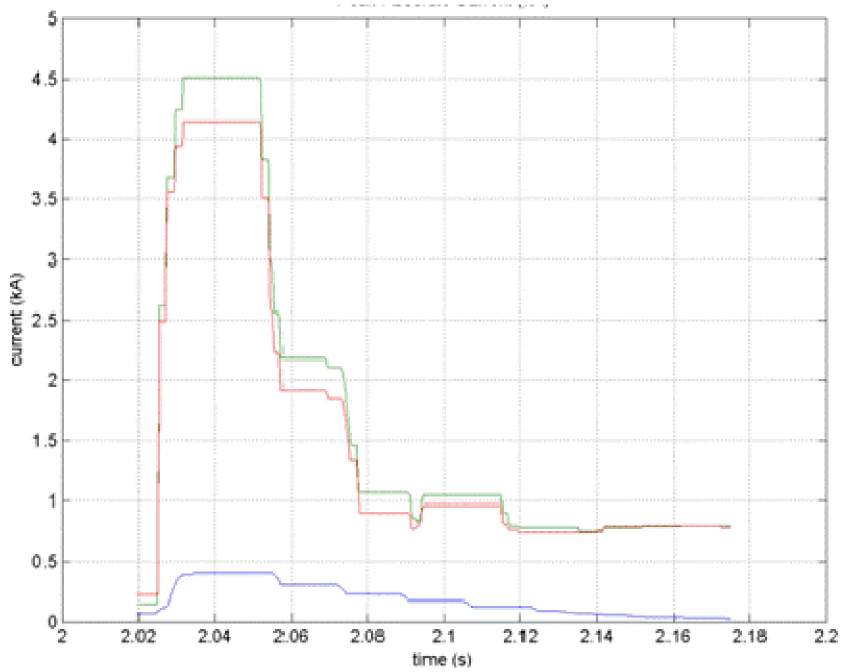

Figure 60: Peak currents at feeder line during Fault 2

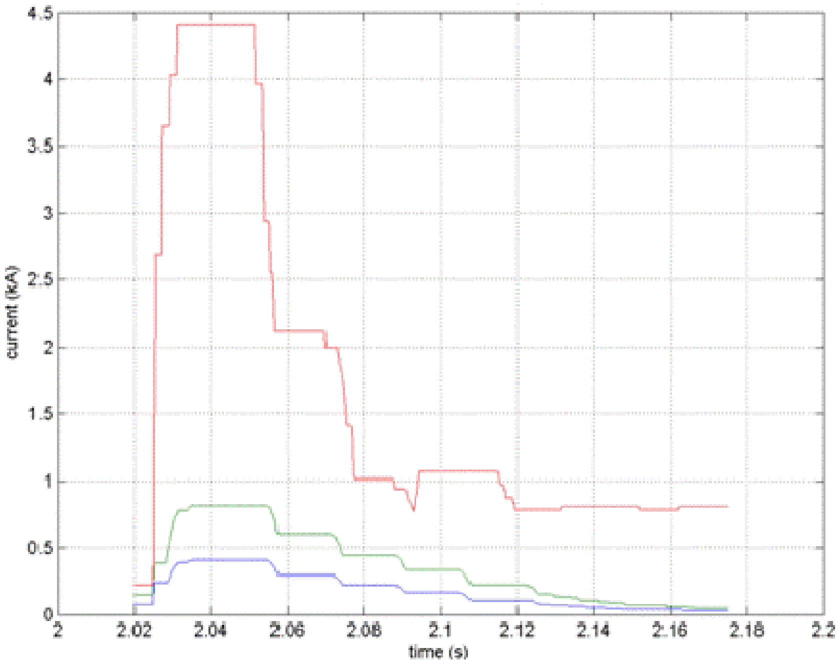

Figure 61: Peak currents at feeder line during Fault 3

As can be seen from Figure **59** to Figure **61**, the peak current different in two measurement units is higher if the fault is occurred between them. This is due to the HVDC current that flow towards the faulty point. While in the healthy section, the peak current difference between the measurement units is less.

Instantaneous active power

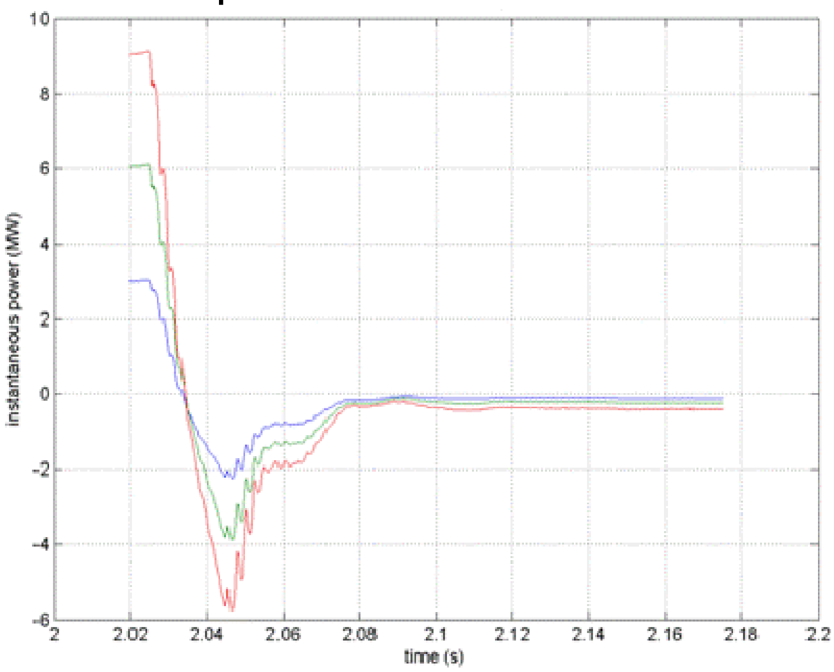

Figure 62: Instantaneous active power at feeder line during Fault 1

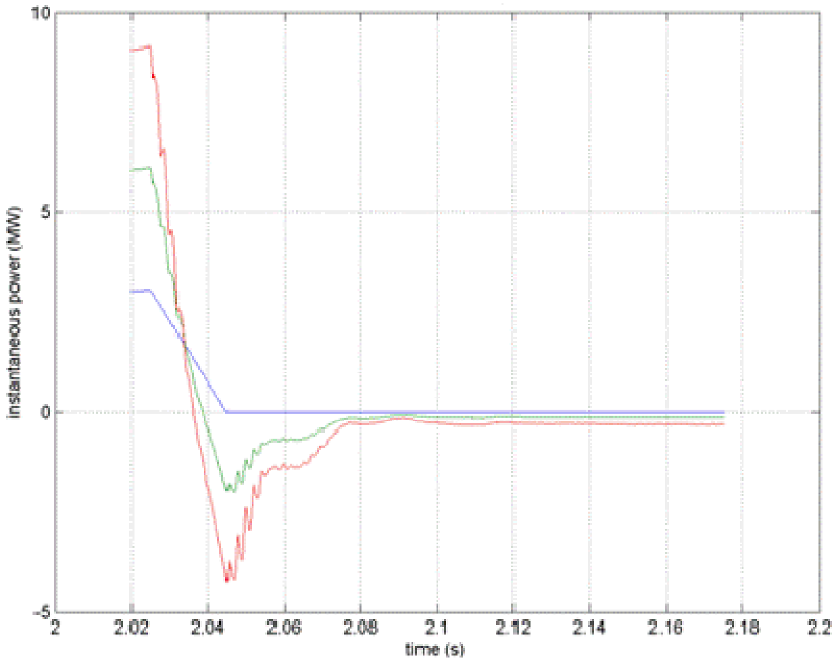

Figure 63: Instantaneous active power at feeder line during Fault 2

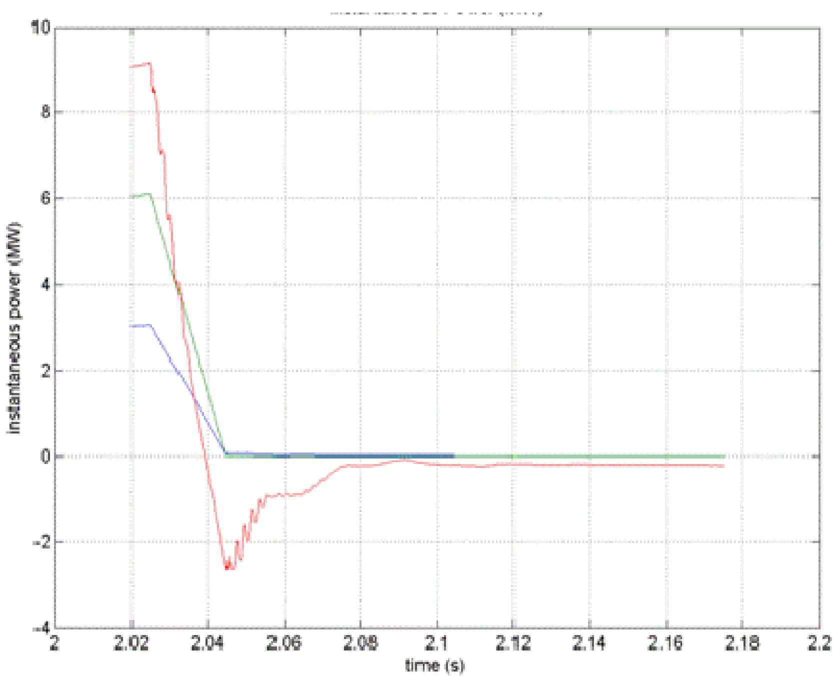

Figure 64: Instantaneous active power at feeder line during Fault 3

As can be seen in Figure **62** to Figure **64**, the instantaneous active power is flowing toward the faulty point, therefore in some part of the line occurred power reversing.

Positive sequence L-G impedance

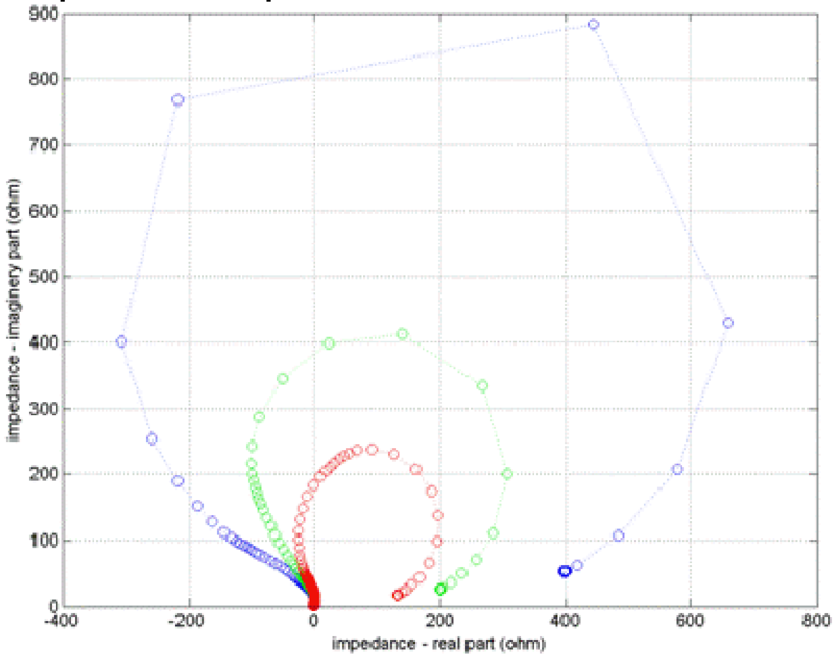

Figure 65: Positive sequence L-G impedance at feeder line during Fault 1

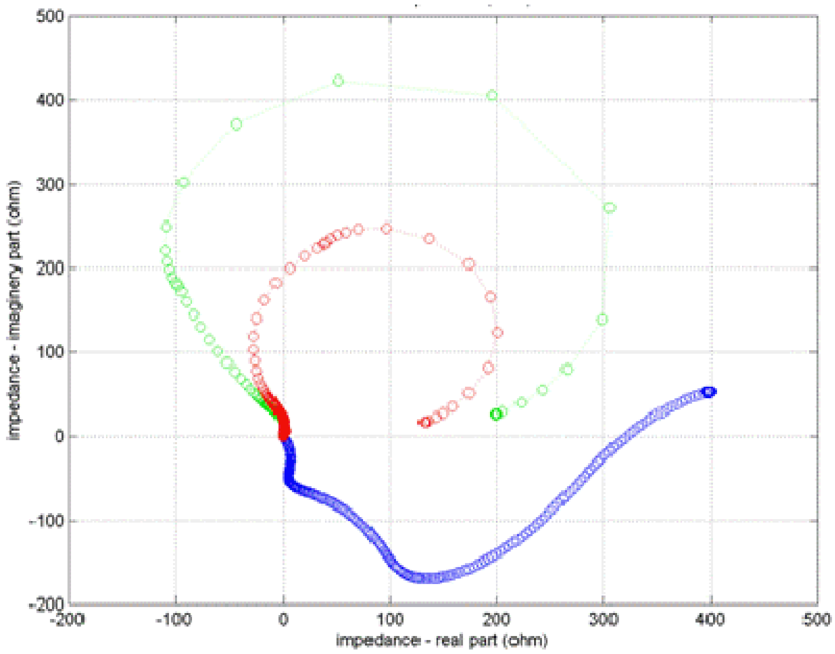

Figure 66: Positive sequence L-G impedance at feeder line during Fault 2

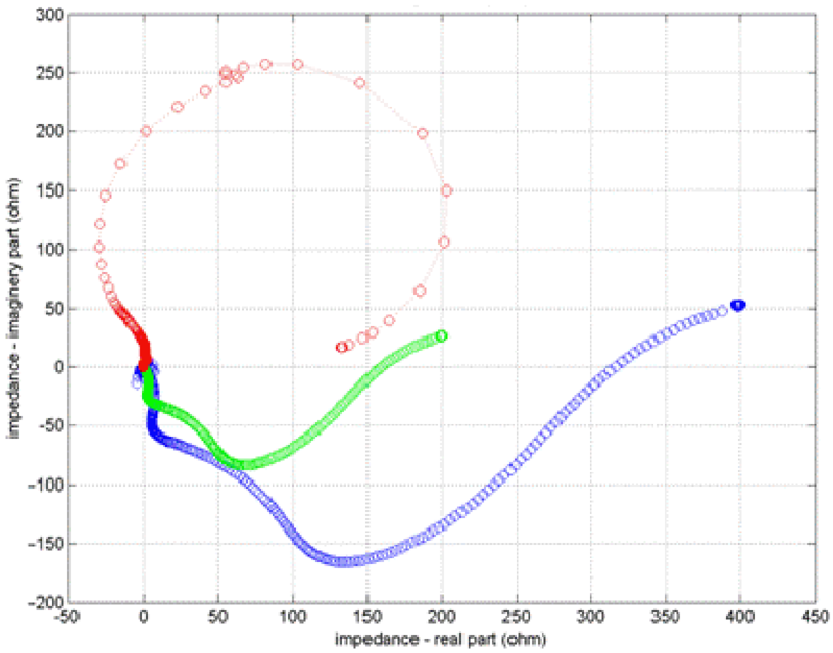

Figure 67: Positive sequence L-G impedance at feeder line during Fault 3

Figure **65** to Figure **67** shown the behavior of the L-G impedance during fault. As can be seen, the trajectory of the impedance change depends on the fault location.

The reason for choosing the peak current to locate the fault on the faulty feeder can be easily found in Figure 33, where peak currents are represented as arrows. The reason for choosing the instantaneous active power and the positive sequence L-G impedance is that a fault within a feeder divides the feeder in two parts with the power ideally flowing towards the fault; since the voltage has been observed to fall almost to zero, a measure of the positive sequence L-G impedance for the use of impedance relays will be used to see if it can prove useful.

4.3 Different simulation scenarios

Different conditions have been applied for the simulation to prove the effectiveness of the detection strategy.

4.3.1 Different sampling frequency

Increasing the rate of data acquisition may lead to a more accurate analysis because the data inside the SW tend to be more accurate. It is a matter of evaluating how much accuracy is reached with a higher sampling frequency. Here the results for the collection point for two faults on different feeders are visualized.

As can be seen in Figure **68**-Figure **70**, there are no significant difference between 4 kHz and 10 kHz sampling frequency DSP results.

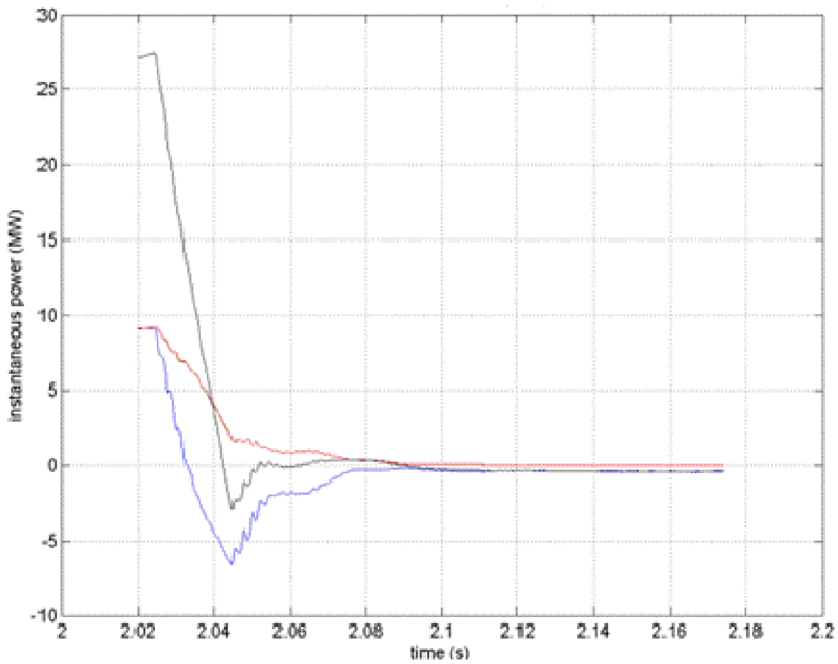

Figure 68: Instantaneous active power at Collection point during Fault 2 for 4 kHz sampling frequency

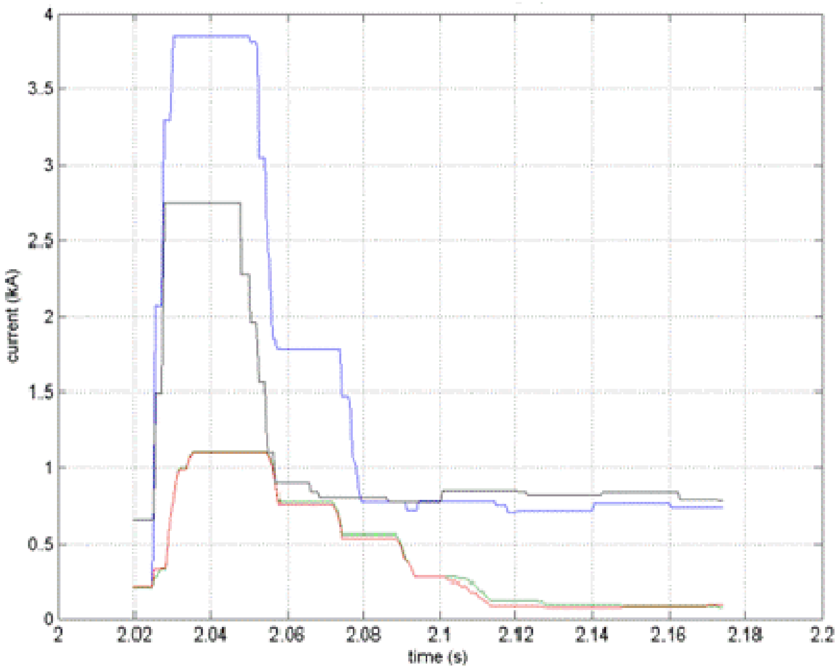

Figure 69: Peak currents at Collection point during Fault 2 for 4 kHz sampling frequency

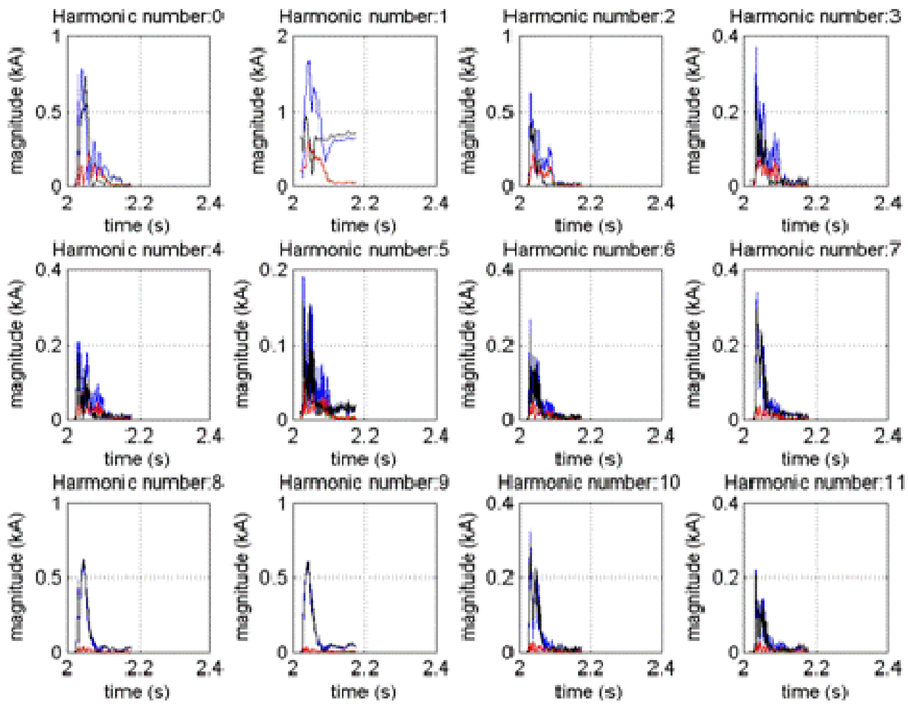

Figure 70: Harmonic analysis at Collection point during Fault 2 with 4 kHz sampling frequency

4.3.2 Different wind turbine condition

It may happen that, during the life cycle of the wind farm, some wind turbine are disconnected for maintenance, but others are still producing power. Here, the case of only four wind turbines operating (as shown in Figure 71) is presented. The results from the application of faults in these conditions are shown are shown from Figure 72 to Figure 77.

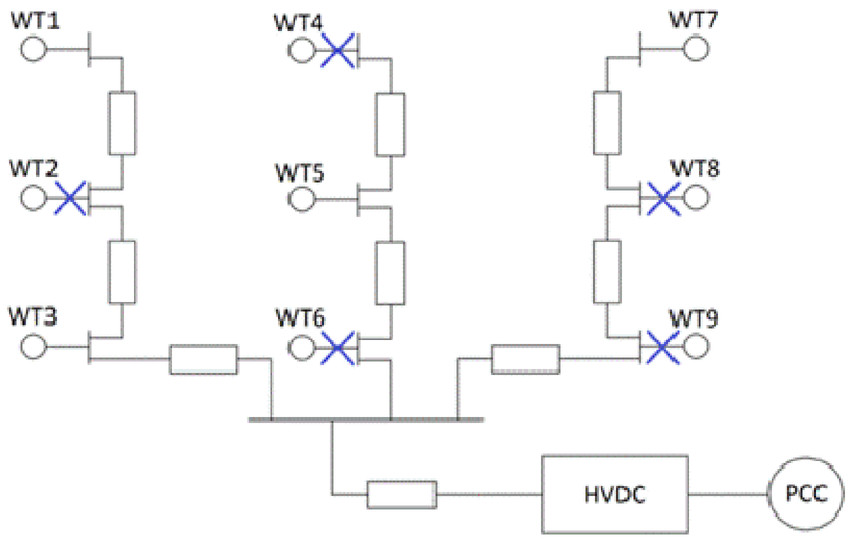

Figure 71: Only four wind turbines are operating in this case

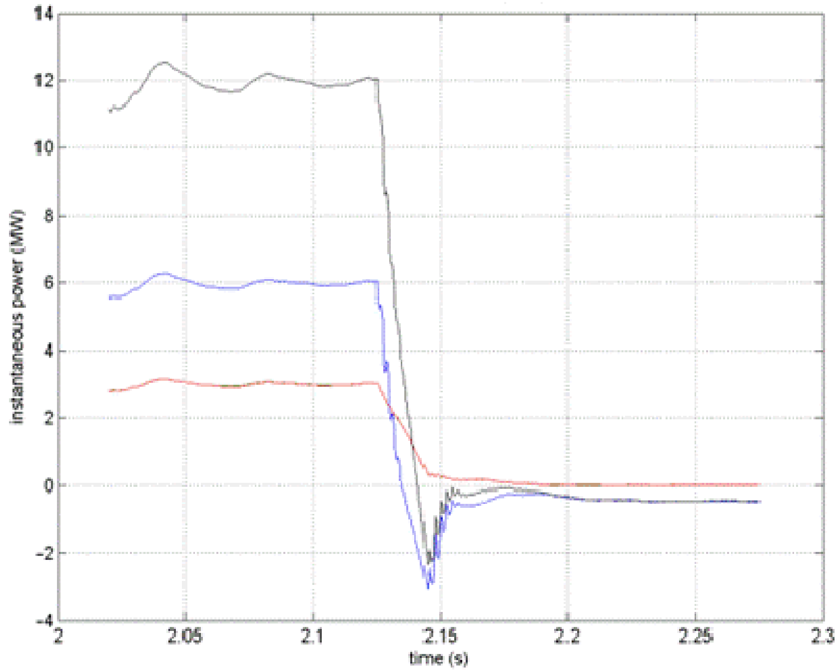

Figure 72: Instantaneous active power at Collection point during Fault 1 with 4 turbines operating

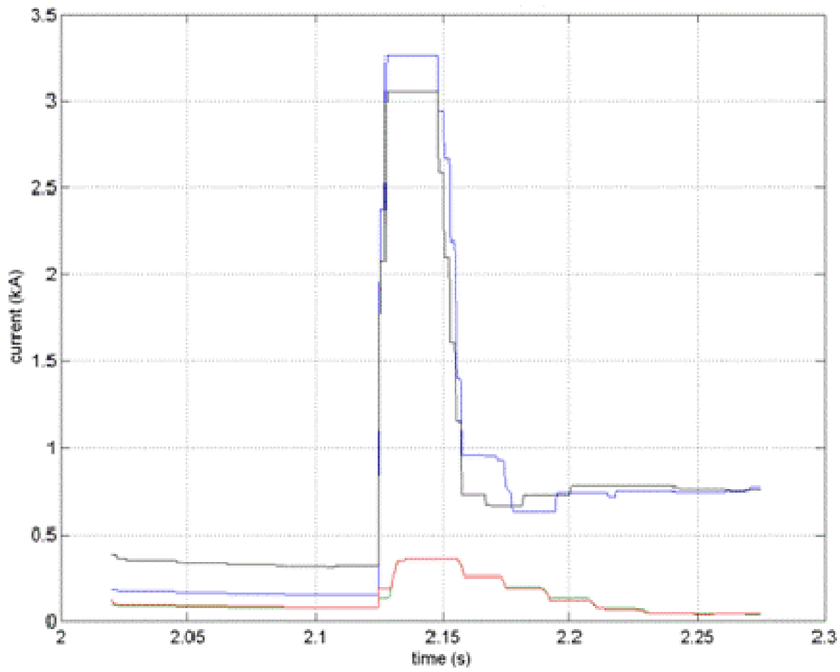

Figure 73: Peak current at Collection point during Fault 1 with 4 turbines operating

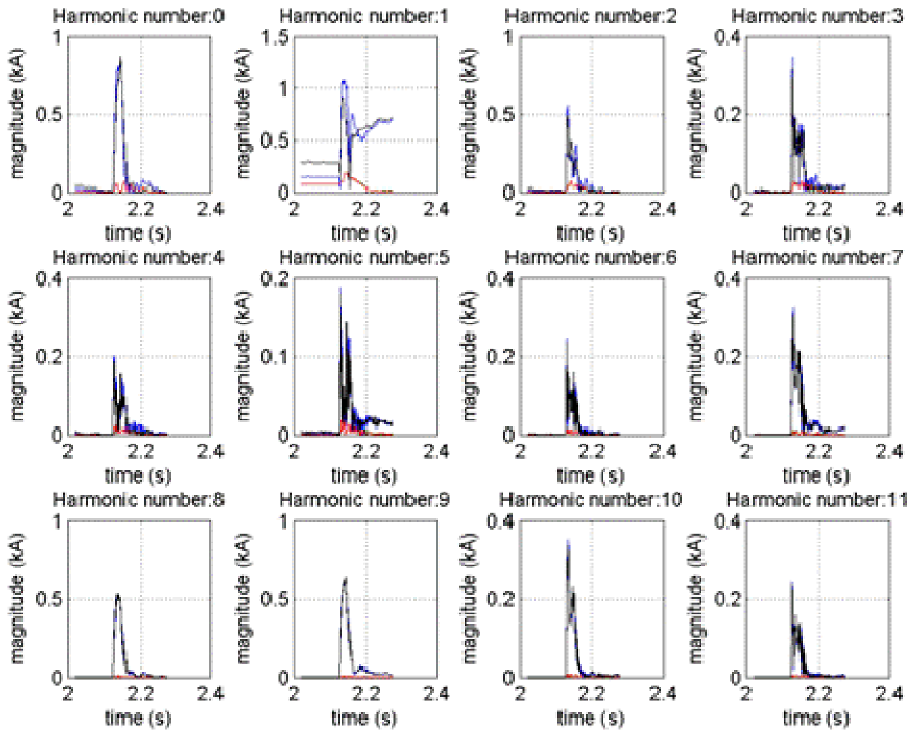

Figure 74: Harmonic currents at Collection point during Fault 1 with 4 turbines operating

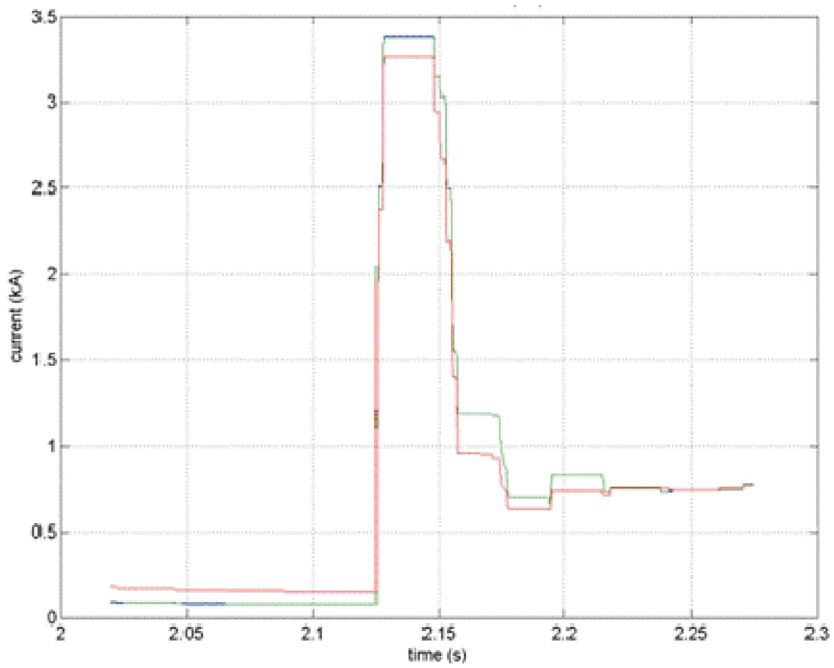

Figure 75: Peak currents at Feeder line during Fault 1 with 4 turbines operating

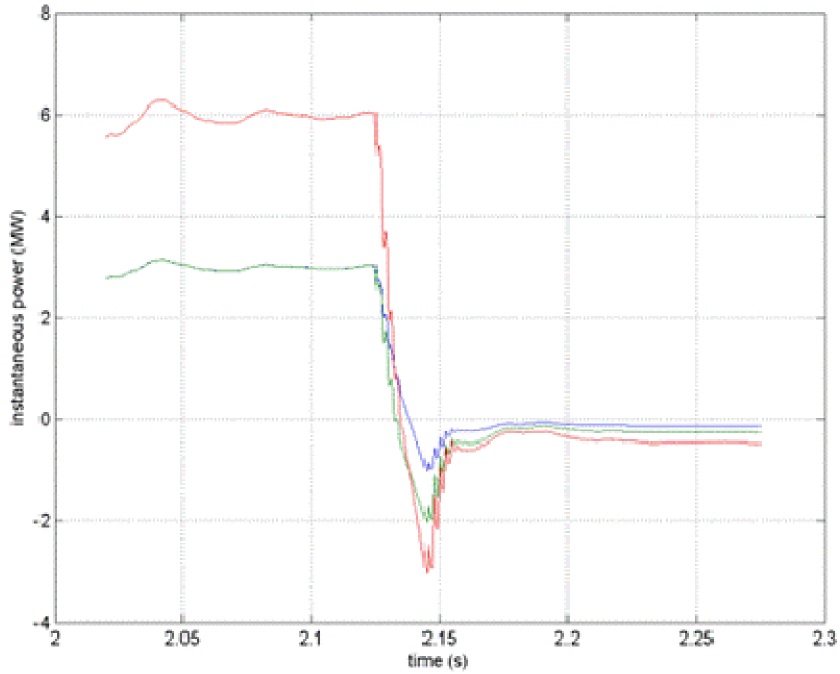

Figure 76: Instantaneous active power at Feeder line during Fault 1 with 4 turbines operating

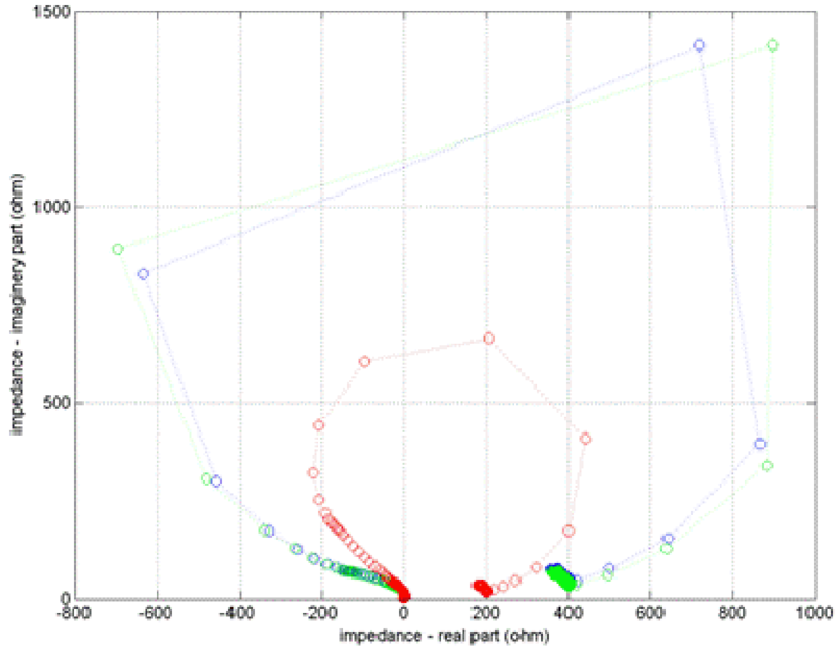

Figure 77: Positive sequence L-G impedance at Feeder line during Fault 1 with 4 turbines operating

4.3.3 Different power ratings of the wind turbines

The following results have been obtained changing the power ratings of the induction generators in the DFIGs and consequently the power rating of the HVDC.

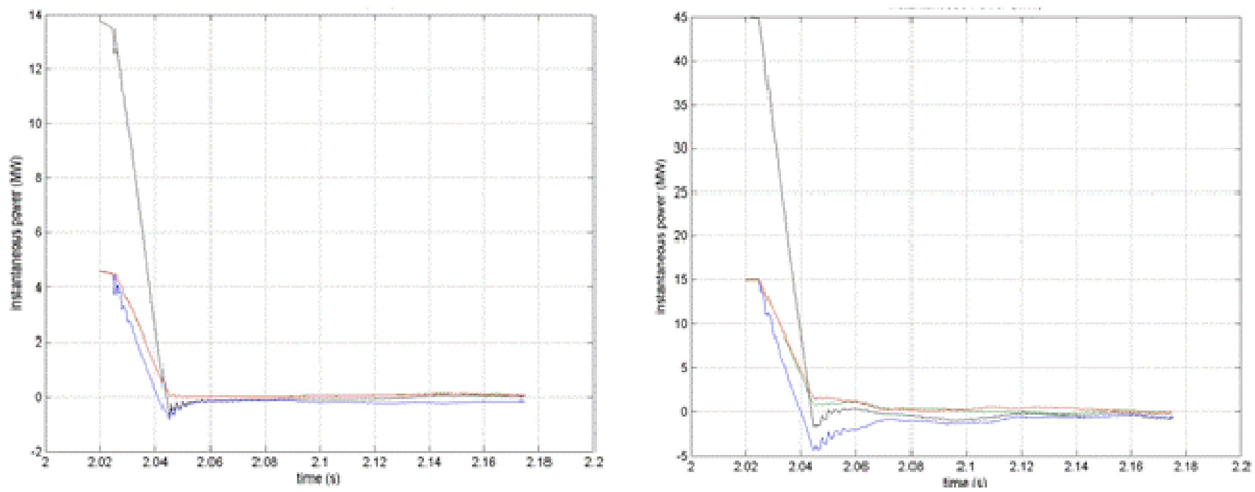

Figure 78: Instantaneous active power at Collection point during Fault 2, the turbines power ratings are 1.5 MW (left) and 5.0 MW (right)

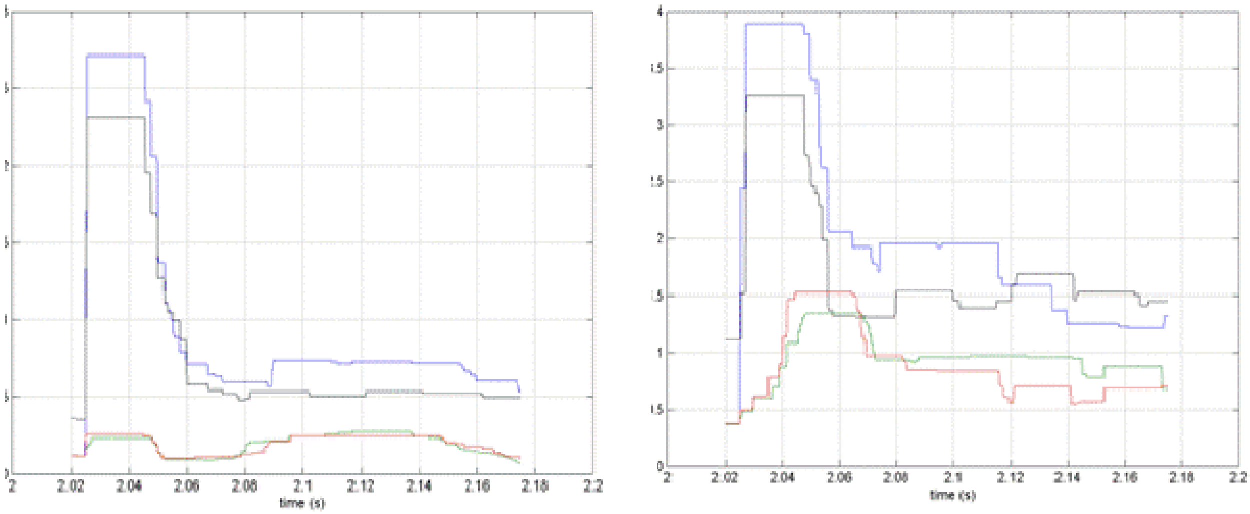

Figure 79: Peak current at Collection point during Fault 2, the turbines power ratings are 1.5 MW (left) and 5.0 MW (right)

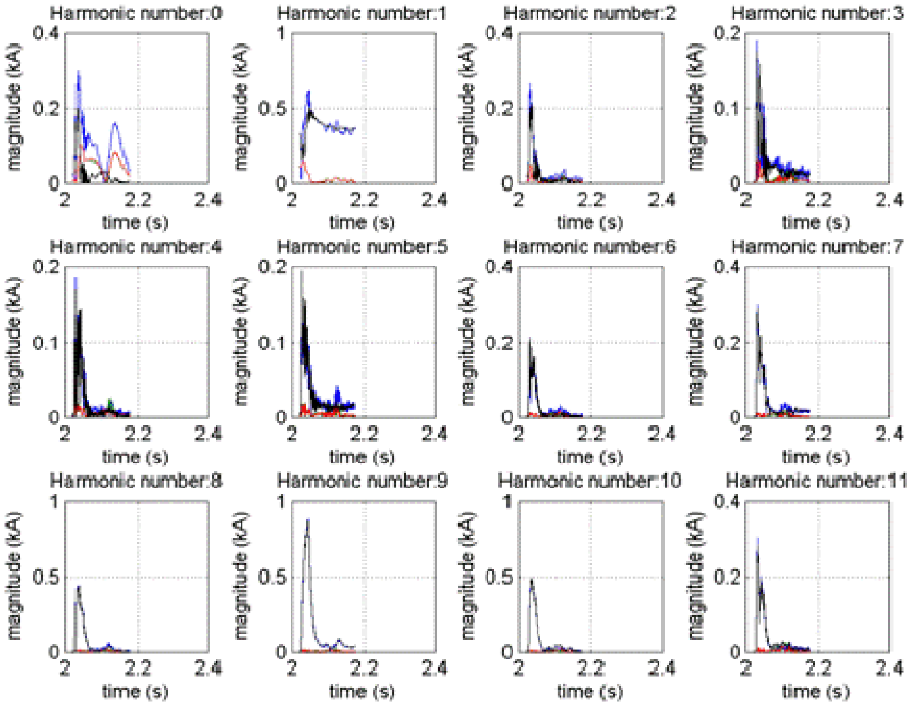

Figure 80: Harmonic currents at Collection point for Fault 2 (1.5 MW rating)

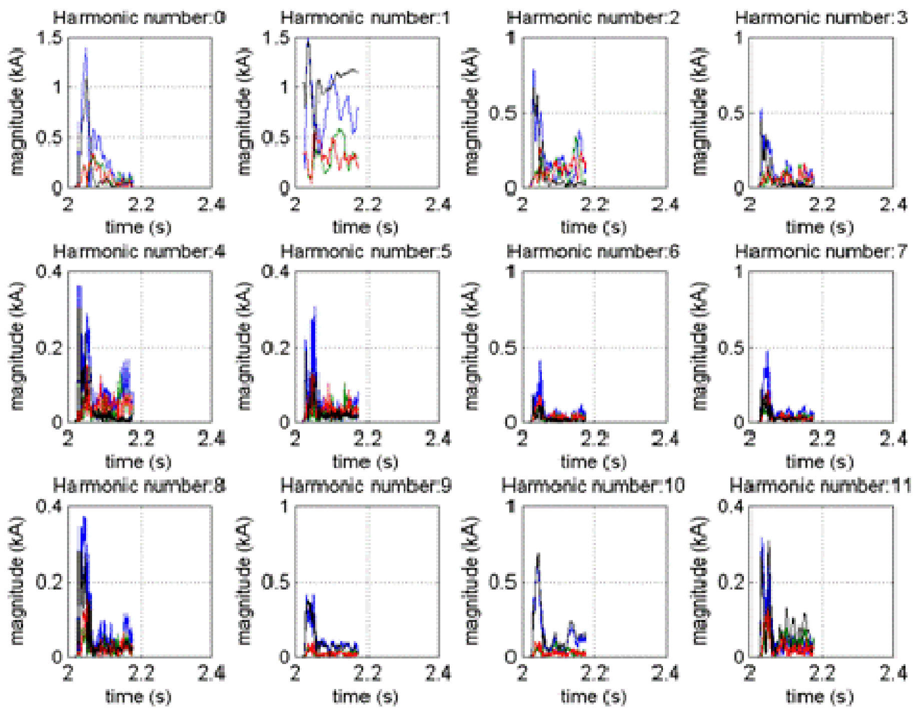

Figure 81: Harmonic currents at Collection point for Fault 2 (5.0 MW rating)

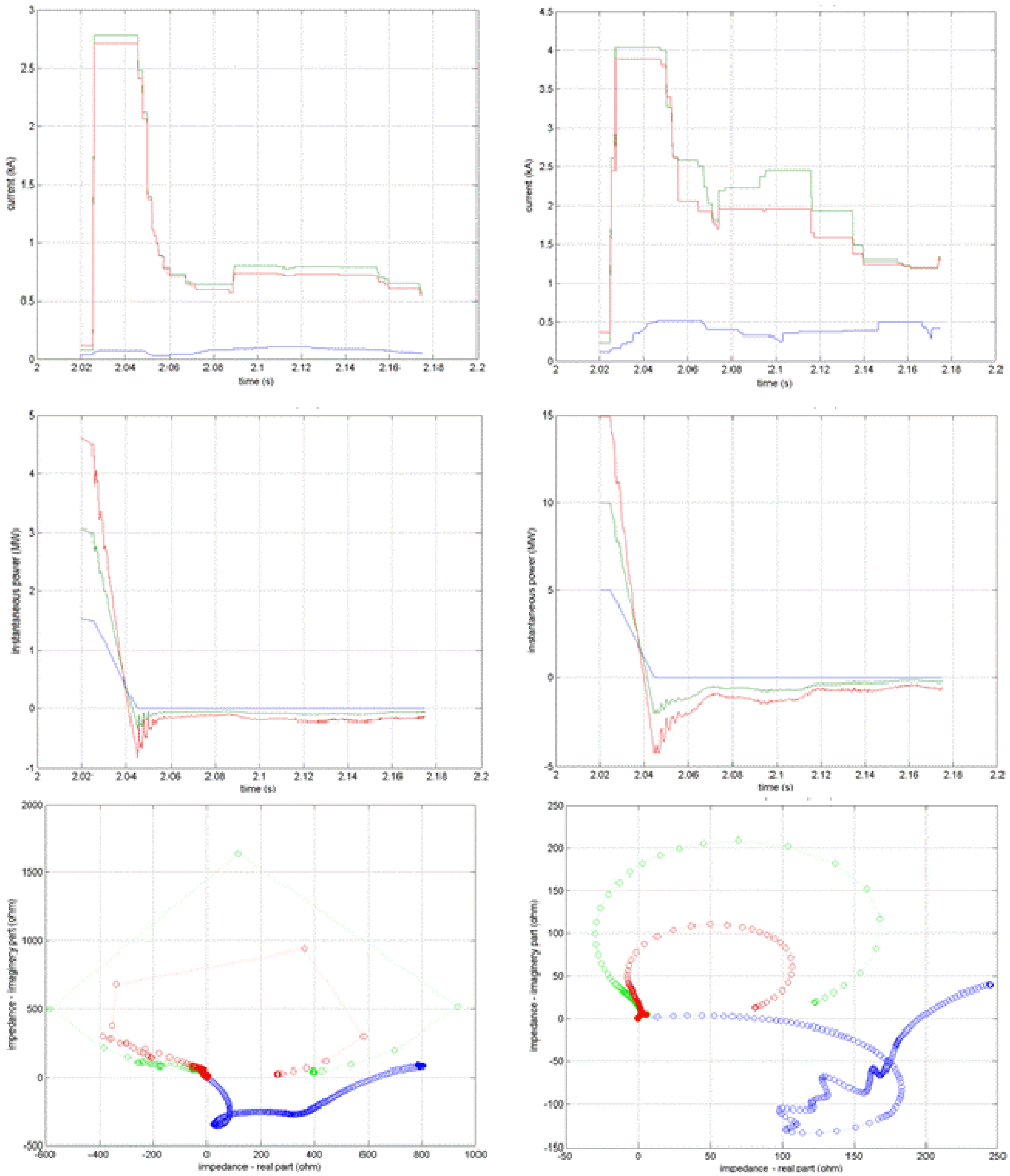

Figure 82: Peak currents, instantaneous active power and fault impedance a at Feeder line during Fault 2, the turbines power ratings are 1.5 MW (left) and 5.0 MW (right)

4.4 Fault detection method validation

As can be seen in the previous sub section, over-current and current differential relay can still satisfy the requirement for detecting the fault in collection point and feeder line, respectively. Therefore, only these two relays are modeled in order to validate the proposed fault detection methods.

4.4.1 Relay model and setting

The settings of the relay models are based on the base test case where all wind turbines rating are 3 MW and by considering the different simulation conditions as explained in the previous sub section.

4.4.1.1 Over-current relay

The over-current relay model in PSCAD/EMTDC is depicted in Figure 83. This relay continuously checks whether or not the input signal exceeds the specified threshold current.

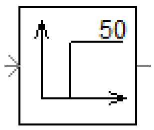

Figure 83: Over-current relay model

The threshold current is set to 1.5 kA or 7 time normal feeder current.

4.4.1.2 Current differential relay

The current differential relay compares the current (magnitude and phase) from two measurement units. This relay is used in the feeder line to detect the faulty section within the line. Having the result in the previous section, it is known that this relay is only used for comparing the current magnitude of two measurement units. Therefore 'M' inputs in the PSCAD/EMTDC current differential relay model (as depicted in Figure 84) are the current magnitudes while the 'P' inputs are constant zero and 180 (or 2π).

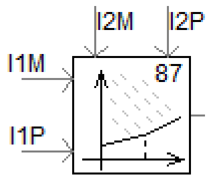

Figure 84: Current differential relay model

The differential threshold current is set to 0.62 kA or 10 times larger than the rated current difference between two measurement units along feeder line.

4.4.2 Validation results

4.4.2.1 Collection point

The following figures only shows the trip signal in collection point when the faults are located in location 2 and location 5. The same trip signal is found to be same for the other fault location within feeder 1 and 2. The fault is occurred at 0.525 second.

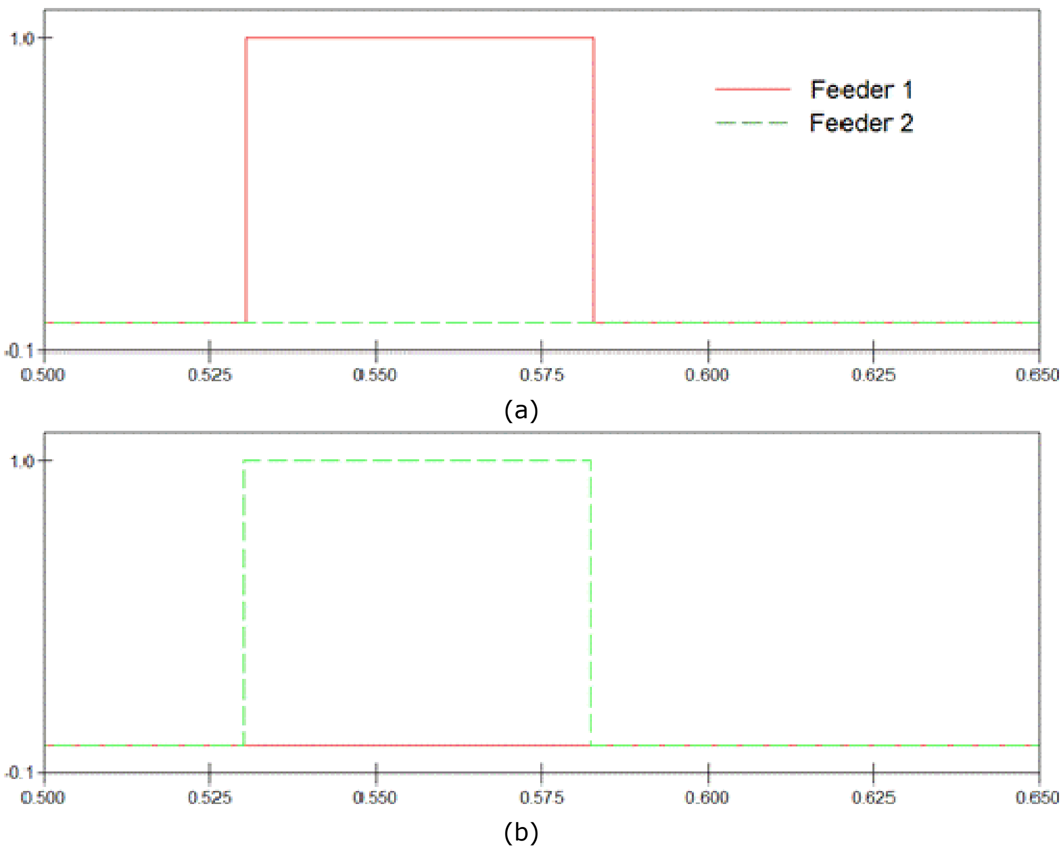

Figure 85: Fault is detected in: (a) feeder 1 during Fault 2, (b) feeder 2 during Fault 5

Figure 85 shows the behavior of the fault detection method placed in the collection point when fault is occurred in location 2 and 5. As can be seen in Figure 85, the trip signal only last for 2 cycles, because the short-circuit fault current in steady state is lower than the current threshold. The fault detection time is approximately 5 ms after the fault instance.

4.4.2.2 Feeder line

The following figures only show the fault detection validation in feeder 1. The same trip signal is found to be same for the other fault location.

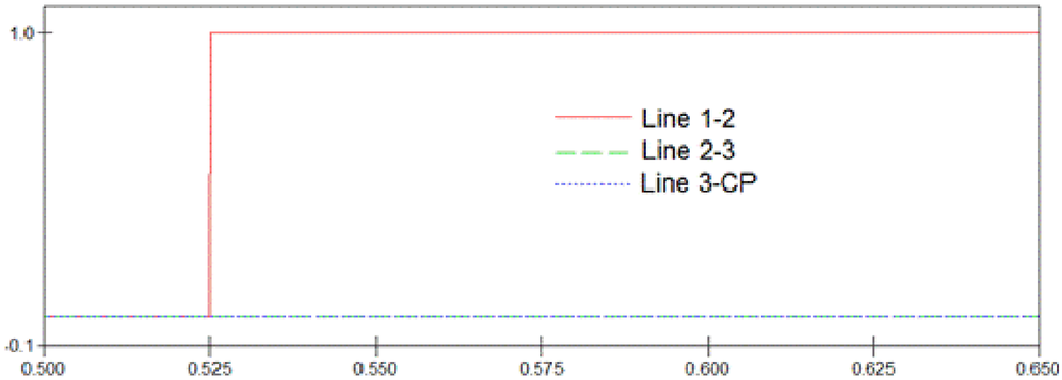

(a)

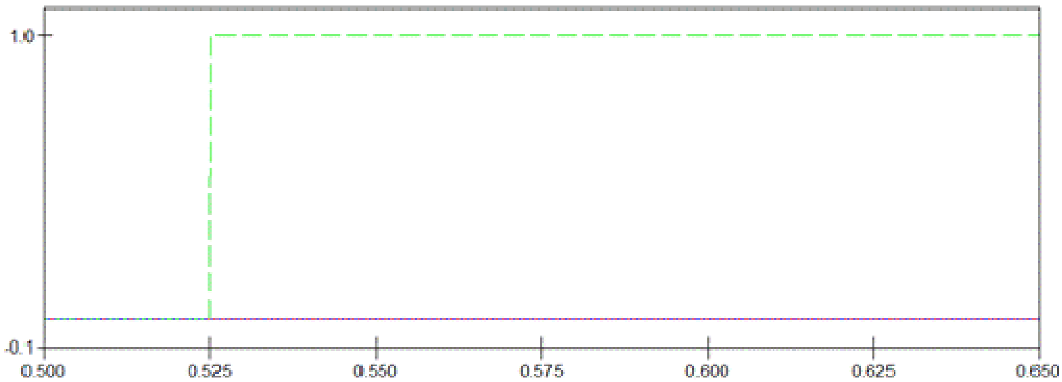

(b)

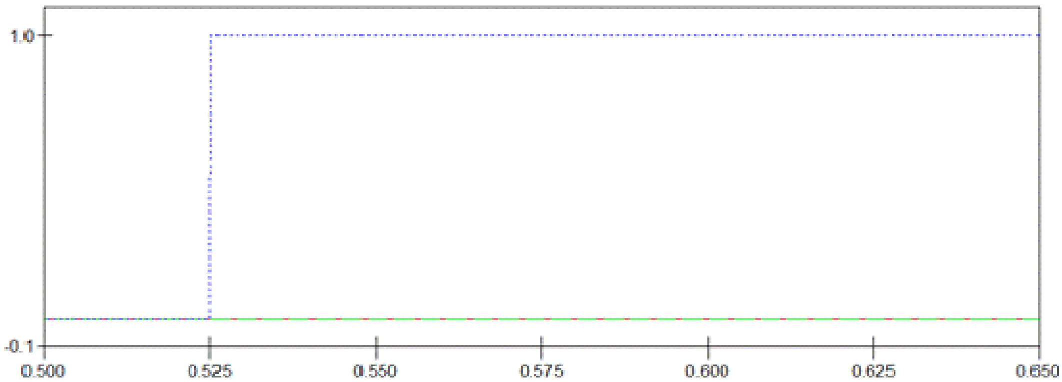

(c)

Figure 86: Fault is detected in: (a) line 1-2 during Fault 1, (b) line 2-3 during Fault 2, (c) line 3-CP during Fault 3

Figure 86 shows the feeder line fault detection output for fault occurred in location 1, 2, and 3, respectively. As can be seen the proposed method can detect the faulty section within feeder line correctly. The response of the fault detection method is faster as compared to Figure 85.

4.5 Conclusion

The studies were performed using a model of DFIG that does not include the overspeed protection of rotor. This model is good enough to capture the short-circuit behavior for a period of interest (approximately 250 ms) for the instance of fault.

Since the crowbar is activated during the fault within the wind farm collection grid, the DFIG is having similar behavior as a wound rotor induction generator. Short-circuit current contribution from a single DFIG reach 6-10 times higher than its rated current [0]. The feeder current measured in the collection grid during the fault also reach more than 15 times normal feeder current.

Although these high peak current last only for 3 cycles, this significant change can be used to detect the fault. The faulty feeder can be detected by observing the peak current at the collection point (Figure 28). Over-current relay can be utilized to accomplish this method. The over-current relay has taken 5 milliseconds for detection of the fault.

The faulty section within a feeder line can be detected by comparing the current magnitude from two ends of the section. This method can be accomplished by utilizing the current differential relay. This requires communication link between the two ends of a section. The proposed method can detect the faulty section instantaneously.

5 Simulation results with FCG

5.1 Short-circuit simulation results and analysis

Unlike AC machines, during fault, converter used in FCG and HVDC can be represented as current source [0]. As depicted in Figure 87, the left-side of busbar i represents the FCG/HVDC, while the right-side of busbar i represents the synchronous generator (SG) under fault condition. When three-phase fault occurs in busbar i, short-circuit current contribution from SG depends on the equivalent impedance of the generator and the line between the generator and the busbar, while the short-circuit current contribution from FCG/HVDC is known and limited to 10% above nominal current. Under unbalance short-circuit faults, e.g. single phase to ground fault or line to line fault, the converter control is designed to continue to supply balanced three-phase currents irrespective of the degree of its voltage unbalance. In both balance and unbalance fault, the current control strategy is normally very fast so that short-circuit current contribution from FCG/HVDC does not change with time.

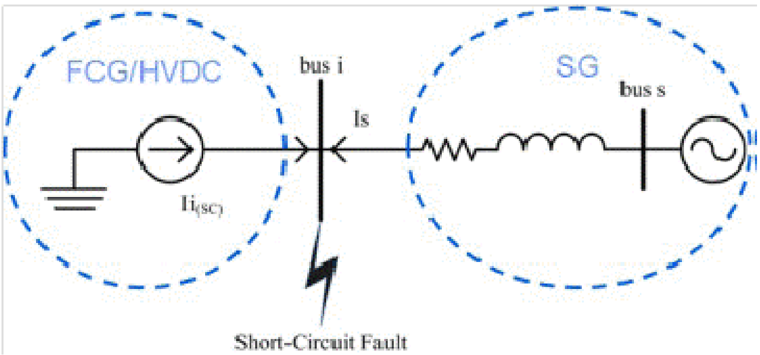

Figure 87: Equivalent circuit of FCG/HVDC and synchronous generator (SG) during short-circuit fault

5.1.1 Collection point

If the fault occurs in feeder 1, currents are flowing from feeder 2, feeder 3, and HVDC into feeder 1, as can be seen in Figure 88.

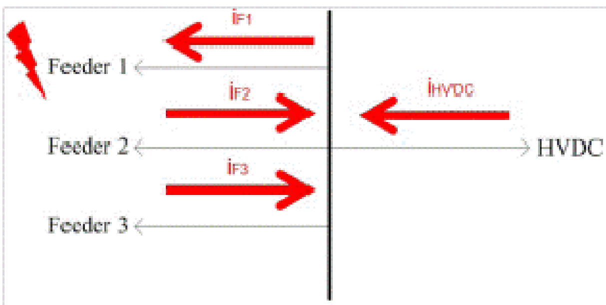

Figure 88: Current behavior when fault occurs in feeder 1

The amount of the current flowing into feeder 1 can be calculated as follows:

$$\begin{aligned} i_{HVDC} &= 1.1 \text{ p.u.} \\ i_{F2} &= \frac{1}{3} \times 1.1 \text{ p.u.} \\ i_{F3} &= \frac{1}{3} \times 1.1 \text{ p.u.} \\ i_{F1} &= 1.8333 \text{ p.u.} \end{aligned} \qquad (0)$$

where i_{F1}, i_{F2}, i_{F3}, and i_{HVDC} are the current measured in feeder 1, feeder 2, feeder 3, and HVDC feeder respectively.

Current measured in feeder 1 (Figure 89(a)) is increased from 0.33 p.u. during normal condition (all FCGs are producing power at their rating) to 1.83 p.u. during fault.

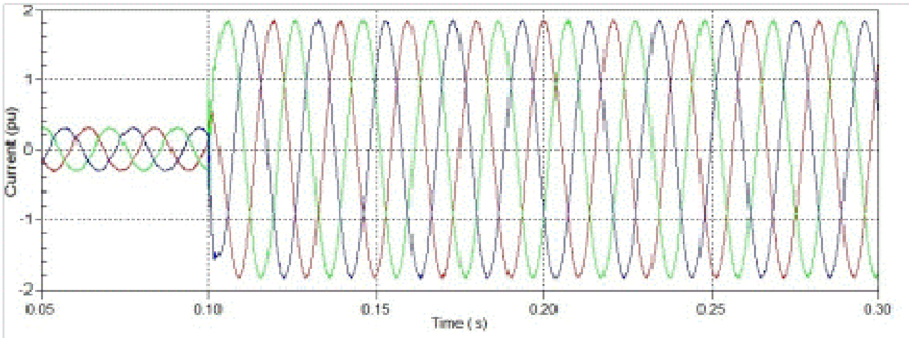

Current (pu)
Time (s)

(a)

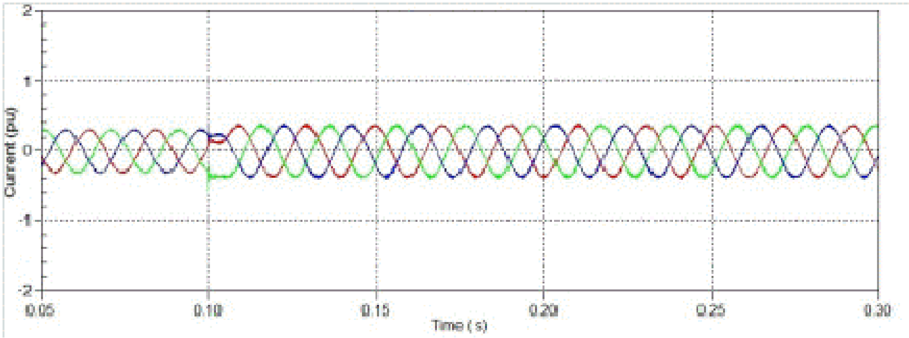

Current (pu)
Time (s)

(b)

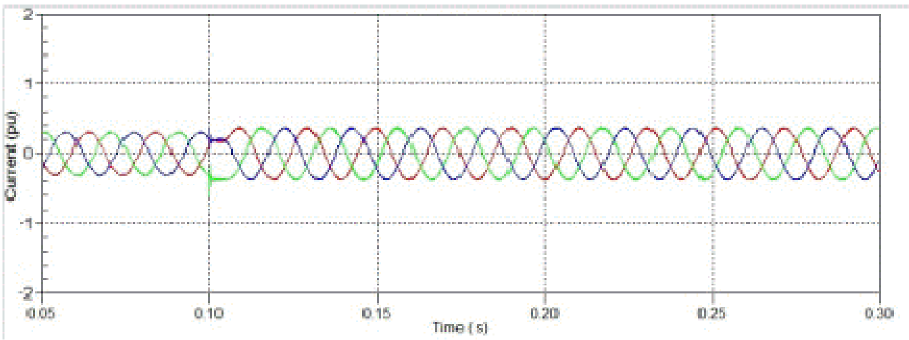

Current (pu)
Time (s)

(c)

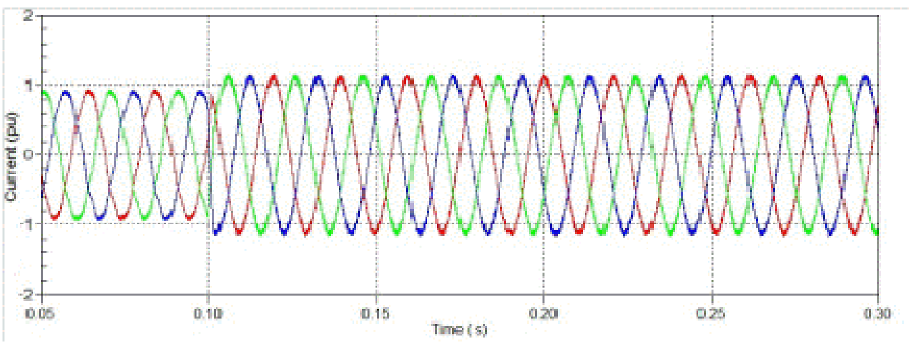

Current (pu)
Time (s)

(d)

Figure 89: Current flowing in: (a) feeder 1; (b) feeder 2; (c) feeder 3; and (d) HVDC feeder

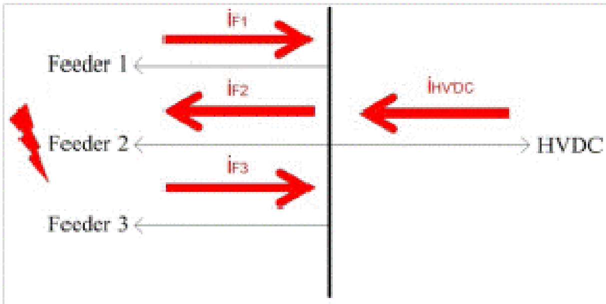

Figure 90: Current behavior when fault occurs in feeder 2

If the fault occurs in feeder 2 (depicted in Figure 90), the current flows into feeder 2 can be calculated as follows:

$$\begin{aligned} i_{HVDC} &= 1.1 \text{ p.u.} \\ i_{F1} &= \frac{1}{3} \times 1.1 \text{ p.u.} \\ i_{F3} &= \frac{1}{3} \times 1.1 \text{ p.u.} \\ i_{F2} &= 1.8333 \text{ p.u.} \end{aligned} \quad (0)$$

Current measured in feeder 2 (Figure 91(b)) is increased from 0.33 p.u. during normal condition to 1.83 p.u. during fault.

As can be seen in Figure 89 and Figure 91, current flows into the faulty feeder equals 1.83 p.u. which is the sum of short-circuit current contribution from healthy feeders and HVDC. Discontinuity in the current waveform of the healthy feeders occur due to the FCG status change from full active power support to full reactive power support.

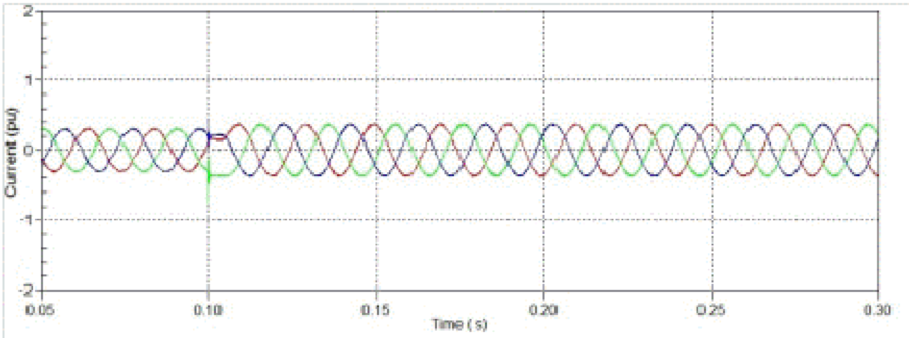
2
1
0
-1
-2
Current (pu)
0.05
0.10
0.15
0.20
0.25
0.30
Time (s)

(a)

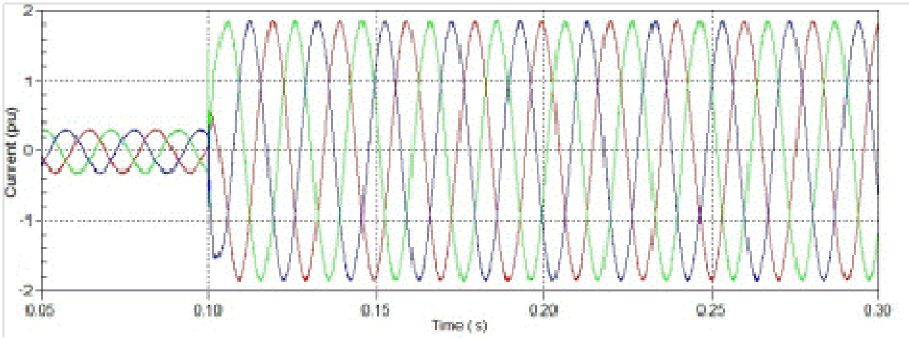
2
1
0
-1
-2
Current (pu)
0.05
0.10
0.15
0.20
0.25
0.30
Time (s)

(b)

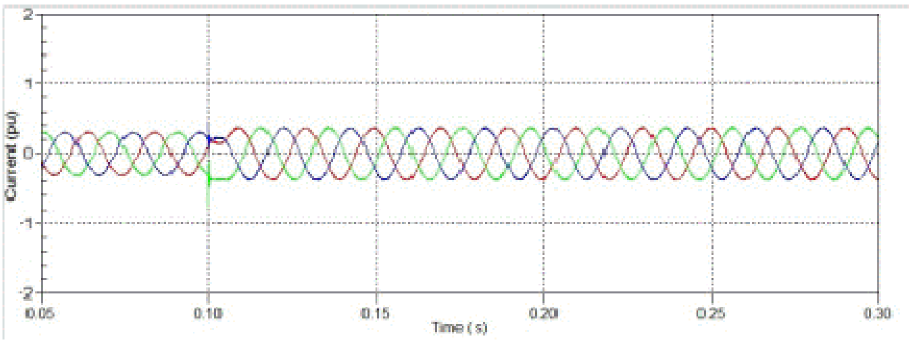
2
1
0
-1
-2
Current (pu)
0.05
0.10
0.15
0.20
0.25
0.30
Time (s)

(c)

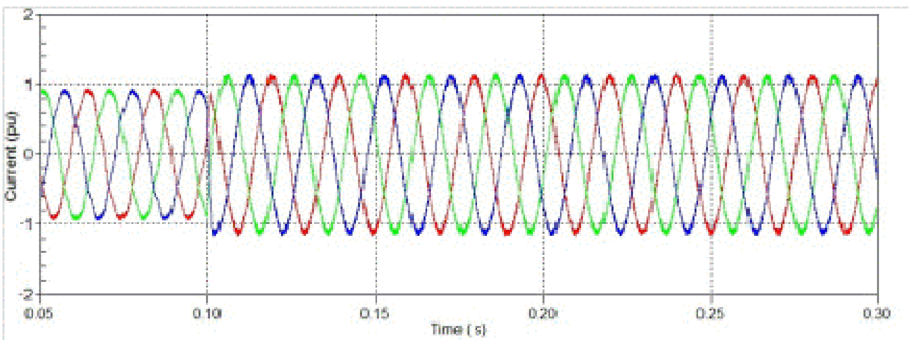
2
1
0
-1
-2
Current (pu)
0.05
0.10
0.15
0.20
0.25
0.30
Time (s)

(d)

Figure 91: Current flowing in: (a) feeder 1; (b) feeder 2; (c) feeder 3; and (d) HVDC feeder

5.1.2 Feeder line

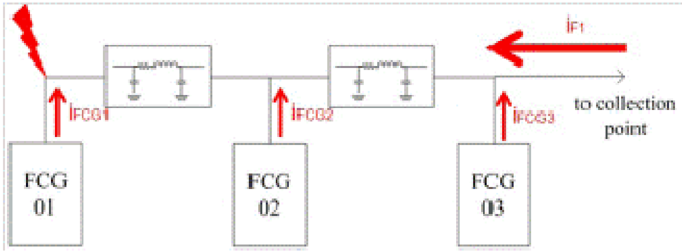

Figure 92: Current behavior when fault is in location 1

If fault is located in location 1 (as depicted in Figure 92), short-circuit current contribution from each FCGs are 10% above their nominal current, therefore fault current (i_{Fault}) can be calculated as follows:

$$\begin{aligned} i_{F1} &= 1.8333 \ \text{p.u.} \\ i_{FCG} &= \frac{1}{9} \times 1.1 \ \text{p.u.} \\ i_{Fault} &= 2.2 \ \text{p.u.} \end{aligned} \qquad (0)$$

where i_{FCG} is the short-circuit current contribution from FCG.

The fault current when fault occurred in location 1 as well as location 2 and 3 is shown in Figure 93.

Since the converter can be represented as current source, the amounts of short circuit current contribution from FCGs are not depending on the line impedance. Therefore, the calculated fault current in (0) is also valid for the other fault locations. This can be seen in Figure 93 where all the fault current for three different locations along feeder 1 are having the same magnitude. In the other words, the fault current can be calculated as the sum of short-circuit current contribution from wind farm and HVDC.

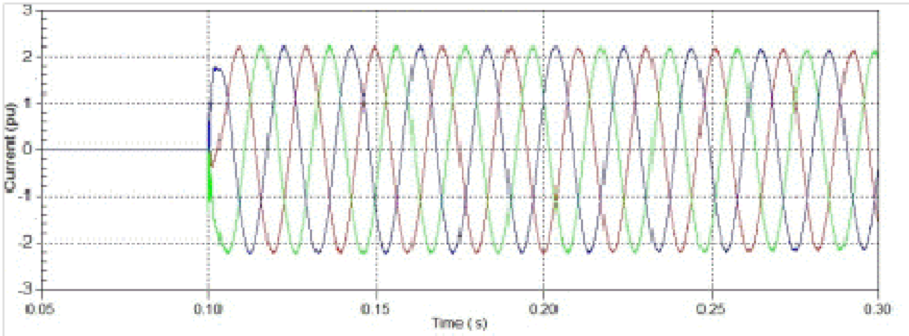

(a)

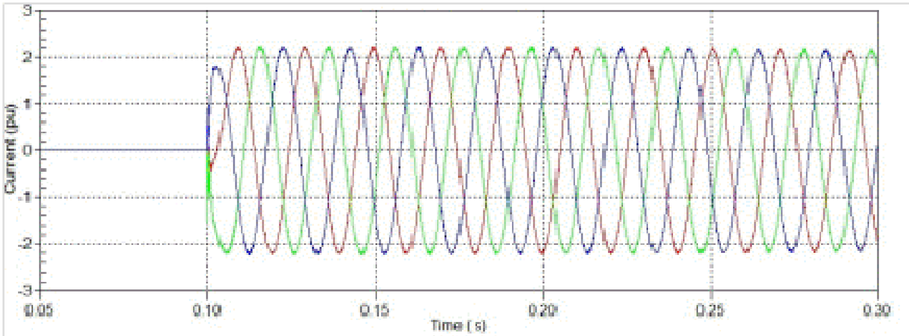

(b)

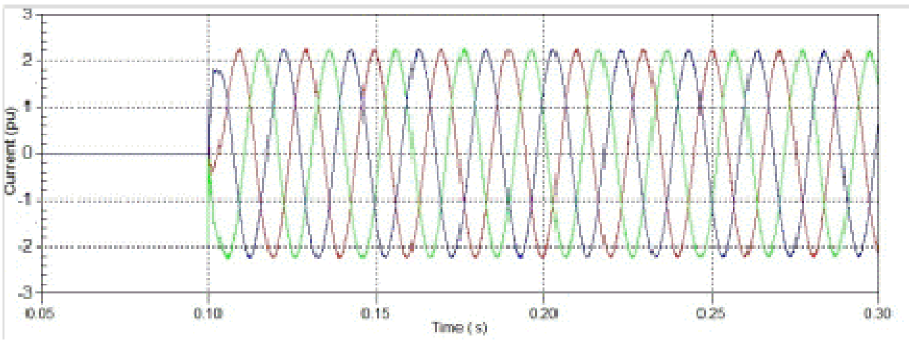

(c)

Figure 93: Fault current when fault is located in: (a) location 1; (b) location 2; and (c) location 3

5.1.3 Different wind speed conditions

Figure 94 shows the peak current measured in the collection point. Two different wind speed conditions are considered, i.e. high wind speed (13 m/s) and low wind speed (5 m/s). The '*' and '+' sign represent the low wind condition, while the 'O' and '◇' sign represent the high wind condition. As can be seen in Figure 94 both low wind and high wind condition give the same peak current, because during short-circuit condition each FCG only supply reactive power.

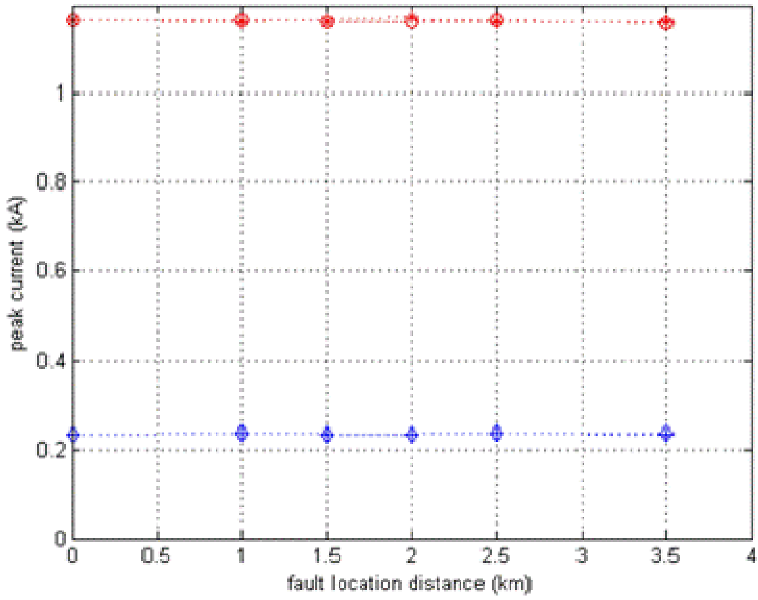

Figure 94 Peak current at the faulty feeder (red) and healthy feeder (blue) during fault for different fault location and different wind speed condition

5.1.4 Maximum fault clearing time

During a short-circuit fault, the thermal energy is developed in the cable and depends on the short-circuit magnitude and duration. The maximum short-circuit current allowed to flow in the cable due to thermal limitation can be formulated as follows [0]:

$$i_{sh} = \frac{i_{1s}}{\sqrt{t_{sh}}} \qquad (0)$$

where $\boldsymbol{i_{sh}}$ is the short-circuit current [kA] during time $\boldsymbol{t_{sh}}$, $\boldsymbol{i_{1s}}$ is the short-circuit rating during 1 second (provided in [0]), and $\boldsymbol{t_{sh}}$ is the short-circuit duration [second]. For XLPE insulated conductors, the maximum allowable short circuit temperature is 250 °C.

From the previous subsection, short-circuit current that flows in the wind farm collection grid is equal to 2.2 p.u. or equal to 0.979 kA, inserting this into (0) the maximum fault clearing time for the feeder line cable is equal to 1.7 minute. The short-circuit current contribution from HVDC is 1.1 p.u. or equal to 0.490 kA, the maximum fault clearing time for the cable connecting collection grid to the SE-HVDC terminal is equal to 2 hours.

5.2 Fault detection

5.2.1 Collection point

The main objective of having the fault detection method in the collection point is to discriminate between the faulty and the healthy feeder. The measurement units (voltage and current meters) are placed in the incoming feeder (feeder 1, 2, and 3) and outgoing feeder (HVDC feeder), as depicted in Figure 95.

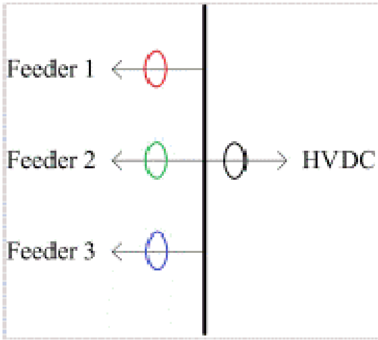

Figure 95: The ellipses indicate the measurement units (MUs) in the collection point

5.2.1.1 Peak current behavior

As can be seen in Figure 96, the peak current flowing into the faulty feeder has the same magnitude regardless the location of the fault. The peak current in the faulty feeder equals to 1.16 kA (≈ 1.83 p.u.), while in the healthy feeders equals to 0.23 kA (10% above their rated current). Therefore the discrimination between faulty and healthy feeder can be achieved by observing the peak current during the fault.

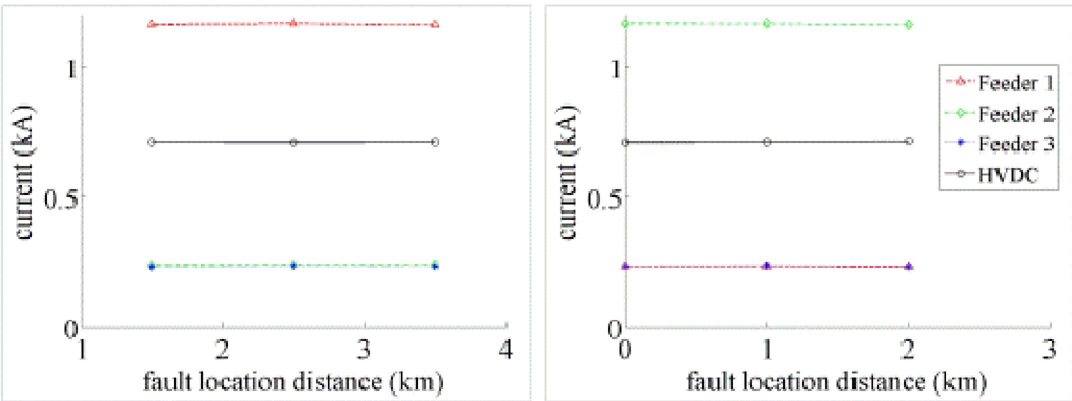

(a) (b)

Figure 96: Peak current magnitude during fault located in (a) feeder 1, and (b) feeder 2

5.2.1.2 Instantaneous active power behavior

When fault occurred in the system, the system voltage and the active power flow are reduced. The direction of the active power also changes toward the faulty point. As can be seen in Figure 97(a), the direction of the instantaneous active power in the HVDC feeder and feeder 1 are changed after the fault occurs in feeder 1, while when the fault is occurred in the HVDC terminal, there are no reverse direction of the instantaneous active power flow.

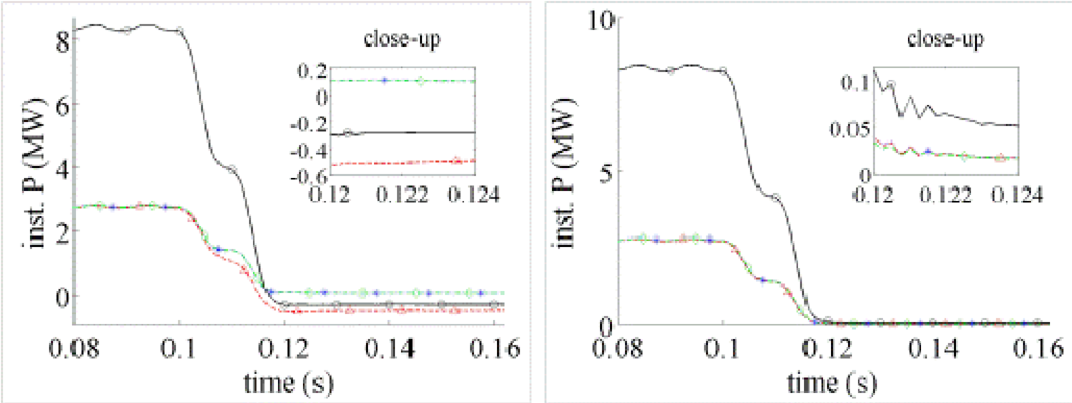

(a) (b)

Figure 97: Instantaneous active power behavior when the fault is occurred in (a) location 1, and (b) SE-HVDC terminal

The instantaneous active power during the fault is shown in Figure 97. By observing the instantaneous active power sign (flow direction), the faulty feeder can be identified.

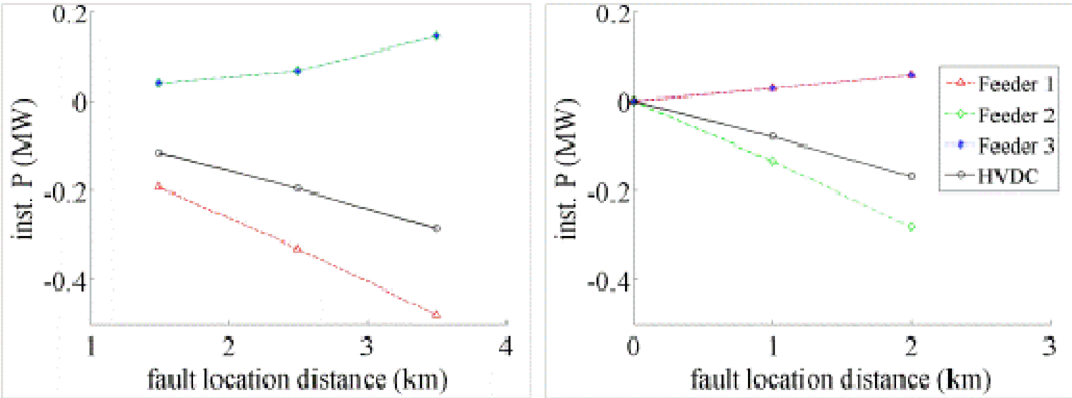

(a) (b)

Figure 98: Instantaneous active power during fault in (a) feeder 1, and (b) feeder 2

5.2.1.3 Current differential behavior

As can be seen in Figure 99, the current differential signal is too noisy to be used to discriminate the faulty and healthy feeder.

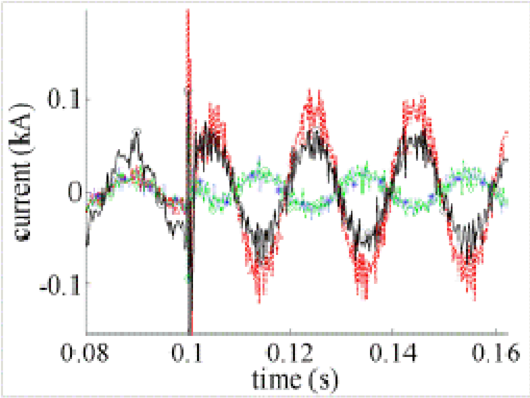

(a)

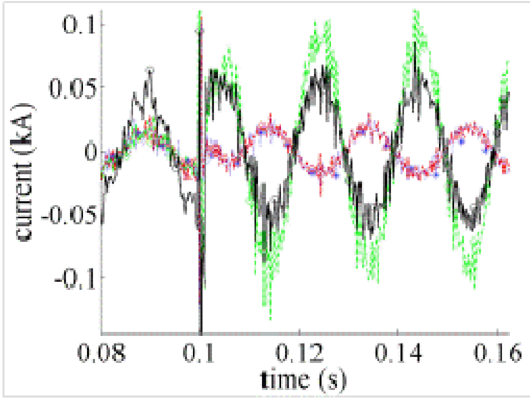

(b)

Figure 99: Current differential behavior when fault occurred in (a) feeder 1, and (b) feeder 2

5.2.1.4 Current harmonics behavior

As can be seen in Figure 100 and Figure 101, discontinuity occurs in the current harmonics other then the fundamental frequency. This behavior does not depend on the fault location. It is also shown that the magnitude of the discontinuity in the faulty feeder is much larger than the healthy one. Therefore, there is possibility to use the current harmonics spectrum to detect the faulty feeder.

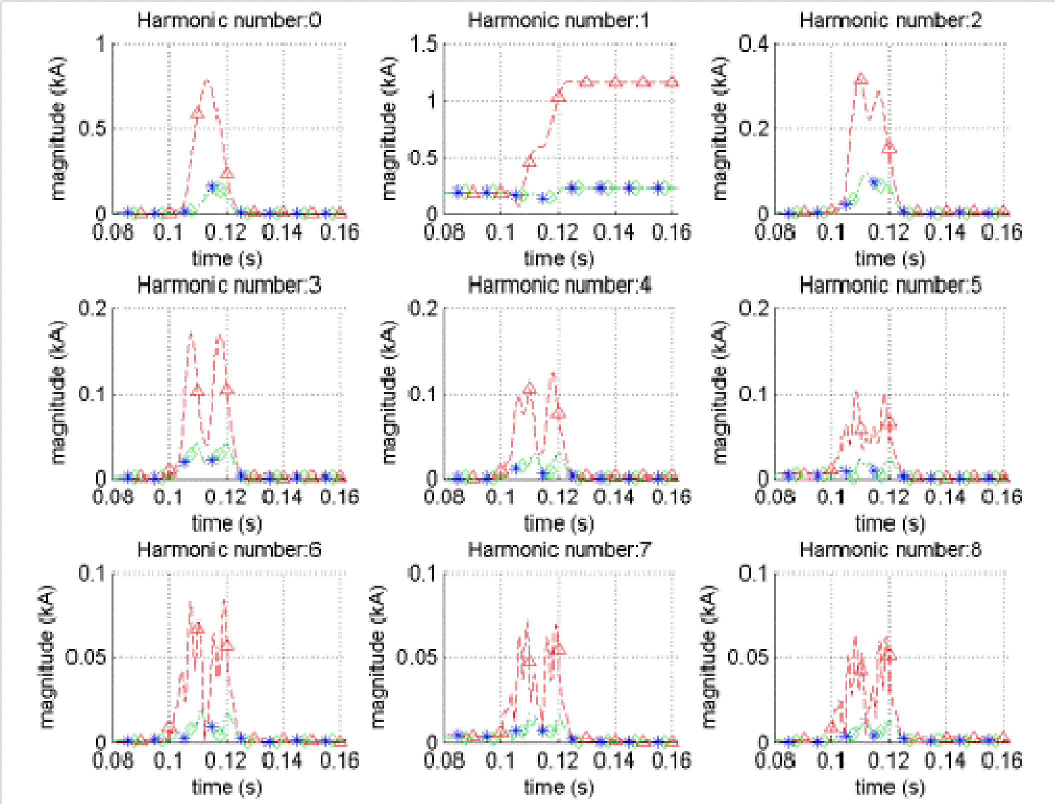

Figure 100: Current harmonics behavior when fault occurred in feeder 1

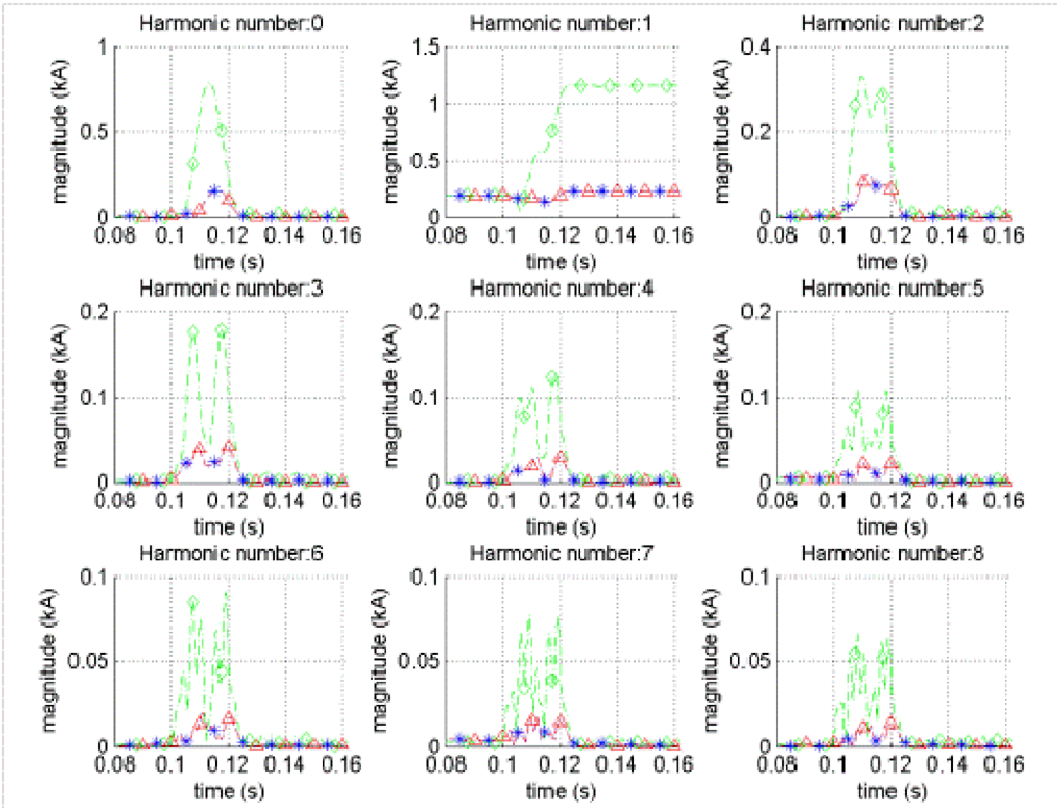

Figure 101: Current harmonics behavior when fault occurred in feeder 2

5.2.1.5 Detection of faulty feeder

After observing the behavior of the signals in the collection point, the detection of faulty feeder can be done using the flowchart depicted in Figure 102. The first step is to observe the instantaneous active power direction in the HVDC feeder. Then the next step is to investigate the peak current value. If the conditions in both step are fulfilled by feeder x, then the fault is occurred in feeder x.

Fault detection by observing only the instantaneous active power direction is not suggested, because during the starting state of the system, instantaneous active power from the HVDC may flow towards the wind farm (reverse direction).

Fault detection by measuring only the peak current is also not suggested, since the peak current may introduce a problem due to fast transient occurred in the system.

The behavior of the current harmonics may also be used to detect the faulty feeder. But other transient in the system, e.g. switching of the circuit breaker, is also interference the harmonic spectrum of the current which may result the similar behavior as presented in this study. Therefore, further study is needed in order to include current harmonics in the fault detection method.

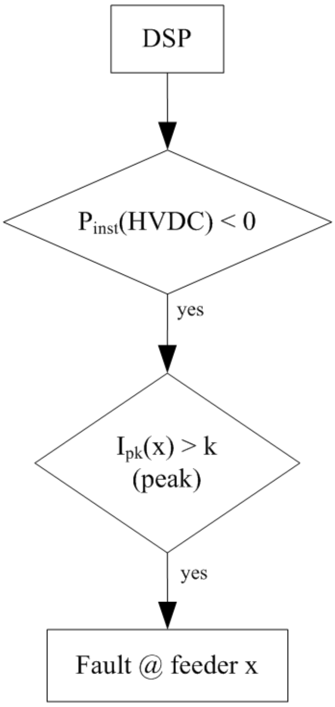

Figure 102: Proposed method for detecting the faulty feeder

5.2.2 Feeder line

The main objective of having the fault detection method in the feeder line is to identify the faulty section within a feeder line. It is assumed that the fault is occurred in feeder 1. There MUs are placed in three different locations as depicted in **Fel! Hittar inte referenskälla.**.

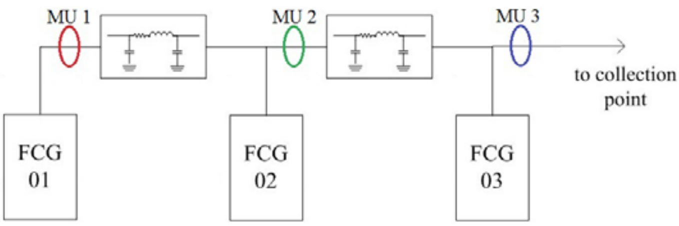

Figure 103: The ellipses indicate the measurement points along the feeder line

In order to see the difference between faulty and healthy section within a feeder, the following analysis will be focused only during Fault 1 and Fault 2. Which means that during Fault 1, the faulty section is the one between FCG 01 and 02, while during Fault 2, the faulty section is the one between FCG 02 and 03.

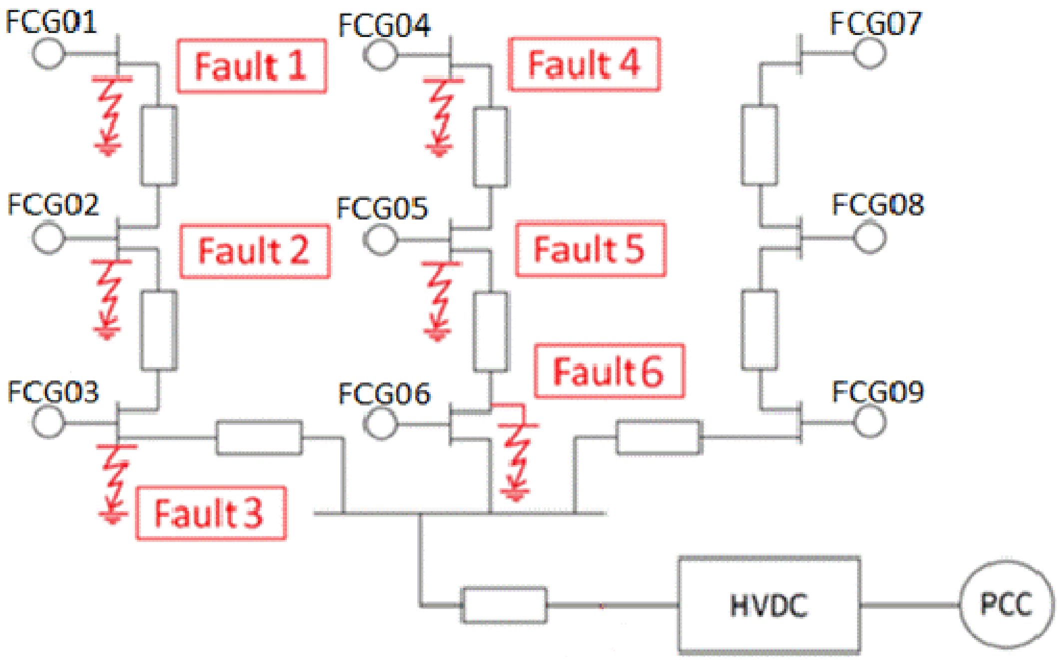

Figure 104: Different fault locations for the short-circuit simulation

5.2.2.1 Peak current behavior

In Figure 105(a), the peak current difference during fault between MU 1 and MU 2 is 1.15 kA (≈ 1.83 p.u.), while the difference between MU 2 and 3 is only 0.075 kA (≈ 0.12 p.u.). During Fault 2 (Figure 105(b)), the peak current difference during fault between MU 2 and MU 3 is 0.99 kA (≈ 1.5 p.u.), while between MU 1 and MU 2 is only 0.082 kA (≈ 0.12 p.u.). This behavior shows the possibility to use the peak current difference between two contiguous MUs for detecting the faulty section within a feeder.

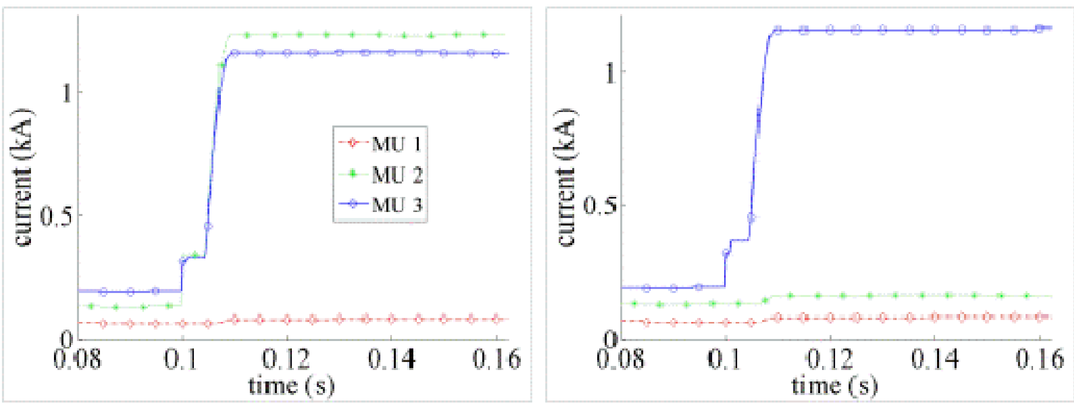

(a) (b)

Figure 105: Peak current behavior during (a) Fault 1, and (b) Fault 2

5.2.2.2 Peak voltage behavior

Figure 106 indicates that during the fault, peak voltage in three different locations is less than 500 volt (or less than 0.017 p.u.). This means that it will be hard to use the magnitude of the voltage to discriminate the healthy and the faulty feeder.

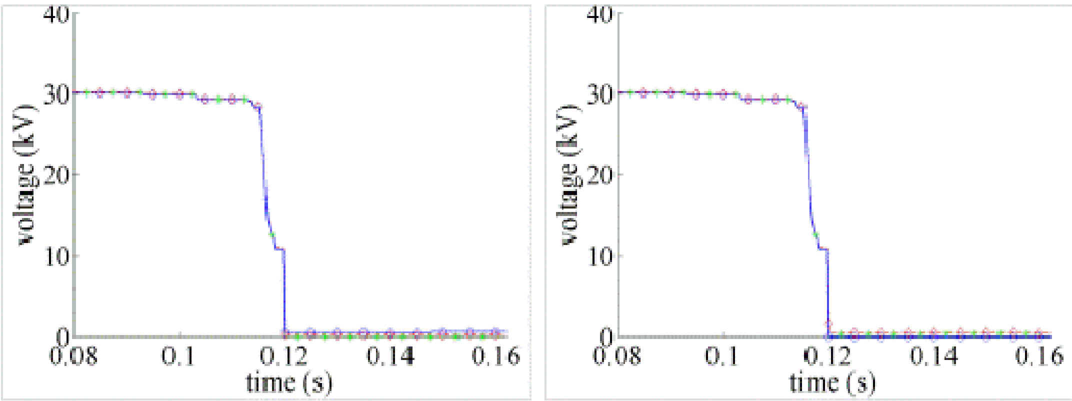

(a) (b)

Figure 106: Peak voltage behavior during (a) Fault 1, and (b) Fault 2

5.2.2.3 Instantaneous active power behavior

As explained before, the direction of the active power flow during fault is toward the faulty point. As can be seen in Figure 107(a), during Fault 1, the instantaneous active power in MU 3 is equal to -0.13 MW, and in MU 1 is equal to 798 W. In Figure 107(b), instantaneous active power in MU 1 is equal to 2.9 kW and MU 2 is equal to 3.3 kW. The instantaneous active power in the faulty point is equal to zero, since the voltage at that point is also zero. It may be hard to have the relay selectivity based on the magnitude of the instantaneous active power, but if communication link between two contiguous MUs is available, the direction comparison of the instantaneous active power may be used for detecting the faulty section within a feeder.

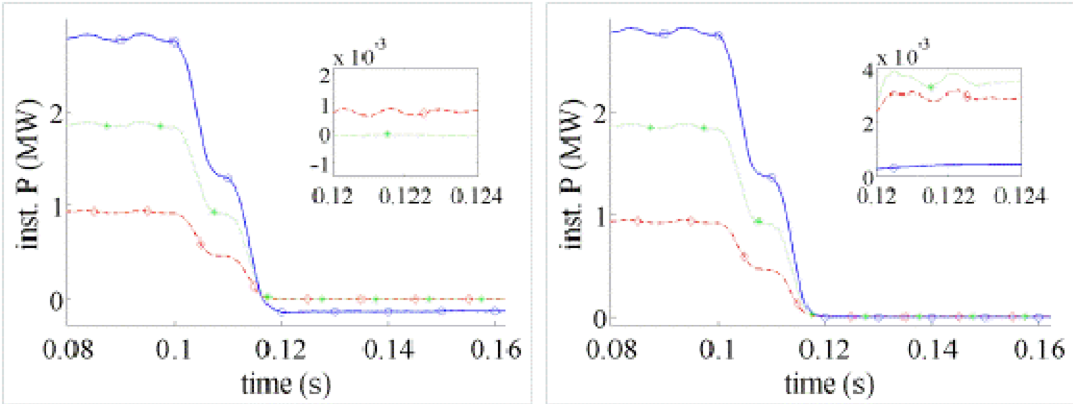

(a) (b)

Figure 107: Instantaneous active power behavior during (a) Fault 1, and (b) Fault 2

5.2.2.4 Voltage differential behavior

The differential of the voltage as depicted in Figure 108 cannot be used to identify the faulty section since the signal is too noisy and the magnitude is very low.

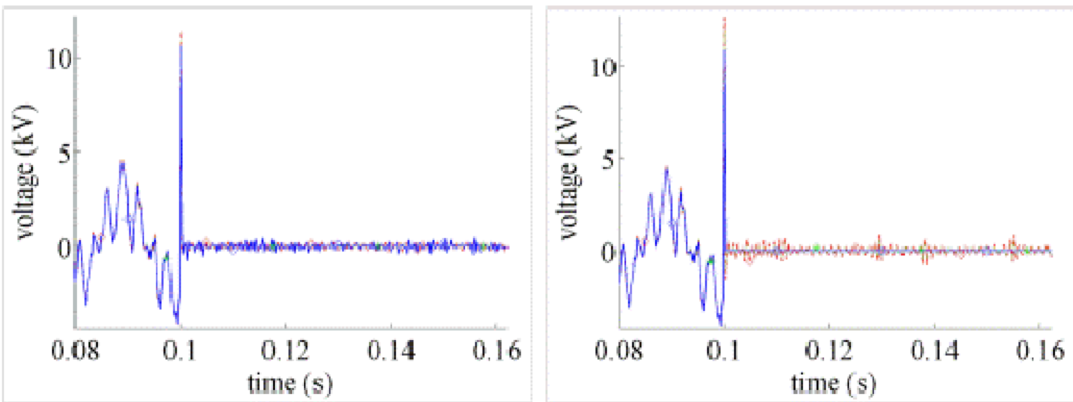

(a) (b)

Figure 108: Voltage differential behavior during (a) Fault 1, and (b) Fault 2

5.2.2.5 Positive sequence L-G impedance behavior

The positive sequence L-G impedance value, as can be calculated using (0), is changing right after the fault initiated. As can be seen in Figure 109, in the normal condition all positive sequence L-G impedance in three MUs is having the positive resistance (real value of impedance). When fault is initiated these impedance is reduced and equal to zero after reaching fault steady-state.

The trajectory of the positive sequence L-G impedance in different MUs may be different for the different fault location. Figure 46 shows the closer look on the impedance behavior 0.0073 seconds after the fault is initiated. It can be clearly seen in Figure 110(a) that the impedance in the MU 1 is moving towards zero through the positive imaginary values, while the other two MUs are moving through the negative imaginary values. During Fault 2 (Figure 110(b)), impedance in the MU 1 and MU 2 are moving through the positive imaginary value. By comparing the trajectory between two measurement points, the faulty section within the line can be identified.

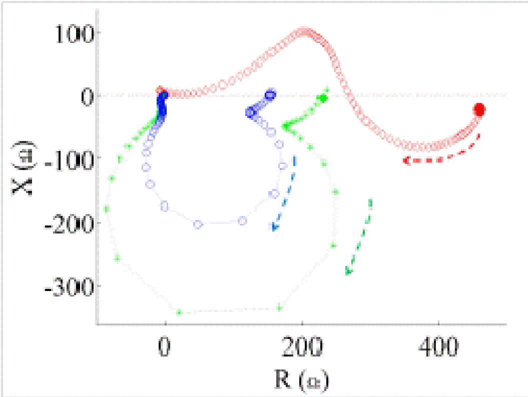

Figure 109: Positive sequence L-G impedance behaviors during Fault 1, the dashed arrows represent the movement direction

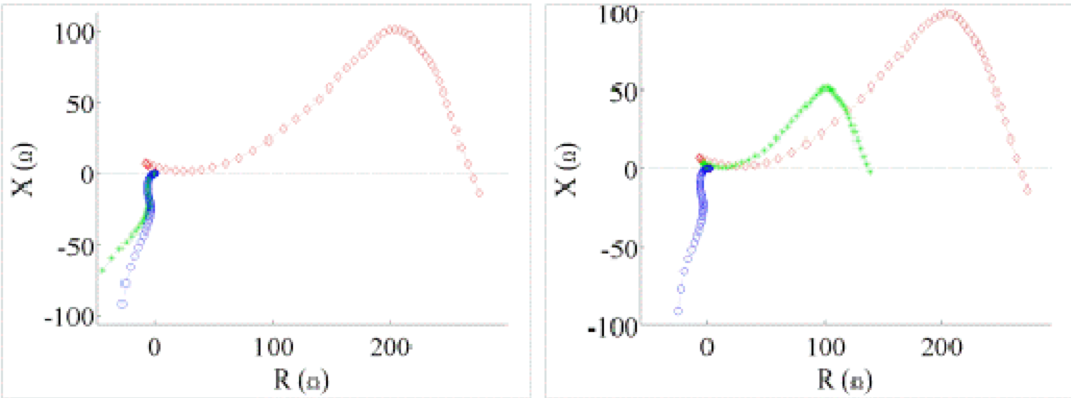

(a) (b)

Figure 110: Closer look in positive sequence L-G impedance behavior during (a) Fault 1 and (b) Fault 2

5.2.2.6 Detection of faulty section within a feeder line

After observing the behavior of the signals in the collection point, the detection of faulty feeder can be done using the flowchart depicted in Figure 111. The faulty section can be detected by comparing the peak current between two contiguous MUs, or comparing the direction of the instantaneous active power or the positive sequence L-G impedance between MUs. It means that the communication line between MUs is needed to have selectivity in the feeder line protection system.

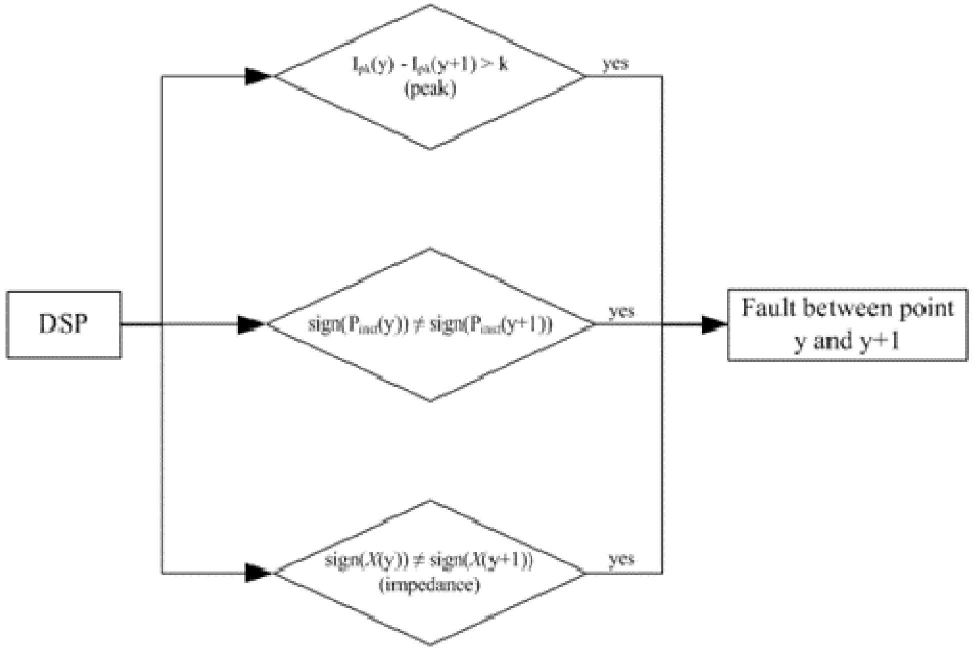

Figure 111: Proposed method for detecting the faulty section within a feeder

5.3 Different simulation scenarios

In the following subsections, short-circuit simulations are performed for different system conditions. The purpose of these simulations is to test the proposed fault detection method for different system conditions. The presented results in the following figures are for fault located in location 2 (Fault 2).

5.3.1 Different sampling frequency

By changing the sampling frequency of the A/D converter, the accuracy of the DSP analysis can be changed. The DSP result when using two different sampling frequencies (4 and 10 kHz) are shown.

As can be seen in Figure 112- Figure 113, there are no significant difference between 4 kHz and 10 kHz sampling frequency DSP results.

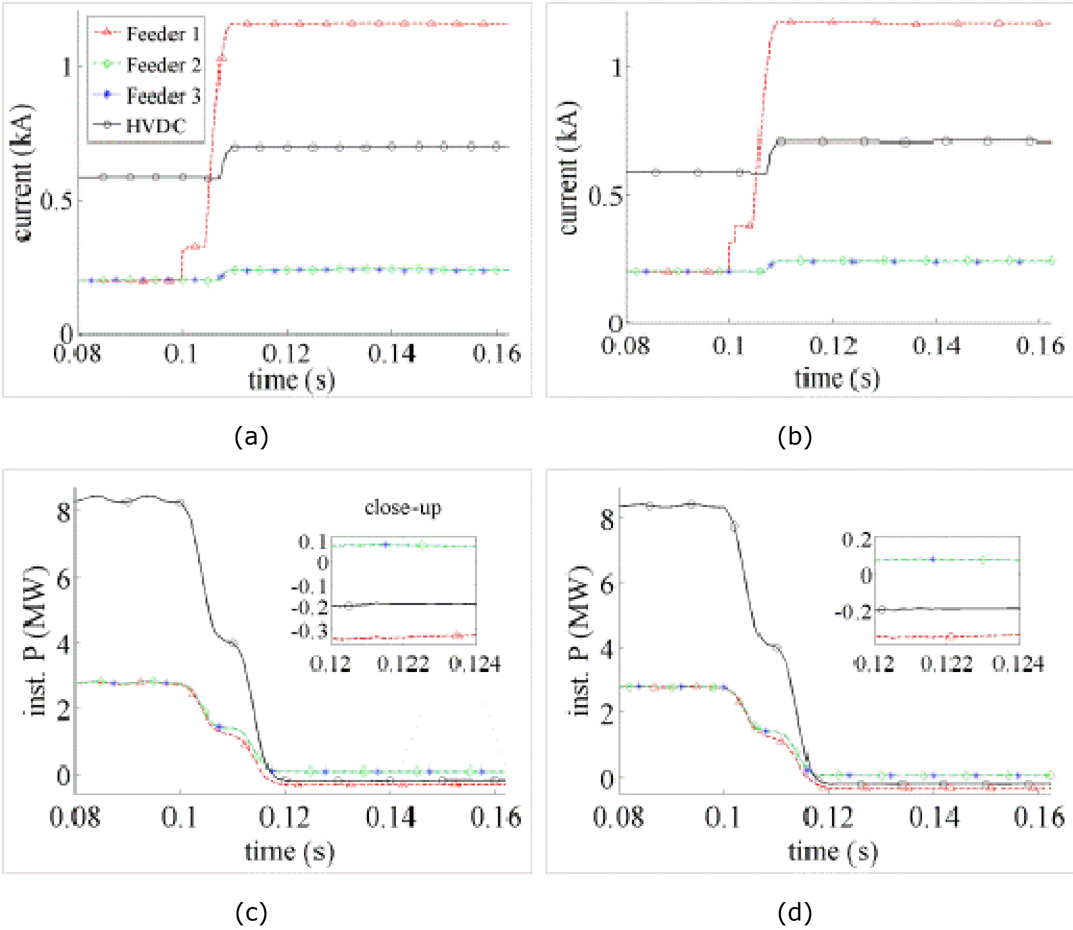

Figure 112: (a) and (c) show the peak current and the instantaneous active power behavior in the collection point for 4 kHz sampling frequency, while (b) and (d) are for 10 kHz sampling frequency

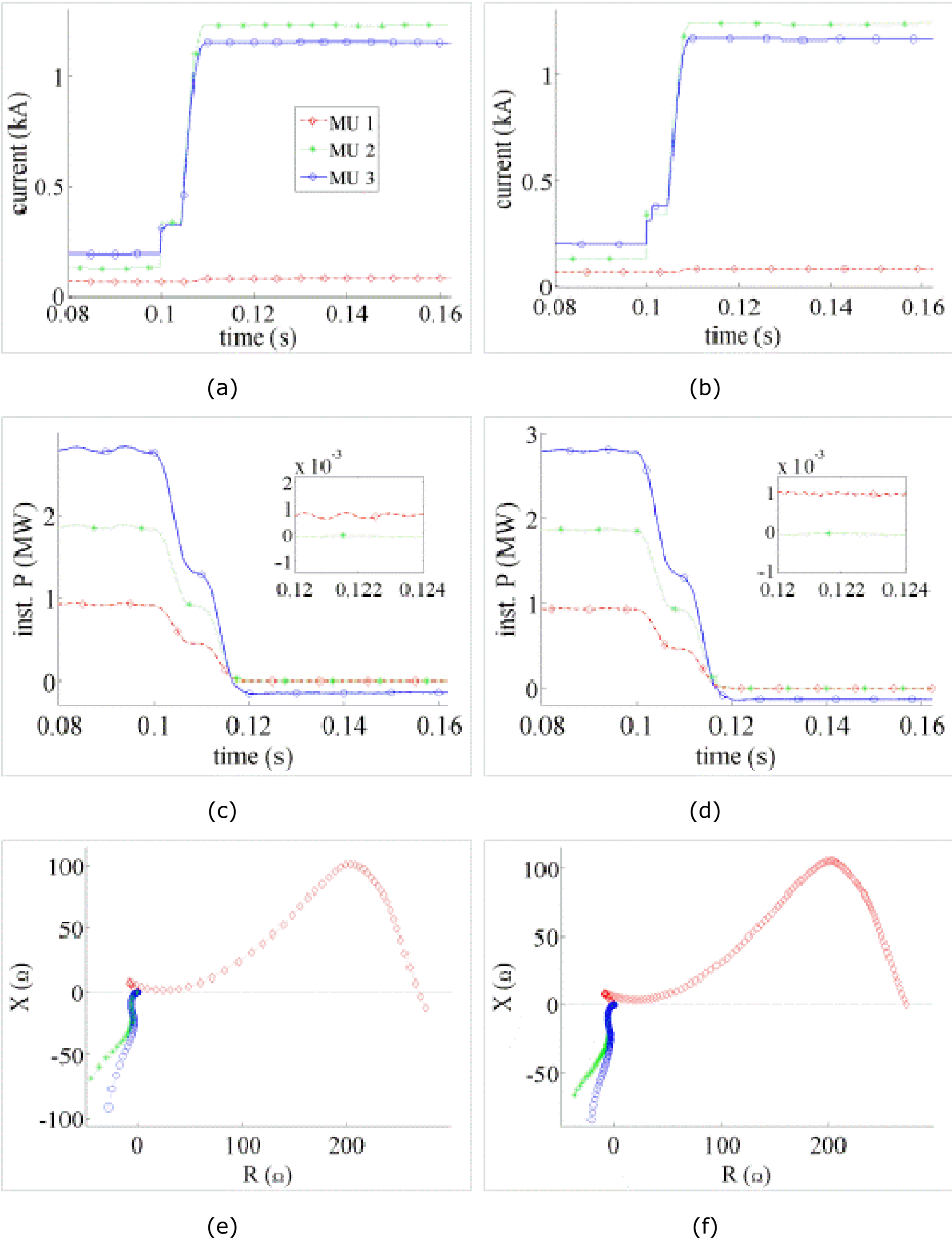

Figure 113: (a), (c), and (e) show the peak current, the instantaneous active power, and the positive sequence L-G impedance behavior in feeder 1 for 4 kHz sampling frequency, while (b), (d), (f) are for 10 kHz sampling frequency

5.3.2 Different wind turbines condition

Due to some reasons, e.g. maintenance, FCG 02, 04, 06, 08, and 09 are disconnected from the system (depicted in Figure 71). This means that when fault occurs, only 4 FCGs are contributing to the fault. The fault current is reduced from 2.2 p.u. to 1.59 p.u. The DSP results when only 4 FCGs connected to the system are shown in the following figures.

The current peak behavior, as depicted in Figure 114(a), has higher value right after the fault is initiated. This is due to the transient current that occurred in the system. During the fault steady-state, peak current in feeder 1 is equal to 0.85 kA (≈ 1.34 p.u.) or decreased 0.31 kA as compared to the base case (when all turbines are in service).

The behavior of the instantaneous active power Figure 114(b) is as same as their behavior in the base case. This also happens in the feeder line, Figure 115.

It can be concluded that the proposed fault detection methods still work properly for this condition.

3

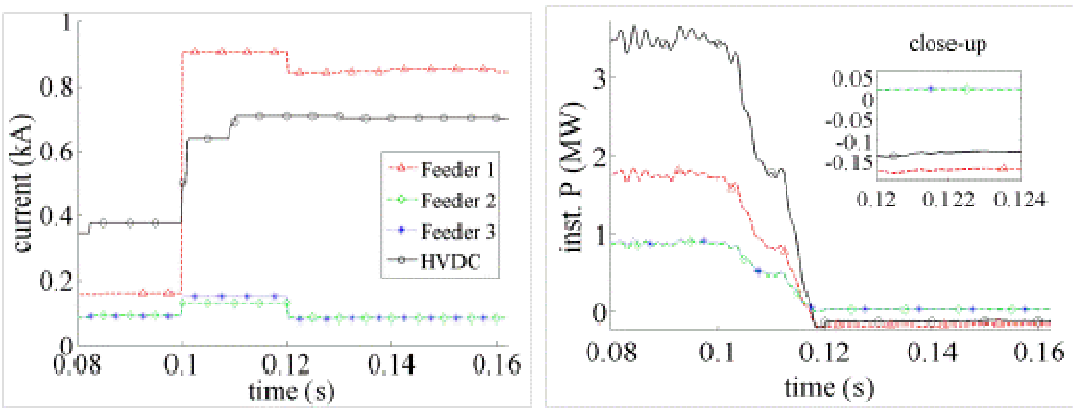

(a) (b)

Figure 114: (a) the peak current behavior, (b) the instantaneous active power behavior in the collection point

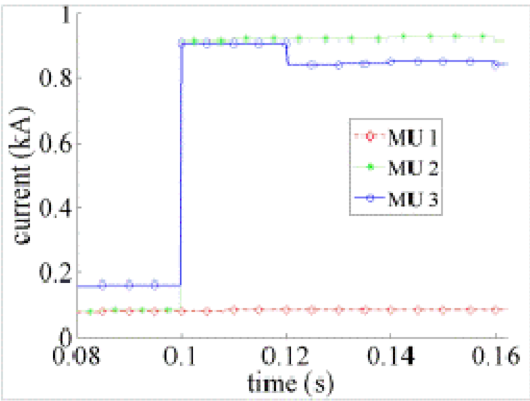

(a)

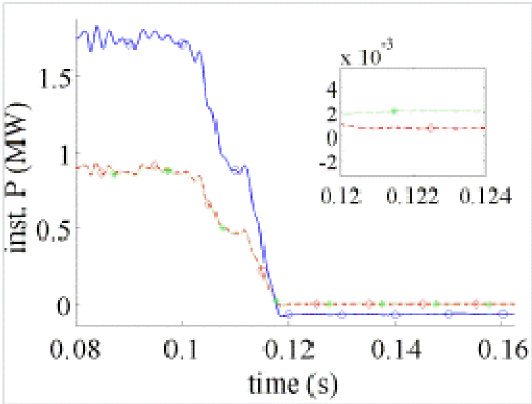

(b)

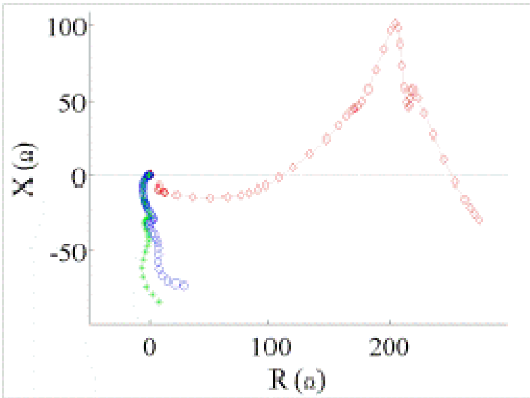

(c)

Figure 115: (a) the peak current behavior, (b) the instantaneous active power behavior, (c) the positive sequence L-G impedance behavior in feeder 1

5.3.3 Different wind turbines and HVDC power rating

In this case, the turbines power rating is changed into 5 MW and 1.5 MW, and the HVDC power rating is changed into 45 MVA and 13.5 MVA respectively. In this study, all converters are assumed to be ideal, therefore the scaling of the system can be achieved easily by scaling up the FCG and HVDC rated power. While in the real system, a lot of things, such as the power electronic switches, controller gain, transformers, circuit breakers, are need to be considered before changing the system rating. The DSP results are shown in the following figures.

As can be seen in Figure 116 - Figure 119, the behavior of the results are all the same. The differences in magnitude are due to the difference of the system rating. Therefore, the proposed method can still be used for different system rating.

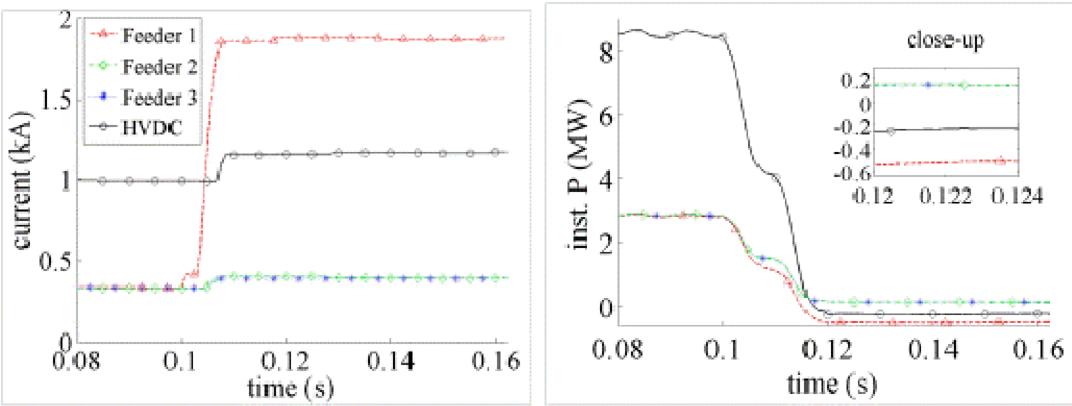

(a) (b)

Figure 116: (a) the peak current behavior, (b) the instantaneous active power behavior in the collection point for 5 MW turbines

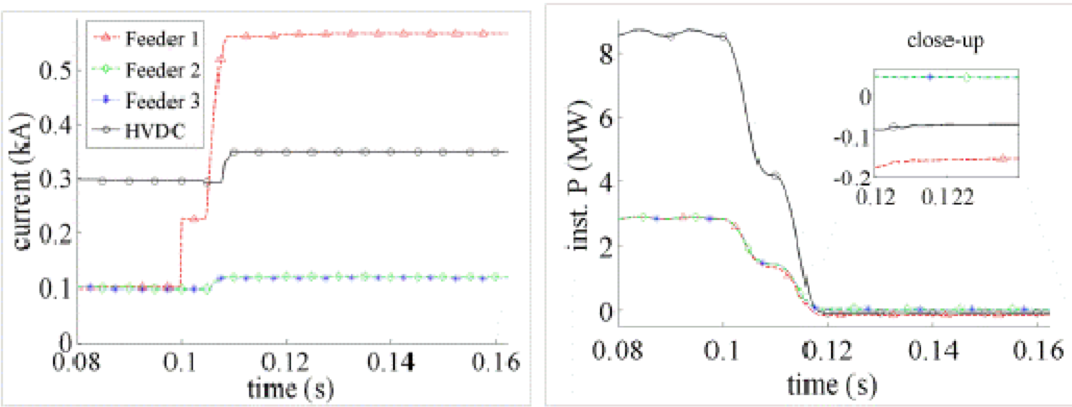

(a) (b)

Figure 117: (a) the peak current behavior, (b) the instantaneous active power behavior in the collection point for 1.5 MW turbines

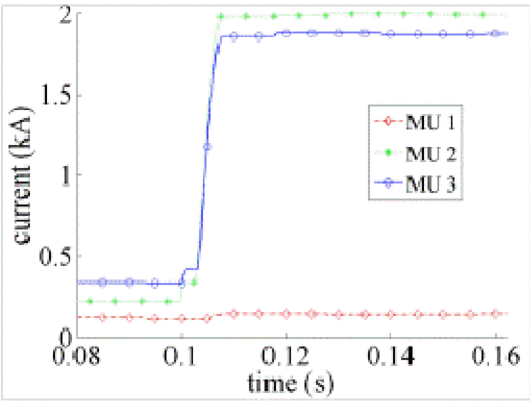

(a)

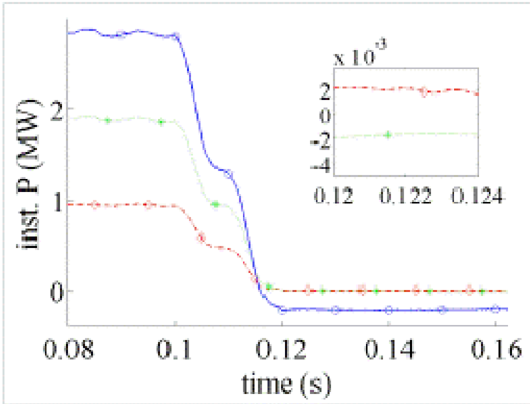

(b)

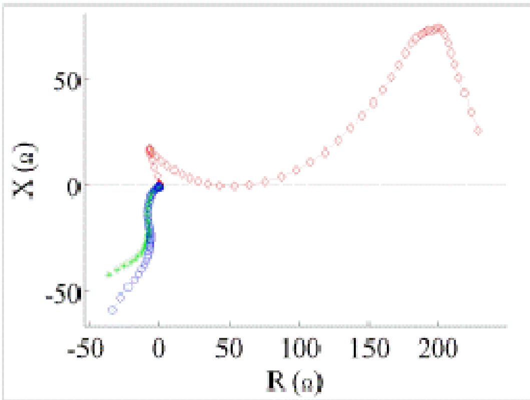

(c)

Figure 118: (a) the peak current behavior, (b) the instantaneous active power behavior, (c) the positive sequence L-G impedance behavior in feeder 1 for 5 MW turbines

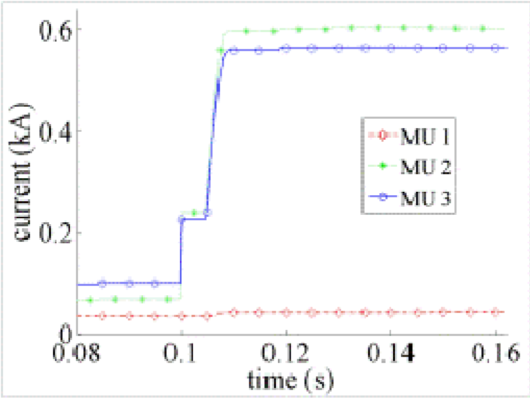

(a)

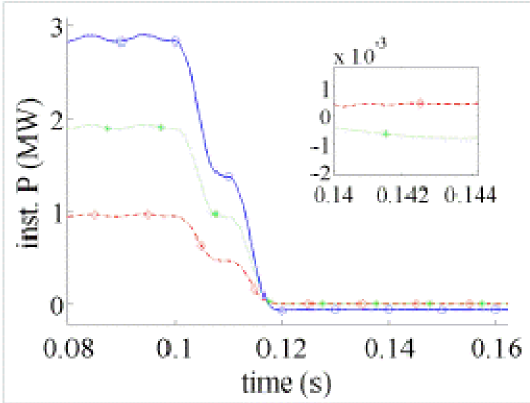

(b)

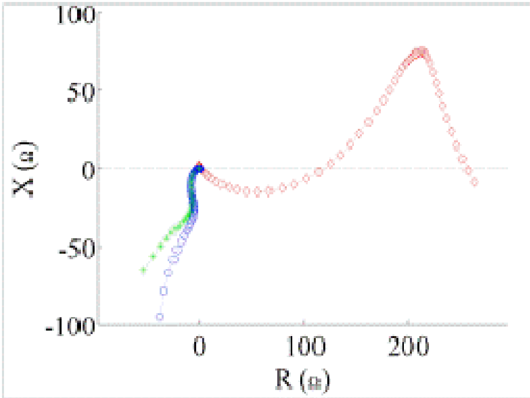

(c)

Figure 119: (a) the peak current behavior, (b) the instantaneous active power behavior, (c) the positive sequence L-G impedance behavior in feeder 1 for 1.5 MW turbines

5.4 Fault detection method validation

After having the fault detection methods in the collection point and feeder line then these methods are implemented and validated using protection relay model in PSCAD/EMTDC. Relay model that are used are the directional power relay (relay number 32), over-current relay (50), current differential (87) and positive sequence L-G impedance (21).

5.4.1 Relay model and setting

In the following sub section the relay models that are used to validate the proposed fault detection methods are explained. The settings of the relays are based on the base test case where all wind turbines rating are 3 MW.

5.4.1.1 Over-current relay

This relay model has been explained in 4.4.1.1. The threshold current is set to 0.62 kA or 3 time normal feeder current. Since the reduced short-circuit current contribution from SE-HVDC to very small value (0.1 p.u.) is not recommended, this threshold current is found to be satisfy the requirement.

5.4.1.2 Current differential relay

This relay model has been explained in 4.4.1.2. The differential threshold current is set to 0.62 kA or 10 times larger than the rated current difference between two measurement units along feeder line.

5.4.1.3 Positive-sequence L-G relay

The trip polygon element in PSCAD/EMTDC is chosen for comparing the positive sequence L-G impedance trajectory. This element checks whether or not a point described by inputs R and X, lies inside a specified region on the impedance plane. If the point lies inside the region then the relay output is '1', otherwise is '0'.

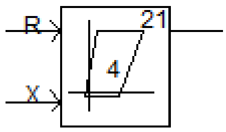

Figure 120: Trip polygon element

Since only the trajectory is observed, the trip region is set to be located in the third quadrant. Therefore if the fault is located backward then the relay output is '1', while if the fault is located forward then the relay output is '0' (no change).

5.4.1.4 Directional power relay

The directional power relay is used to detect the active power flow direction in the HVDC feeder as well as along the feeder line. The principle of this relay is to compare the active power with the zero point. If the active power is positive then the relay output is '0', while if the active power is negative then the relay output is '1'.

Since this relay is not implemented in the PSCAD/EMTDC standard library, logic gates are built to realize the behavior of the directional power relay.

5.4.2 Validation results

The faulty part of the system can be identified by arranging the relay mentioned in the previous sub section into the proposed fault detection methods as depicted in Figure 102 and Figure 111.

5.4.2.1 Collection point

The following figures only shows the trip signal in collection point when the faults are located in location 2 and location 5. The same trip signal is found to be same for the other fault location within feeder 1 and 2.

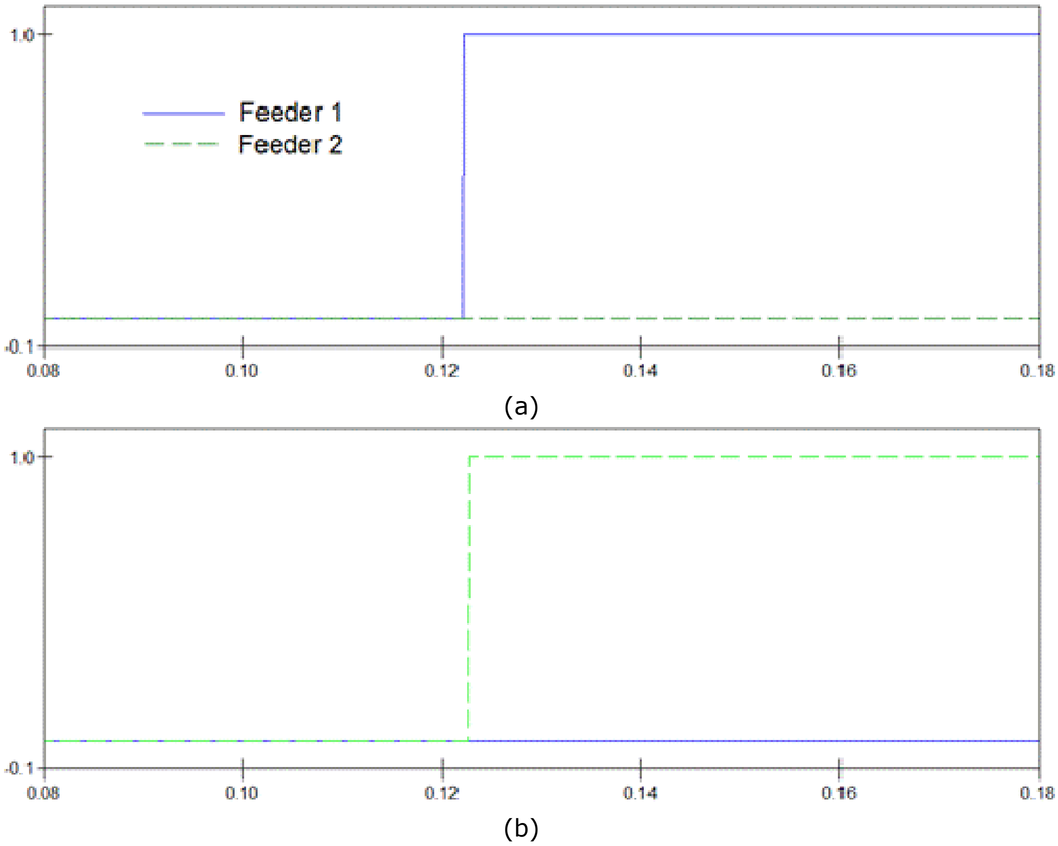

Figure 121: Fault is detected in: (a) feeder 1 and (b) feeder 2 after 0.022 seconds from the fault instance

Figure 121 shows the behavior of the fault detection method placed in the collection point when fault is occurred in location 2 (Figure 121a) and location 5 (Figure 121b). As can be seen in Figure 121, the fault is detected one cycle after the fault initiated (fault occurred at 0.1 s), due to the active power zero-crossing time.

5.4.2.2 Feeder line

The following figures only show the fault detection validation in feeder 1. The same trip signal is found to be same for the other fault.

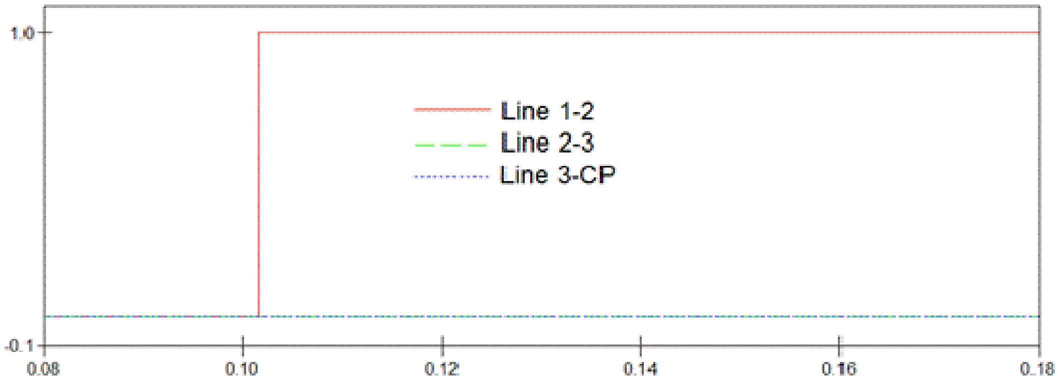

(a)

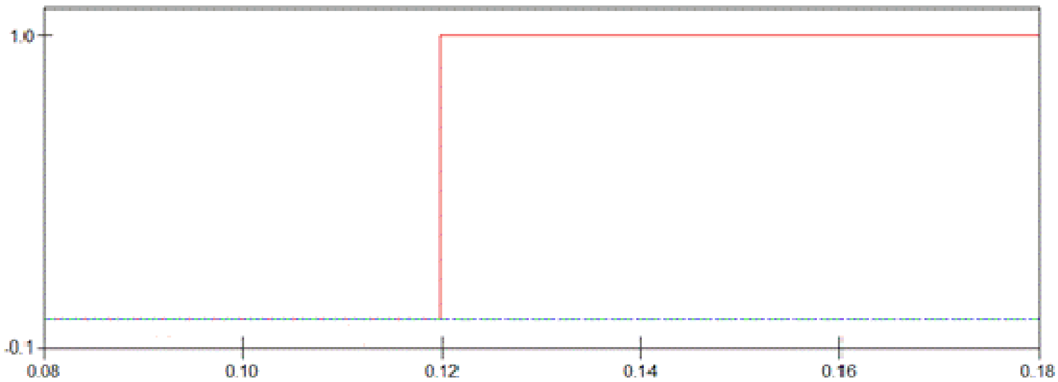

(b)

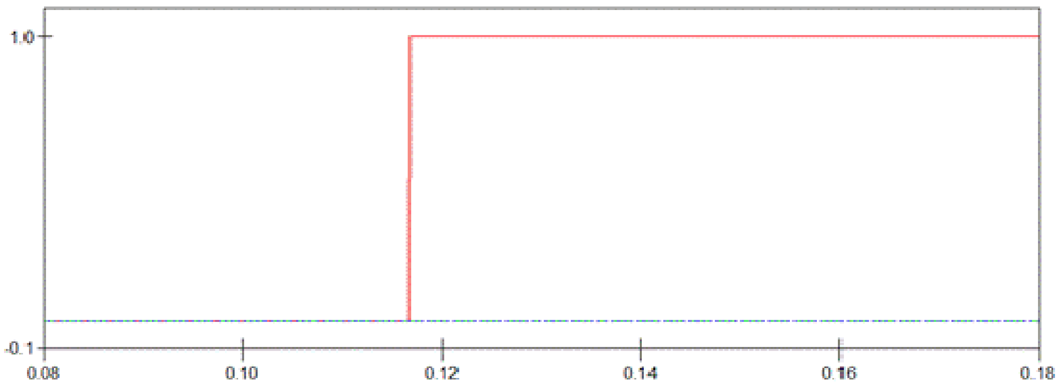

(c)

Figure 122: Fault is detected in line 1-2 (Fault 1) by using: (a) current differential relay, (b) power direction relay, and (c) impedance relay

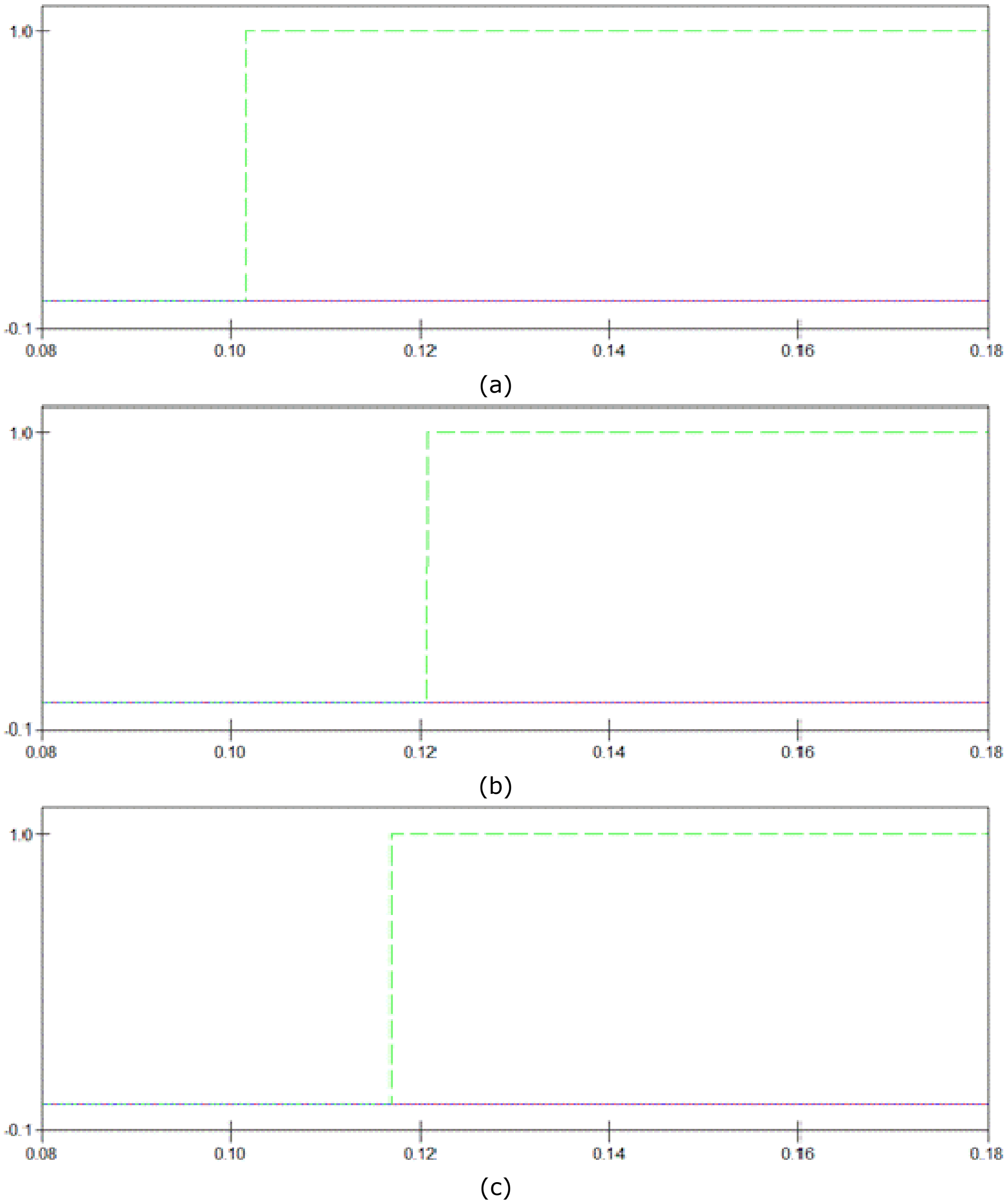

Figure 123: Fault is detected in line 2-3 (Fault 2) by using: (a) current differential relay, (b) power direction relay, and (c) impedance relay

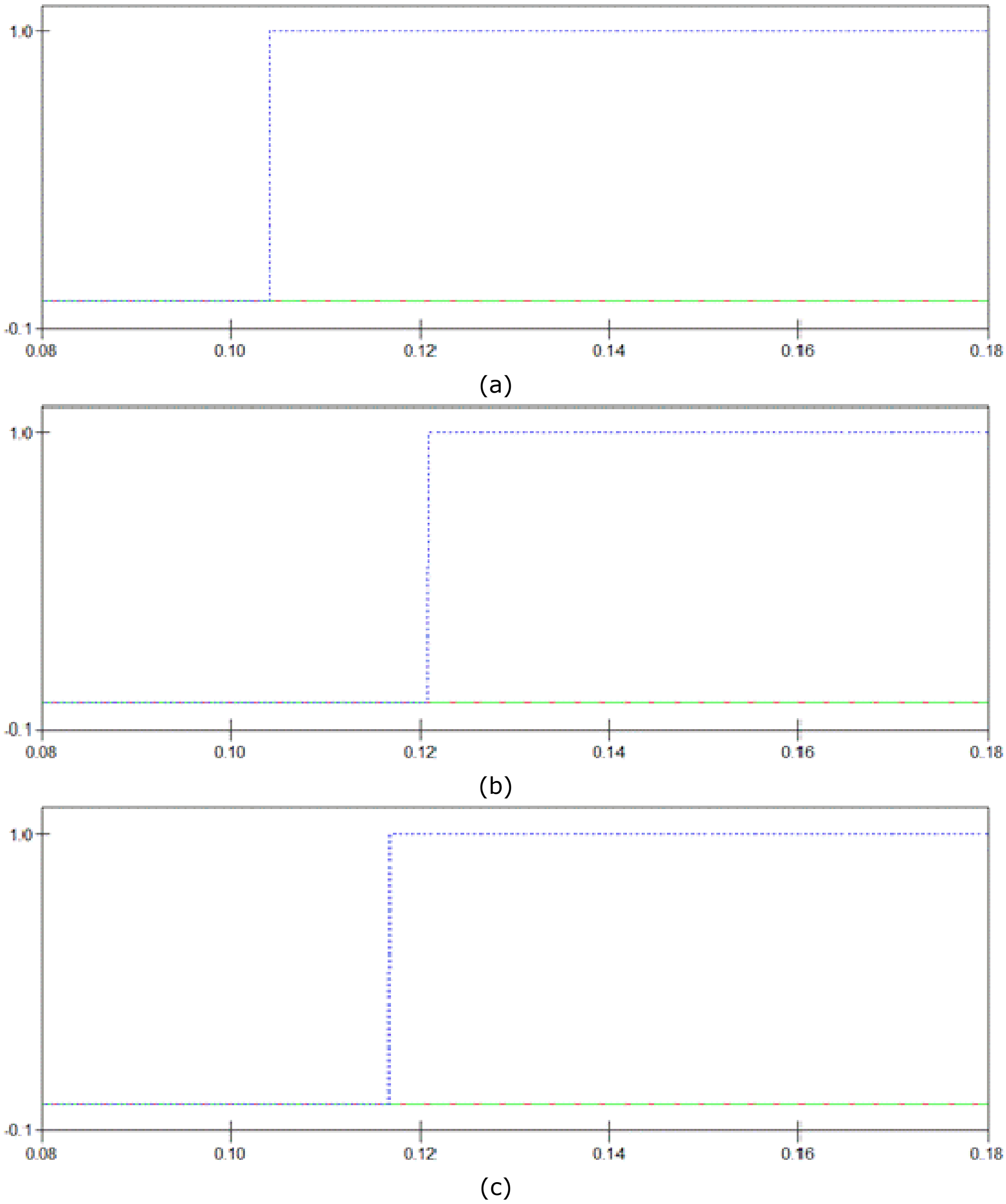

Figure 124: Fault is detected in line 3-CP (Fault 3) by using: (a) current differential relay, (b) power direction relay, and (c) impedance relay

Figure 122 shows the feeder line fault detection output for Fault 1, while Figure 123 and Figure 124 is for Fault 2 and 3, respectively. As can be seen the proposed method can detect the faulty section within feeder line correctly. The active power directional relay gives the slowest response to the fault due to the zero-crossing time of the power.

5.5 Conclusion

The simulation studies were performed using simplified model of FCG. The model is good enough to capture the short-circuit behavior for a period of interest (approximately 250 ms) for the instance of fault.

During the fault within the wind farm collection grid, the behavior of the FCG can be represented as constant current source (contributing 10% above rated current), which means that short-circuit current contribution at the terminal of FCG is limited.

Due to the short-circuit current from the FCG limited to 10% above the rated current, the fault detection becomes challenging.

The faulty feeder can be detected by combining the active power direction and the peak current observed at the collection point (Figure 28). Directional power relay and over-current relay can be utilized to accomplish this method. The proposed method has taken about 22 milliseconds for detection of the fault.

Three different methods for identifying the faulty section within a feeder were investigated. These are described below.

- Method 1: compares the peak current magnitude between two ends of the section
- Method 2: compares the direction of the active power between two ends of the section
- Method 3: compares the direction of the positive sequence L-G impedance between two ends of the section

All of these three methods require communication link between two ends of the section. These methods can be accomplished by utilizing the current differential, directional power, and positive sequence L-G impedance relays.

All the three methods were tested on PSCAD/EMTDC simulation setup. The Method 1 has taken 4 milliseconds to detect the faulty section. Method 2 and Method 3 have taken 22 milliseconds, and 18 milliseconds respectively to detect the same faulty section.

Method 2 needs longer time to detect the faulty section as compared to Method 1 because Method 2 works on the information of active power direction. The active power direction does not change instantaneously and takes about one cycle (20 milliseconds) as seen from the simulation.

Method 3 also needs longer time to detect the faulty section as compared to Method 1 because of time required from the DFT analysis for impedance calculation.

6 Conclusions and Future Works

6.1 Conclusions

Large wind farms are being sited in remote locations to minimize environmental impacts and exploit stable wind speed. The distance from the wind farm to the main grid is becoming large and if it exceeds 80 km for offshore or 500 km for onshore, HVDC transmission would be the most cost effective.

The HVDC converters employ power electronic switches designed to carry rated current. They have very limited overload capability. Due to safety reasons the HVDC-link cannot carry abnormally high current in the event of a fault at its terminal. Typically the fault current contribution is limited up to 10% above the rated current. Hence the fault detection in HVDC-connected wind farm becomes a challenging task as compared to HVAC-connected wind farm.

In order to study the behavior of the system under faulty condition, a case study has been implemented in PSCAD/EMTDC software. The case study consists of 9 wind turbines placed on 3 feeders, each feeder having 3 wind turbines. Two different turbine technologies namely DFIG wind turbine and FCG wind turbine were considered at the time. Three-phase short-circuit fault at different locations in collection grid was studied.

For the faults inside the AC collection grid, the affected protection zones are the collector feeder zone (feeder line) and the collector bus zone (collection point) as can be seen in Figure 28. Therefore this study focused on the fault detection in these two zones, i.e. collection point and feeder line. In other words, the protection scheme should first detect and isolate the faulty section and if the faulty section cannot be isolated due to any reasons, the protection scheme should then trip the faulty feeder.

The voltage and current data from simulation was post-processed (digital signal processing/DSP) using sliding data window having 20 milliseconds width (one cycle of 50 Hz) in MATLAB. The peak value of the voltage and current, the fundamental component of voltage and current, the harmonic contents, and the derivative of the voltage and current were obtained. In addition, the instantaneous active power and impedance were also computed.

The fault detection methods were proposed based on the information obtained from the DSP analysis. The trip logics were built by selecting the useful signals from the DSP analysis. The fault detection logics then were tested on the studied system implemented in PSCAD/EMTDC environment. This study shows that the proposed logics were able to detect the fault in both AC collection grids, one with DFIG and the other with FCG wind turbines.

In the wind farm with DFIG wind turbines, the behavior of a single DFIG during fault is similar to wound rotor induction generator because the crowbar is activated to protect the converter from high current. Short-circuit current contribution from a single DFIG may reach 6-10 times higher than its rated current. The feeder current measured in the collection grid during the fault also reach more than 15 times the normal feeder current because of short-circuit contributions from other wind turbines.

The faulty feeder can be detected by observing the peak current at the collection point. Over-current relay can be utilized to accomplish this objective. The studies show that the over-current relay has taken 5 milliseconds for detection of the fault.

The faulty section within a feeder can be detected by comparing the current magnitude from two ends of the section. This can be accomplished by utilizing the current differential relay. This requires communication link between the two ends of a section. The study shows that this relay can detect faulty section quickly.

The wind farm with FCG wind turbines shows significant different fault behavior as compared to the wind farm with DFIG wind turbines. The behavior of each FCG during terminal fault can be represented as constant current source contributing 10% above rated current.

The faulty feeder in the wind farm with FCG wind turbines can be detected by combining the information such as the active power direction and the peak current observed at the collection point. Directional power relay and over-current relay can be utilized to accomplish this objective. The proposed method has taken about 22 milliseconds for detection of the fault.

Three different methods for identifying the faulty section within a feeder were investigated. These methods are:

- Method 1: compares the current magnitude between two ends of the section
- Method 2: compares the direction of the active power between two ends of the section
- Method 3: compares the direction of the positive sequence line to ground (L-G) impedance between two ends of the section

All of these three methods require communication link between two ends of the section. These can be accomplished by utilizing the current differential, directional power, and positive sequence L-G impedance relays.

The Method 1 has taken 4 milliseconds to detect the fault. Method 2 and Method 3 have taken 22 milliseconds, and 18 milliseconds respectively to detect the same fault. It can be seen that Method 1 is faster and having good selectivity to detect the faulty section.

The above conclusions are drawn from a specific study presented in this report and widely different data and network topology may lead to different results.

6.2 Future works

The studies in this report have been carried out using simplified models of DFIG, FCG, and HVDC. The data used in these studies have been taken from the public domain. It is therefore suggested that more realistic models may be developed and the studies may further repeated using detailed models and realistic data.

The protection and control of wind farm collection grid should be studied together with protection and control of HVDC link. The combined study might reveal certain aspect of protection and control which the protection and control study of wind farm collection grid alone may not reveal.

Active protection methods such as injection method may also be investigated, especially protection of wind farm with FCG wind turbines.

The study in this report have considered three-phase direct short-circuit only. The further studies should be made to consider the unbalance and high impedance short-circuit fault.

Different wind farm collection grid topologies may also be studied, since different topologies may require different type of protection scheme.

Further studies on communication link type in the faulty section detection system are needed, since it may interfere the detection time of the relay.

Results may be validated and refined by performing real-time simulation on real-time simulator such as RTDS or OpalRT.

Appendix 1- DFIG model parameters

Part	Label	Description	Value	Unit
Wind Turbine	Pturbine	Rated wind turbine power	3	MW
	Vwrated	Rated wind speed	15	m/s
	Vwcutin	Cut-in wind speed	3.5	m/s
	Vwcutout	Cut-out wind speed	25	m/s
	Rrotor	Rotor radius	45	m
DFIG	Sgen	Rated generator power	3	MVA
	freqgen	Generator frequency	50	Hz
	Vgen	Generator rated voltage	0.69	kV
	J	Generator inertia	0.85	s
	nturn	Stator-rotor turns ratio	0.3	
	Rs	Stator winding resistance	0.0054	pu
	Ls	Stator leakage inductance	0.10	pu
	Rr	Rotor resistance	0.00607	pu
	Lr	Rotor leakage inductance	0.11	pu
	Lm	Magnetizing inductance	4.5	pu
Transformer	Sxformer	Rated power of xformer	3	MVA
	LVxformer	Low voltage of xformer	0.69	kV
	HVxformer	High voltage of xformer	35	kV
	freqgrid	Grid frequency	50	Hz
	Lleak	Positive sequence leakage reactance	0.15	pu
	Culoss	Copper losses	0.015	pu
	Nlloss	No load losses	0.015	pu
PE Switch	Ron	ON Resistance	0.001	Ω
	Roff	OFF Resistance	1	MΩ

Appendix 2- FCG model parameters

Part	Label	Description	Value	Unit
Wind Turbine	Vw	Rated wind speed	13	m/s
	Pturbine	Rated turbine power	3	MW
	Rrotor	Rotor radius	46.2	m
	Arotor	Rotor swap area	6705	m^2
	Rho	Air density	1.225	kg/m^3
	kp	Gain cst of turbine regulator control	6.5	
	ki	Integral cst of turbine regulator control	6.5	
	ks	Gain cst of speed damping	0.05	
	Gm	Gain multiplier	30	
PMSG	npp	Number of generator pole pairs	150	
	Sgen	Rated generator power	3	MVA
	freqgen	Generator frequency	50	Hz
	wref	Generator electrical speed	314.16	rad/s
	nsgen	Generator mechanical speed	20	rpm
	Vgen	Generator rated voltage	0.69	kV
	J	Generator inertia	2	pu
	B	Generator damping	0.002	pu
	VgenPh	Generator line to neutral voltage	0.39	kV
	VgenPeak	Generator peak voltage	0.56	kV
	I_base	Base current	2.51	kA
	I_peak	Current peak	3.55	kA
	Rs	Stator winding resistance	0.017	pu
	Xs	Stator leakage reactance	0.064	pu
	Psi	Generator flux linkage	1	pu
Rectifier	kpc_r	Gain cst of inner controller	1.4	
	Tic_r	Time cst of inner ctrl	0.059	
	kps_r	Gain cst of outer controller	60	

	Tis_r	Time cst of outer ctrl	0.001	
	Lgen	Estimated generator inductance	0.15	
	Idmax	Max current limit	1.1	pu
	Idmin	Min current limit	-1.1	pu
	Vdmax	Max voltage limit	1.05	pu
	Vdmin	Min voltage limit	-1.05	pu
	Vqmax	Max voltage limit	1.05	pu
	Vqmin	Min voltage limit	-1.05	pu
DC-Link	DCv	Rated DC voltage	1.1	kV
	Rbrake	Braking resistance	0.1	Ω
	linkcap	DC-link capacitor	50	mF
	Dcvmax	max DC-link voltage	1.177	kV
Inverter	kps_i	Gain cst of current controller	10	
	Tis_i	Time cst of current controller	0.01	
	Hyband	Hysterisis band	0.05	
Transformer	Sxformer	Rated power of xformer	3	MVA
	LVxformer	Low voltage of xformer	0.69	kV
	HVxformer	High voltage of xformer	35	kV
	freqgrid	Grid frequency	50	Hz
	Lleak	Positive sequence leakage reactance	0.15	pu
	Culoss	Copper losses	0.015	pu
	Nlloss	No load losses	0.015	pu
PE Switch	Ron	ON Resistance	0.001	Ω
	Roff	OFF Resistance	1	MΩ

References

[0] Co-Generation and Renewables: Solutions for a Low-Carbon Energy Future. Technical report, International Energy Agency, 2011. available at http://goo.gl/EHk8B.

[0] Clean Energy Progress Report. Technical report, International Energy Agency, 2011. available at http://goo.gl/oUWHT.

[0] Wind in Power: 2010 European Statistics. Technical report, The European Wind Energy Association, 2011. available at http://goo.gl/214rh.

[0] Benefits of Wind Energy. Website, 2009. available at http://goo.gl/NT6a7.

[0] Global Wind Report 2010. Technical report, Global Wind Energy Council, 2011. available at http://goo.gl/Jzlec.

[0] B. Van Eeckhout, and D. Van Hertem, and M. Reza, and K. Srivastava, and R. Belmans. Economic comparison of VSC HVDC and HVAC as transmission system for a 300 MW offshore wind farm. *European Transactions on Electrical Power*, 20:661-671, 2010.

[0] Meah, K. and Ula, S. Comparative evaluation of HVDC and HVAC transmission systems. *Power Engineering Society General Meeting, 2007. IEEE*, pages 1--5, 2007. IEEE.

[0] ABB differences with classic - HVDC light. Website. available at http://goo.gl/pbhTL.

[0] E.H. Camm, M.R. Behnke, O. Bolado, M. Bollen, M. Bradt, C. Brooks, W. Dilling, M. Edds, W.J. Hejdak, D. Houseman, S. Klein, F. Li, J. Li, P. Maibach, T. Nicolai, J. Patino, S.V. Pasupulati, N. Samaan, S. Saylors, T. Siebert, T. Smith, M. Starke, and R. Walling, "Characteristics of wind turbine generators for wind power plants," *Power Energy Society General Meeting, 2009. PES '09. IEEE*, 2009, pp. 1 -5.

[0] Y.-zhang Sun, J. Lin, G.-jie Li, and X. Li, "A review on the integration of wind farms with variable speed wind turbine systems into power systems," *Sustainable Power Generation and Supply, 2009. SUPERGEN '09. International Conference on*, 2009, pp. 1 -6.

[0] Li, H. and Chen, Z. Overview of different wind generator systems and their comparisons. *Renewable Power Generation, IET* 2, no. 2 (June 2008): 123 -138.

[0] Johns, A.T. and Salman, S.K. *Digital protection for power systems*. Peter Peregrinus Ltd, 1997.

[0] Yalla, M.V.V.S. A digital multifunction protective relay. *Power Delivery, IEEE Transactions on*, 7(1):193 -201, 1992.

[0] Öhrström, M. *Fast fault detection for power distribution systems*. PhD thesis, Department of Electrical Engineering, Royal Institute of Technology, 2003. Available at http://goo.gl/vinpu.

[0] Wang, F. *Power Quality Disturbances and Protective Relays*. PhD thesis, Division of Electric Power Engineering, Department of Energy and Environment, Chalmers University of Technology, 2001. Available at http://goo.gl/16Oo4.

[0] XLPE Cable Systems: User's Guide. Website. available at http://goo.gl/ygxSF.

[0] Du, C. *VSC-HVDC for industrial power systems.* PhD thesis, Division of Electric Power Engineering, Department of Energy and Environment, Chalmers University of Technology, 2007. Available at http://goo.gl/pzfn0.

[0] Pena, R. and Clare, J.C. and Asher, G.M. Doubly fed induction generator using back-to-back PWM converters and its application to variable-speed wind-energy generation. *Electric Power Applications, IEE Proceedings -* 143, no. 3 (May 1996): 231 -241.

[0] Mohan, N. and Undeland, T.M. and Robbins, W.P. *Power electronics*. Wiley New York, 1995.

[0] Shire, T.W. *VSC-HVDC based Network Reinforcement*. MSc thesis, Department of High-voltage Components and Power Systems, Faculty of Electrical Engineering, Mathematics and Computer Science, Delft University of Technology, 2009. Available at http://goo.gl/disyk.

[0] Perdana, A. *Dynamic models of wind turbines: a contribution towards the establishment of standardized models of wind turbines for power system stability studies*. PhD thesis, Division of Electric Power Engineering, Department of Energy and Environment, Chalmers University of Technology, 2008. Available at http://goo.gl/n8Hd5.

[0] Jin Yang and Yajing Gao and O'Reilly, J. Permanent magnet synchronous generator converter protection analysis during DC wind farm open-circuit fault condition. *Electrical Power Energy Conference (EPEC), 2009 IEEE*, pages 1 -6, 2009.

[0] Ramtharan, G. and Arulampalam, A. and Ekanayake, J.B. and Hughes, F.M. and Jenkins, N. Fault ride through of fully rated converter wind turbines with AC and DC transmission. *Renewable Power Generation, IET*, 3(4):426 -438, 2009.

[0] Daryoush Mehrzad, and Javier Luque, and Marc Capella Cuenca. *Vector Control of PMSG for Grid-Connected Wind Turbine Applications*. Master's thesis, Institute of Energy Technology, Aalborg University, 2009. Available at http://goo.gl/VThjZ.

[0] Harnefors, Lennart. *Control of variable-speed drives*. Applied Signal Processing and Control, Department of Electronics, Mälardalen University, Västerås, 2002.

[0] Liu, B. et al. Faults mitigation control design for grid integration of offshore wind farms and oil and gas installations using VSC HVDC.

Power Electronics Electrical Drives Automation and Motion (SPEEDAM), 2010 International Symposium on, 2010, 792 -797.

[0] Jiang-Hafner, Y. and Hyttinen, M. and Paajarvi, B. On the short circuit current contribution of HVDC Light. *Transmission and Distribution Conference and Exhibition 2002: Asia Pacific. IEEE/PES*, pages 1926 - 1932 vol.3, 2002.

[0] Woodford, D. Introduction to PSCAD/EMTDC V3. 2000.

[0] Wilson, P. and Craig, M. PSCAD User's Guide. *HVDC Research Centre, Canada*, 2003.

[0] Cardenas, J. and Muthukrishnan, V. and McGinn, D. and Hunt, R. Wind farm protection using an IEC 61850 process bus architecture. *Developments in Power System Protection (DPSP 2010). Managing the Change, 10th IET International Conference on*, pages 1--5, 2010. IET.

[0] Tleis, N.D. *Power systems modelling and fault analysis: theory and practice*. Newnes, 2007.

[0] Slootweg, H. and De Vries, E. Inside wind turbines-Fixed vs. variable speed. *Renewable Energy World*, 6(1):30--41, 2003.

[0] Muyeen, SM and Takahashi, R. and Murata, T. and Tamura, J. A method to calculate initial conditions of wind generator in transient stability simulation. *3rd International Conference on Electrical & Computer Engineering*, pages 175-178, 2004.

[0] Andreea, C. *Encoderless Vector Control of PMSG for Wind Turbine Applications*. Lambert Academic Publishing, 2011.

[0] Karaliolios, P. and Ishchenko, A. and Coster, E. and Myrzik, J. and Kling, W. Overview of short-circuit contribution of various Distributed Generators on the distribution network, *Universities Power Engineering Conference, 2008. UPEC 2008. 43rd International* , vol., no., pp.1-6, 1-4 Sept. 2008

ELFORSK

SVENSKA ELFÖRETAGENS FORSKNINGS- OCH UTVECKLINGS - ELFORSK - AB

Elforsk AB, 101 53 Stockholm. Besöksadress: Olof Palmes Gata 31
Telefon: 08-677 25 30, Telefax: 08-677 25 35
www.elforsk.se